A Photographic Survey of Very Low Mass Stars and Brown Dwarfs.

Andrew David Thackrah

Presented for the Degree of Doctor of Philosophy
at the University of Edinburgh
1996

This thesis is solely my own composition, except where specifically indicated in the text.

Andrew Thackrah,
November 1996.

Acknowledgments

Firstly I thank my supervisors Mike Hawkins and John Cooke for keeping a watchful eye over me these past four years and especially for some choice but unpublishable comments about various astronomers and for reading the draft of this thesis. On the astronomy side I also want to thank Hugh Jones, Ewan Brown, Harvey MacGillivray, Despina Hatzidimitriou and Barry Croke and also Chris and Richard at the visitor centre as-was.

Love and thanks to Mum, Dad, Alison, Steve and Rachel for putting-up with me and medals to Steve Mc, Harry and Jonny for being excellent wing-men.

Mentioned in dispatches are Ann, Carl, The Mitchell Clan and JB
ADT 1996

"It is to be inferred that there exist countless dark bodies close to the sun - such as we shall never see"
- F. Nietzsche, 1885

Contents

Abstract

This thesis presents a study of the very low mass stars and hypothesised brown dwarf population that straddle the end of the stellar main sequence. The current status of the physical and observational arguments for the existence of sub-stellar objects is reviewed and the most recent numerical models are assessed. The suitability of wide-field photographic plates as detectors of this type of object is investigated, a 112 square degree photographic survey is described and subsequent candidate observations are presented.

It is found that for conventional survey-grade U.K. Schmidt plates, the detection probability is sensitive to a range of assumptions concerning the initial mass function and density distribution function. For objects of spectral class later than M5, brown dwarfs may constitute up to one third of the objects detected, though this value is extremely sensitive to the photographic flux limit and is also found to decrease toward the plate limit if a time-dependent density function is used to describe the space distribution. The height of the Sun above the Galactic plane is considered and it is calculated that the given present estimates, an upper limit to the likely variation in number density is around 50%, corresponding to less than ten objects per square degree. Variations of the assumed initial mass function strongly affects the absolute values.

The predicted age distribution of detectable brown dwarfs suggest that the vast majority of them will be less than 1 gigayear in age. The predicted spectral distribution begins around M4 to 5 , peaking around M6 to M7. A photographic brown dwarf survey is feasible provided suitable follow-up measurements are carried-out to assess the ages of candidate objects. In mid-to-high latitude Galactic fields photographic plates are more suited to such a survey than current CCD detectors.

A photographic survey is described making use of R and I band photographic plates from the U.K. and ESO Schmidt telescopes. The ROE's COSMOS and SUPERCOSMOS densitometers were used to measure the plates with candidates being selected

by photometric colour. The techniques devised to match the image catalogues, photometrically calibrate the magnitude scale, automatically classify stellar and galaxian images and measure image displacements are described. The luminosity function derived from the survey is found to conform to previous determinations, showing no sign of increasing space density in the faintest bins.

A follow-up observational programme based on a sub-set of candidates selected from the survey was conducted. Spectroscopic measurements in the $6500 - 9000$Å range are presented with the emphasis on the detection of the 6708Å Li I resonance doublet. Lithium is detected in at least one of the survey objects. The object appears to be a young brown dwarf with a mass in the range $M/M_{\odot} = 0.065 \pm 0.025$. This object is important in being the first Galactic field brown dwarf candidate to pass the so-called 'Lithium test'.

Chapter 1

Introduction

Stars with masses below $0.3M_{\odot}$, usually called late M dwarfs, red dwarfs or very low mass stars (VLMSs) account for 40% of the Galactic disc's stellar population by number and 25% of its mass (Miller and Scalo, 1979). These values are lower limits because the extent of the population is still uncertain. Surveys of these stars are hampered by their extreme intrinsic faintness and unlike brighter, higher-mass stars, our knowledge of the nature of this population has only been able to advance in-line with improvements in instrumentation.

With every advance fainter, cooler, lower-mass stars have been discovered, extending the population towards the theoretically predicted physical end of the stellar main sequence - the hydrogen-burning minimum mass (HBMM). Beyond this limit lies the hypothesized *brown dwarf* population, a class of objects spanning the mass range between stars and jovian planets. After more than two decades of intensive surveying the Galaxy's brown dwarf population is begining to reveal itself in a variety of astronomical environments. The optimism inspired recently by the first few positive detections has given a new impetus to the consideration of this class of star as a population and its possible influence on the current outstanding research topics of star formation and the Galactic mass/luminosity relation. Although faint, nearby stars were discussed in the early decades of this century as an explanantion for Oort's dark matter (Oort, 1932) work did not begin in earnest until a suit-

able physical model had been established. The hurdle of designing a theoretical model of the formation of a star with a (fully) convective core was scaled almost fifty years ago by Hayashi (1962). The model was soon applied to the problem of low mass stars (Kumar, 1963) and resulted in the prediction of a cessation of stable hydrogen fusion in stars with masses around $0.1M_{\odot}$. The model allows for lower mass stars whose cores become sufficiently degenerate during contraction to prevent the further temperature rise necessary to initiate stable hydrogen-helium fusion reactions.

Such stars were named 'black dwarfs' and have since come to be referred to as 'brown dwarfs' (Tarter, 1985). The minimum mass at which stable hydrogen burning is possible represents the physical end of the main sequence and the start of the brown dwarf population. Brown dwarf models have been computed for masses as low as $0.01M_{\odot}$, just ten times the mass of Jupiter (giving rise to the name 'super Jupiter') and attempts to determine a physical lower limit to this, still theoretical population are hampered by our lack of understanding of the nature of cloud-fragmentation in the star-formation process.

With an established physical model, observational surveys began. To date there have been more than 40 surveys (see Burrows & Liebert, 1993) making use of almost every astronomical tool. The surveys can be broadly grouped into those that have searched for companions to brighter stars, those that have surveyed young Galactic clusters and those that have searched the *field stars* of the local Galactic disc. Searches for faint stellar companions have employed astrometry and high-resolution spectroscopy to detect the gravitational effect of potential partners. The most recent survey by Marcy and Butler (1995) have refined the technique of measuring radial velocity perturbations to the point where they are able to detect objects of Saturnian mass and have done so (Marcy & Butler, 1996a,b).

The coolest stars (< 3000K) are best studied in the infra-red where they are brightest. Henry and McCarthy (1993) have employed a method of infra-red speckle spectroscopy to conduct an astrometric search of nearby red dwarfs. The most

valuable feature of surveys of this type is that a direct dynamical measure of the system's mass can be made. As mass is regarded as the only reliable way of determining the nature of a star and can say more in the absence of other information than any other stellar property, a great deal of effort has been expended on this type of survey. The disadvantage of the methods generally is that they are restricted to the study of relatively bright and therefore very near-by stars ($\approx 12^{th}$ mag. and $\approx 10pc$ respectively).

The detection of fainter, more distant stars requires long exposures over wide areas since the aim is to sample the largest possible volume. CCD detectors and photographic plates are employed in such surveys and the nature of the work is such that high-accuracy astrometry is neither possible nor required. The goal is to detect previously unknown stars from the mass of data by identifying those images with distinctive motions or colours.

Many of the faintest known stars were discovered in the LHS survey (Luyten, 1979) which represents the culmination of decades of work. The survey initially measured proper motions by comparison of Palomar Schmidt plates with a mechanical blink comparator. Each star was also assigned a crude photographic colour corresponding roughly to the modern B-R (actually o-e) colour. Distance was deduced from a property that Luyten called the *reduced proper motion* that related brightness to proper motion by assuming a common tangential Galactic speed for all local disc stars. Improvements in the survey led to the development of the first automated plate measuring machines. The COSMOS machine in Edinburgh followed in 1980. Being able to measure a 900 cm^2 photographic plate in six hours, giving the positions of several hundred thousand images with sub-micron accuracy and photometric measurements accurate to less than ten percent, the machine and its partner APM in Cambridge have been used for many Galactic surveys of both field stars and clusters.

Of the Galactic clusters the Pleiades, Hyades and Praeseppe are the most studied. Being young and nearby they offer the best chance to detect the faintest stars

whilst they are in the brightest stage of their evolution. If membership of the cluster can be determined with confidence (e.g. by coherent proper motions) then within the survey's limits the number density of the sample in terms of luminosity and, most importantly, mass can be measured. This distribution will be close to the initial (zero age main sequence) *mass function* (IMF) which is believed to be determined by the physical processes of star formation. It can be used to study the Galaxy's mass/luminosity relationship as a probe of the *dark matter* which may account for the controversial discrepancy between the Galaxy's visible and dynamic mass distributions (see Kuijken & Gilmore 1989c).

An important result of recent surveys of young clusters is the similarity in the shape of their IMFs, supporting the theory of a 'universal' star formation process. At low masses the number counts appear to increase with decreasing mass right down to the HBMM, at which point the photographic surveys tend to become statistically incomplete. This incompleteness is an unfortunate product of a photographic plate's high flux limit and the relatively large distance moduli of these clusters. To overcome this limit requires a deeper CCD survey, two of which have recently identified brown dwarfs in the Pleiades (Rebolo *et al.* 1995, Basri *et al.* 1995). The survey conditions support an increasing mass function beyond the HBMM although the numbers involved and the small areal coverage of these surveys weakens the significance of the statistics.

To detect the very lowest mass stars, photographic surveys may be put to better use by surveying the local disc stars of the *solar neighbourhood* which can be loosely defined as the volume around the sun in which accurate parallax measurements can be made. In this region surveys with wide-field photographic plates remain competitive with the much more efficient CCDs due to their far superior areal coverage. In some respects (discussed later) they may be more suited to the job of detecting young, low-mass disc stars. The photographic V–I survey of Reid & Gilmore (1982) established the space density of local M dwarf stars and presented evidence of a rare 'thick disc' population. The survey technique was extended toward the infra-red with R–I surveys (Hawkins and Bessell, 1988, Leggett &

Hawkins, 1988) which probed the faintest main sequence stars and stretched the luminosity function (LF) towards the HBMM. A larger 270 square degree survey was carried out by Tinney (1993) again using photographic R–I selection. Between them, these three surveys have consolidated the local M dwarf luminosity function. The surveys are in general agreement over the shape and size of the LF for all but the faintest bins. Here the number counts fall and statistical uncertainties lead to differences in the measured shape, and most importantly the general trend as the function enters the brown dwarf regime.

For the stars that straddle the end of the main sequence, the conversion of the luminosity function to a mass function is critically sensitive to the stellar mass-luminosity relationship and the empirical measurements of luminosity. The photometric accuracy of a survey therefore determines the accuracy to which the survey can be used to explore the mass density distribution of a population. A CCD survey can achieve a higher level of photometric accuracy, and should in principle replace photographic plates as the favoured survey detector. CCD surveys have yet to make such an impact in this field. The 27 square degree survey of Kirkpatrick *et al.* (1994) plays-off depth for area and the deep 'pencil beam' survey of Hu *et al.* (1994) sacrificing statistical value through areal coverage and choice of photometric system.

A new generation of infrared technology may raise the profile of CCD cameras in the field of cool star detection. Two surveys in particular; the Two Micron All Sky Survey (2MASS, Chester 1995) and DENIS (a less convincing acronym, Copet *et al.* 1995) will survey all (2MASS) and over half (DENIS) of the sky in the infra-red photometric bands. 2MASS will conduct its survey in the JHK bands to a depth of 15 and DENIS in the IJK bands with 0.5 - 1.0 magnitude lower sensitivity. The value of these surveys to brown dwarf science depends very much on the local space density of these stars and on the ability of these surveys to actually select candidates from the mass of data produced. Predictions of the expected number of brown dwarf detections range from 0 to over 1000! Selection is not necessarily straight-forward since the infra-red bands cover a relatively short

baseline (in wavelength) from which to produce colour diagrams. The popularity of the visible system lies with the importance of the broad-baseline visible-IR colours, especially I–K. For this reason, DENIS may have the advantage in the short term although the data from both surveys will eventually be matched to photographic plates.

The discussion above emphasises the value of the photographic plate as a modern wide-field survey tool, which I take as the main theme of this thesis. In the subsequent chapters, I discuss the latest developments in modelling stellar structure and empirical relationships based on recent surveys. Predictions of the observable distribution of very low mass stars and the variations likely for various survey criteria are discussed in chapter three. The subsequent two chapters describe a low mass star survey carried with photographic plates of the UK Schmidt telescope and measured with Edinburgh's COSMOS and SUPERCOSMOS machines. Observations from a follow-up programme to that survey are included along with a discussion of uncertainties and implications raised in earlier chapters.

Chapter 2

Low mass stars - Theory and Observation

Our first requirement is to assess the physical case for the existence of brown dwarfs. The areas of physical theory that concern us are those of star formation, particularly cloud fragmentation and the concept of an *Initial mass function* (IMF) and that of stellar structure and evolution. Whereas the models of cloud fragmentation are still in their infancy the study of the resulting IMF is better developed as a consequence of surveys of young stellar associations. The models of brown dwarf and low mass star structure appear considerably more mature but, as we shall find also lack important observational constraints.

2.1 Star formation and the initial mass function.

In the murky world of brown dwarf semantics a consensus has arisen that these objects form by the fragmentation of molecular clouds like stars and not by accretion in a proto-stellar disc, like planets. In our haste to discover these elusive objects, the detection of GL 229B. (Nakajima *et al.* 1995) may overturn this definition, but for the moment I will use it as it applies to the nature of the survey described in this thesis. Our question is *'is there a physical lower limit to the size*

of star-forming fragments in molecular clouds?' It seems that as yet, there is no answer to this question and few people have attempted to answer it in the context of brown dwarf studies.

Boss (1986) suggests a lower fragmentation limit around $0.02M_{\odot}$ and the Pleiad Teide 1 appears close to this value. Boss' calculations however are based on models of equal-mass binary fragmentation which only extend to $0.02M_{\odot}$ so the possibility of lower-mass fragments should not be ruled-out. Boss notes that the inclusion of any more complicated physics, such as turbulence can only act to introduce kinetic energy into the system and *increase* the minimum mass.

In a more recent paper (BM92: Boss and Myhill,1992) the possibility of fragmentation in tri-axially symmetric (i.e. ellipsoid) clouds is investigated over a wider range of physical conditions. The ratios of rotational and thermal to gravitational energy in the initial (isothermal) clump are free parameters. There are three paths for the initial clump; expansion, collapse to a single object or fragmentation. BM92's calculations suggest that the multiple fragmentation events occupy a much larger region of 'parameter space' than the single objects or expansion: as might be expected from the observation that most stars are in binary systems (Abt 1979). The models are explicitly designed to study fragmentation scenarios and do not provide further constraints on the minimum fragment mass. In these simulations fragmentation is only seen to occur in the first stage of dynamic 'free-fall' collapse. The second stage of collapse, induced by the dissociation of molecular hydrogen does not induce fragmentation in these models and BM92 suggest that the initial stage of collapse may be critical to the formation of binary (i.e. most) stars. The implication of this for brown dwarf formation may be that they must either form from large initial fragments, with their mass essentially determined by the large-scale conditions of the pre-collapse cloud (rather than the conditions of sub-clumps) or that they may form later in proto-stellar accretion discs - raising the suggestion of a planetary 'super-Jupiter' origin.

The conditions for fragmentation in proto-stellar discs has been studied by Adams

and Benz (1992), starting with a perturbed disc model and following the growth of instability in low-order modes of the system. Again the model is not explicitly concerned with brown dwarf formation but they present a scenario in which low mass stars ($\sim 0.05 M_{\odot}$) could form with planet-sized companions due to the growth of instabilities into the system at a very early stage. Much of the material ($\sim 1 M_{\odot}$) has yet to accrete, raising the possibility that the smaller member will grow to brown dwarf size. Adams applies the model to brown dwarfs in a later paper (Adams 1995) taking the approach that the end result of the star formation process is an observable distribution of stellar mass fragments. He also points out that there is no 'mass scale' during fragmentation and that any mass spectrum is likely to be modified by 'stellar processes'.

The mathematical relation that describes the spatial distribution of stellar mass is known as the mass function. This normally applies solely to main sequence stars with an Initial Mass Function (IMF) describing the space density distribution of 'zero-age' main sequence stars. The initial conditions of star formation, the sound speed, rotation rate, magnetic field strength and so on must influence, if not determine the IMF and it is possible that although the function varies from place to place the overall form is 'universal'. Adams' conclusions reiterate those of Boss, stating that the evidence is weighted towards a higher fragment limit, making field brown dwarfs unlikely although not affecting the likelihood of brown dwarfs forming as 'planets' i.e. in an existing proto-stellar nebula. Both authors recognise the lack of hard observational evidence, particularly of proto-stellar binary systems. This is due at present to technical limitations and since their conclusions are based on a semi-empirical study using simplistic initial conditions it seems clear that the subject will only be clarified by further observational work and that the negative tone of the predictions should not discourage future surveys.

2.2 Stellar structure models.

If we have convinced ourselves that brown dwarfs can form at all then we must next consider their physical nature. We require predictions of observable properties that can be detected in a survey. Stellar structure models predict the luminosity and effective (black– body) temperature which can be related to the observable brightness and spectral energy distribution of a star. The models of Hayashi (1962) paved the way for the first brown dwarf models of Kumar (1963). The models describe a fully convective isothermal sphere; a polytrope whose gravitational contraction provides an initial source of luminosity. The state of the material in the star is mostly dependent on the mass of the star and if this is sufficiently low, the combination of pressure and density produced ensure that the core becomes electron-degenerate before the temperature has risen high enough to ignite a hydrogen fusion chain reaction. This is the most basic definition of a brown dwarf star and tells us that the defining criterion is the mass of the forming star. The models that describe brown dwarfs are applicable to low mass stars too, i.e. there are no new physical assumptions introduced which, in light of the success of low mass stellar structure theory, suggests that brown dwarfs are physically possible. Spurred-on by this, we now look at the most recent versions of this model, examining the predicted evolution of the objects in some detail to identify those properties which may act as an observational signature.

The models discussed here are those of D'Antona and Mazzitelli (DM85, 1985), Nelson, Rappaport and Joss (NRJ86, 1986) and Burrows *et al.* (BHSL93, 1993) which have enjoyed the most interest recently. The models are broadly similar to the work of Grossman *et al.* (1974) and are in close agreement about the most important prediction of the models: the hydrogen burning minimum mass (HBMM), which can be thought of as the physical lower-limit of the stellar main sequence and the start of the brown dwarf sequence. The value for the HBMM is close to $0.08M_{\odot}$ and predictions vary less than $\pm 0.015M_{\odot}$ for a wide range of metallicities.

The models available describe masses from $0.3M_{\odot}$ to $0.01M_{\odot}$: the range of fully

convective stars. To give a quantitative description of the nature of current models, the evolution of a low mass star ($0.11M_{\odot}$) an intermediate mass object sometimes called a *transition object* ($0.08M_{\odot}$) and a low mass brown dwarf ($0.05M_{\odot}$) are compared. The intention is to emphasize the early similarities and later differences with a view to identifying useful observational discriminants for a mixed-age sample.

For the first 10^6 years of their lives, our stars follow a similar path of gravitational heating, reaching $T_{\rm eff} \simeq 4000K$. The stars are likely to be embedded in an optically thick molecular cloud and reveal their presence in coincidence with the initiation of deuterium fusion. This period of steadily-falling luminosity, part of the *T Tauri phase* lasts until the stars are roughly 10^7 years old. The central temperature in these proto-stars is around 10^6K and this thermal energy source endows the $0.11M_{\odot}$ star with a luminosity of $0.1L_{\odot}$, the $0.08M_{\odot}$ star being roughly $0.05L_{\odot}$ and $0.05M_{\odot}$ star already falling below $0.01L_{\odot}$. This stage sees a *fall* in the luminosity of the stars by an order of magnitude in each case accompanied by a negligibly small drop in surface temperature. The central temperature meanwhile has risen above the $2.5x10^6$K required for lithium fusion in the two higher-mass stars. In objects lower than $0.06M_{\odot}$, this temperature is never achieved, because during this stage of the stars evolution, electron degeneracy pressure is starting to become important to the stability of these stars, due to the inefficiency of nuclear reactions under these conditions. Although important for observational reasons which are discussed later, the energy contribution of lithium fusion is paltry and with the cessation of deuterium fusion, the stars begin their next phase of contraction and thermal heating between 10^7 and 10^8 years.

With no nuclear energy source to support the stars, they begin to contract and the structure increasingly relies on electron degeneracy pressure for support. The heat supplied to the centre is proportional to the star's mass but as the core becomes increasingly dense and degenerate, the rate of temperature-rise falls. If the temperature reaches a value sufficient to ignite the ppI hydrogen-fusion chain reaction ($\sim 5 \times 10^6 K$) then the thermal pressure becomes dominant and the star moves

towards a state of hydrostatic equilibrium known as the stellar main sequence. Should the heat supplied be too low to achieve this temperature before the onset of full electron degeneracy then the object is supported by a pressure source that has almost no dependence on temperature and the centre will not become any hotter. Thus, the ppI chain reaction never begins (although some short lived period of hydrogen burning may happen) and the object 'fails' to become a main sequence star.

Our $0.11M_{\odot}$ object will reach the main sequence, our $0.05M_{\odot}$ object will not. The $0.08M_{\odot}$ object reaches this stage with physical conditions that lie critically between the two extremes with the result that it may continue to burn hydrogen at a very slow rate for several times 10^{10} years, never quite reaching the main sequence, but never cooling fully into the brown dwarf regime. The star is essentially 'frozen' into a T Tauri stage and lying as it does at the physical *transition* between main sequence stars and brown dwarfs is given this name. At this stage (around 5×10^8 years the stars become observationally distinct as the higher mass star settles at a constant luminosity of $10^{-3}L_{\odot}$ and the lower mass brown dwarf begins to fade, reaching $10^{-5}L_{\odot}$ after 10^9 years and less than $10^{-6}L_{\odot}$ after 10^{10} years. During this time, the $0.11M_{\odot}$ star reaches a surface $T_{\rm eff}$ ~2800K, the $0.08M_{\odot}$ dwarf cools gradually falling to around 2000K and the $0.05M_{\odot}$ dwarf cooling to below 500K. The main sequence star will not evolve appreciably for a time exceeding 10^{10} years; comparable to the age of Universe. During this time, the brown dwarf will continue to cool and fade and will increasingly take on the appearance and characteristics of a giant gas planet such as Jupiter.

Figure 2.1 summarises the evolution of low mass stars according to the three quoted models. The figure compares the derived mass-luminosity relationships (M/L) at several epochs corresponding roughly to T tauri stage (3 Myr), young cluster (70 Myr; Pleiades age), old cluster (600 Myr; Hyades age) and young, intermediate and old Galactic disc populations (1, 5 and 10 Gyr respectively). The M/L relation is the most important product of low mass stellar models, allowing a direct relation of the measurable luminosity to the usually unmeasurable mass which is essential

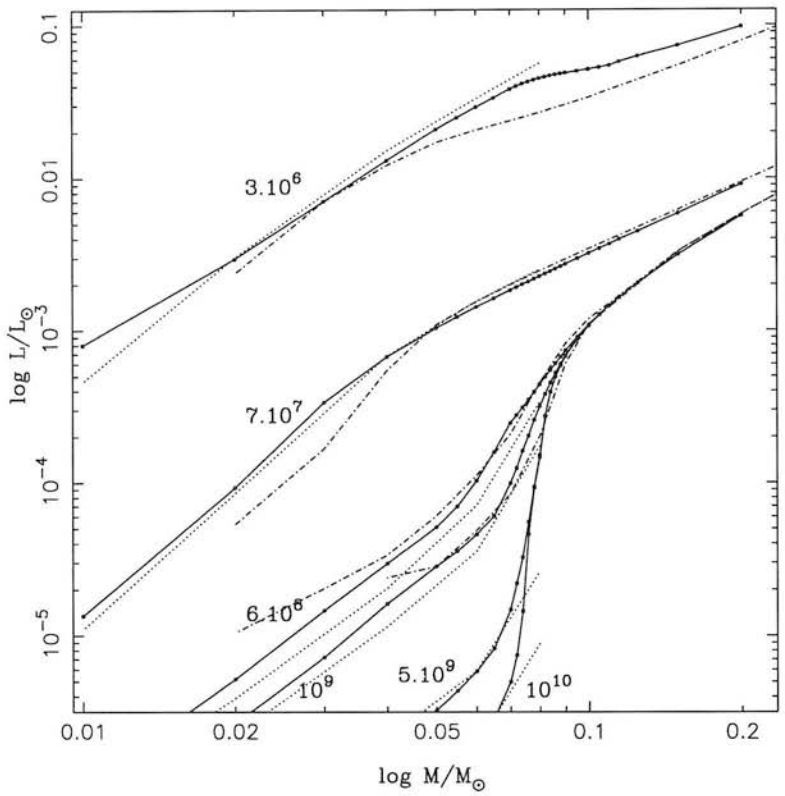

Figure 2.1: Mass-luminosity relation for three low mass star models, compared (where published data are available) at several epochs from 3 Myr to 10 Gyr. Solid lines with grid points (circles) are Burrows *et al.* (1993) model X , dot-dashed lines are D'Antona and Mazzitelli model 7, 1993 and dotted lines for the Nelson *et al.* 1986 model.

for converting the observed *luminosity function*; the number density of stars as a function of luminosity, to the mass function. From the mass function we can estimate the initial mass function and surface mass density to be compared with estimates of missing or dark matter in the Galaxy.

As figure 2.1 shows, the three compared models are in reasonable agreement with the largest discrepancies occurring for the lowest masses and earliest epochs. All the authors warn of the dangers of taking the computations of the earliest epochs too seriously due to the basic lack of knowledge of the physical conditions affecting a proto-star (see section 2.1). The M/L at early epochs can be represented by a

simple power law over the whole mass range considered. The luminosity evolution is clearly rapid and the isochrones for the higher mass 'true' stars soon converge. The most important feature of the diagram is the extremely steep gradient for transition objects and the continued rapid luminosity evolution at later epochs in the lower mass stars. The effect of the steep gradient for transition objects is to make the determination of a transition mass function extremely sensitive to errors in the measurement of luminosity. The rapid cooling of the lower mass stars has the affect of making luminosity function completely age-dependent, which all but rules-out an observational determination of the mass function for these stars unless the age of all contributing objects is known.

2.3 Low mass stellar atmospheres

The account above has described the predictions by stellar structure theory of a star's luminosity and effective temperature. To express these quantities in terms of observable magnitudes and colours requires an understanding of the only part of the star that is visible to an observer: the atmosphere. The atmosphere is an important boundary condition in models of stellar structure. It determines the rate of radiation escape and thus the temperature gradient and convective nature of the star, which in turn affects the internal chemical distribution and thus the conditions of hydrostatic stability.

2.3.1 The black-body distribution

The simplest model we could adopt for VLMSs and BDs is of an ideal gas in thermal equilibrium: a black-body radiator. The radiant flux has a Planck distribution, which peaks, according to the Wien displacement law at 0.9 μm for our $0.11M_{\odot}$, 3150K star, at 1.2 μm for our $0.08M_{\odot}$, 2600K transition object and at 2.1μm for the $0.05M_{\odot}$, 1400K brown dwarf. The bulk of the flux is radiated at wavelengths between 1 and 4μm and we can see from this that BDs are best

studied at near infra-red wavelengths. Table 2.1 summarises the approximate [1] absolute magnitudes expected for our three example stars as black-bodies.

Table 2.1: Predicted photometric magnitudes for cool dwarfs at 10^9 years.

Mass	T_{eff}	M_B	M_V	M_R	M_I	M_J	M_H	M_K	M_{bol}
$0.11M_\odot$	3150K	12.7	11.4	10.2	9.6	8.2	7.6	7.2	11.7
$0.08M_\odot$	2600K	15.9	14.2	12.6	11.8	9.8	9.0	8.4	13.5
$0.05M_\odot$	1400K	25.3	22.3	19.0	17.2	13.3	11.5	10.2	16. 1

2.3.2 Absorption features.

In fact, the flux distribution of cool stars differs vastly from the underlying distribution to the extent that in some cases it is difficult to even estimate their effective temperature. This remains a systematic source of disagreement between observers and modellers of cool stellar atmospheres (see Kirkpatrick 1995 for example). The black body treatment remains important however due to the need to compare atmospheric observations and predictions to the effective temperatures produced by the stellar models.

Cool stellar atmospheres permit the formation of atoms, molecules and below 2400K, condensed grains which act as very strong sources of absorption. The spectral region of interest in cool stars extends from around $0.5\mu m$ to $4\mu m$. The opacity in this spectral region is dominated by 3 sources: VO (Vanadium oxide) in the R and I bands, TiO in the V, R and I bands and H_2O in the J, H and K bands (see Kirkpatrick *et al.* 1991 for example). In the case of a $0.1M_\odot$ star such as Gl406 (spectral class dM6; see table 2.2), the effect of metal oxide absorption is to reduce the flux in the R and I bands to around 15% and 50% of the continuum values respectively. Up to M6, the oxide bands allow for reliable spectral classification,

[1] Using standard Johnson/Cousins/IR systems with box filter profiles and Burrows *et al.* model G (1989).

beyond this the bands are less useful and attention is turning toward the use of the near IR H_2O bands to complete the sequence and extend it into the brown dwarf regime (see Jones *et al.* 1994 for example.) The absorption is very temperature sensitive and leads to an increasingly steep photometric temperature-colour relation. The high pressure-sensitivity of some features allow us to discriminate between dwarfs and giants. Particularly useful are atomic features due to sodium and calcium.

2.3.3 Emission features.

The 3-2 transition of the hydrogen atom, the principal line of the Balmer series is usually referred to as Hα and has a rest frequency of 6562.808Å placing it in the photometric R band. This is the only notable emission line of interest in the 0.5 - 4μm region of cool stars. The presence of the line is related to the youth of the star although the mechanism involved is poorly understood. It appears to be due to chromospheric activity and is likely to be related to the rotational period of the star, which decreases with age. Magnetic activity and membership of a binary system have also been suggested to explain the phenomenon. The correlation of Hα emission with youth is most evident in the dMe spectroscopic sub-class, whose members collectively show a lower velocity dispersion than the dM population as a whole.

Young stellar clusters such as the Pleiades and the Hyades have been subject to detailed studies of Hα emission. Having similar age and metallicity the stars in each cluster shed light on the natural spread of the line strength at a given age. It is clear from these studies that although the strength of the line decreases with age, there is sufficient spread to prevent anything other than a rough age determination for a star in emission. Hawley (1995) has shown that the fraction of M dwarfs showing emission rises to a peak of (~ 0.6) at M5. Beyond this there are insufficient measurements to be statistically useful.

The strength of the line is usually expressed with the *equivalent width* convention.

The width measured is that of a rectangular line profile which contains that same flux above the background continuum as a true line profile, which is considerably more extended. The measurement is therefore dependent on the continuum value that is assumed in the region of the line and in the case of M dwarfs, the continuum is almost completely destroyed by molecular absorption, leading to systematic differences in the measurements of different authors.

2.3.4 Model atmospheres

The treatment of the atmosphere in low mass star models has always been something of a grey area. That is, the 'Eddington' treatment of the gas assuming radiative equilibrium and a monochromatic $T(\tau)$ relationship has been used. As Baraffe *et al.* (1995) point out, such assumptions break down in the $2500 < T < 4000K$ range due to H_2 dissociation. They also note that although the grey assumption is useable below 2500K, the formation of grains will alter the appearance of the stellar spectrum, if not the evolutionary processes of the star.

The failure of grey models is revealed by comparison with observations. The parallax program of Monet *et al.* (1992) has produced the definitive observational HR diagram for low mass stars and is sufficiently accurate to resolve the low-metallicity sub-dwarf population with ease. This and other work (Kirkpatrick *et al.* 1991, Bessell 1991) reveals a consistent offset of around +200K between effective temperatures calculated with model atmospheres using the Eddington approximation and those calculated using observed flux distributions. The higher temperatures of the model atmospheres have been recognised as being due to the overly-simplistic treatment of the principal sources of absorption; H_2O, TiO and VO. Recently, synthetic spectra (Allard 1990) have been generated to overcome this problem. The 'first generation' of models producing some convergence of results for higher temperature dwarfs (Kirkpatrick *et al.* 1993) but remaining too high for lower temperature stars. More recent models (Baraffe *et al.*) claim to be able to reproduce the observed colours of lower metallicity stars. The same authors

note discrepancies between their predictions for the lowest mass stars observed by Monet *et al.* and Kirkpatrick with inaccurate treatment of TiO features seeming to be the likely culprit.

In conclusion, the much discussed 200K gap between theory and observation, though narrowing for hotter stars, remains. The fact that the accuracy of the synthetic spectra results vary with metallicity and that the observational HR diagram work tends to use crude metallicity delineations in colour-magnitude relationships suggest that neither party are fully in error. Agreement will be met when the difficult task of modelling stellar absorption features is achieved and better observational discrimination of metallicity is possible. Until then, the $\pm$200K discrepancy remains as a lower limit to the accuracy with which we can compare theoretical and observed effective temperatures.

Having discussed some details of the theoretical side of the subject we now turn to the observational record to date. We see to what extent the observable properties are related to the predictions and conclude by estimating the likely bounds and possibilities of our chosen survey method in the light of previous surveys. This requires a discussion of the various photometric systems involved in finding appropriate bolometric corrections as well as our knowledge of the IMF, the galactic star-formation history and the local mass density.

2.4 Previous surveys

Due to their low luminosity, the first red dwarfs to be discovered were the nearest ones: the most apparently bright. Their proximity also emphasised their space motion and it was through their relatively high proper motions that they were detected. The most comprehensive and enduringly valuable proper motion survey is the LHS survey (Luyten 1979). Along with the NLTT catalogue (Luyten 1979) it contains over 50,000 stars with proper motions as small as $0''.1\mathrm{yr}^{-1}$ and is estimated to be 90% complete for 65% of the sky (Dawson 1986), although the value is almost certainly an over-estimate for M dwarfs. The survey detected some of coolest known stars such as LHS 2924; spectroscopic type M9V which define, in observational terms, the end of the main sequence. Palomar 'o' and 'e' band plates were used in this survey to assign a rough photographic colour to each star and distances were calculated using a reduced proper motion value; a statistical measure of luminosity based on the assumption of a common tangential velocity for all stars a given Galactic radius. To fully exploit the catalogue better parallax and photometric measurements had to be made and many of the stars found their way into the Gliese catalogue.

The Gliese catalogue (1969) and the updated Gliese and Jahreiß catalogue (1991) collect together all known stars within 25 parsecs of the solar system. As other surveys (e.g. Henry & McCarthy 1992) have demonstrated, the Gliese catalogue is clearly incomplete for the faintest stars but it still contains a wealth of photomet-

ric and distance data. Many, if not all of the Gliese stars have been the subject of a search for fainter companions and the successful discovery of low mass companions around two stars in particular raised hopes amongst brown dwarf hunters (Harrington 1986). These stars, Gl 644C and Gl 752B, also known as VB 8B and VB 10B have since been relegated to the status of dM7 and dM8 stars respectively, but due to their brightness continue to be studied for comparative purposes. Recently, the star Gl 229 has yielded its companion to infra-red study and this star, Gl 229B is sufficiently faint and red mark it as a definite brown dwarf, or even a 'super Jupiter'. Its infra-red spectrum more closely resembles the planet Jupiter than any star, showing methane absorption features which may only exist below 1000K. From stars such as these and other hard-won discoveries such as GD 165B (Becklin & Zuckerman 1988) and Teide 1 (Rebolo *et al.* 1995) a picture of the observational properties of the lowest mass stars has emerged. Eight of the most important stars in this field are listed in table 2.2 with their estimated mass, effective temperature and wide-band photometric magnitudes. The photometric colours are the most important measurements to would-be wide-field surveyors and are discussed in more detail in the following section.

2.5 Photometric properties.

We start with table 2.2; the measured photometric magnitudes and effective temperatures for a judicious selection of very low mass stars and brown dwarf candidates which allows us to gauge the variation between observations and the level of agreement with theory.

Notice how these stars are very much fainter in visible bands than the black-body estimates in table 2.1 would have us believe. The R band contains at most, a few percent of the original continuum, the rest being dispersed in to the infra red. This is the effect of the metal oxide absorption bands described in section 2.3.

Table 2.2: Definitive dwarfs that straddle the end of the main sequence.

Name	sp. type	Mass ($M_\odot$)	$T_{\rm eff}$	M_R	M_I	M_J	M_H	M_K	M_{bol}
Gl 699	M5	0.17	3095^J	12.0	10.5	9.0	8.5	8.2	10.9
Gl 406	M6	0.1	2670^J	14.7	12.5	10.2	9.6	9.2	12.2
VB 8	M7	0.1:	2650^B	15.6	13.2	10.7	10.2	9.8	12 .9
VB 10	M8	0.085	2506^J	16.3	14.0	11.1	10.4	10.0	13. 3
LHS 2924	M9	0.081	2219^J	-	15.1	11.7	11.0	10.5	14.0
Teide 1^R	M8	0.05?	2600	16.1	13.3	-	-	9.6	12.7:
GD165 B	M10+	0.06?	1856^J	20.3:	17.9	13.2	12.1	11.4	14.9
Gl $229B^N$	?	0.02?	1200:	23.3	21.2	14.7	14.4	14.6	17. 3:

Photometry from Leggett (1992), other data from B: Bessell (1994) K: Kirkpatrick (1994) R: Rebolo *et al.* (1995) N: Nakajima *et al.* (1995) J: Jones *et al.* (1994).

The effect varies strongly across the visible photometric bands, decreasing with wavelength and has the affect of enlarging the photometric colour terms of the stars. The most important colour for this survey is R–I which, for a late M dwarf is greater than 2.0, compared to the black-body estimate of 0.6. The sensitivity of other colour indices in this spectral region gives us a valuable tool for determining the temperature/spectral class of the star. The values given in table 2.2 are based on measurements in the Cousins and Infra-red (JHK) photometric systems which are the most frequently quoted systems. In the case of the R and I bands, other systems such as Mould, Gunn and the 'natural' photographic system are also used and it is important to be aware of the *colour terms*, the differences that arise between the various filter/detector combinations.

2.5.1 Colour terms between photometric systems.

Although I band photometric systems are generally very similar, the R band filters have very different filter profiles from system-to-system. This leads the large to differences between measures in the systems and is most evident in the discrepancy between the Cousins photometric and the 'Schmidt' photographic R–I colours (see

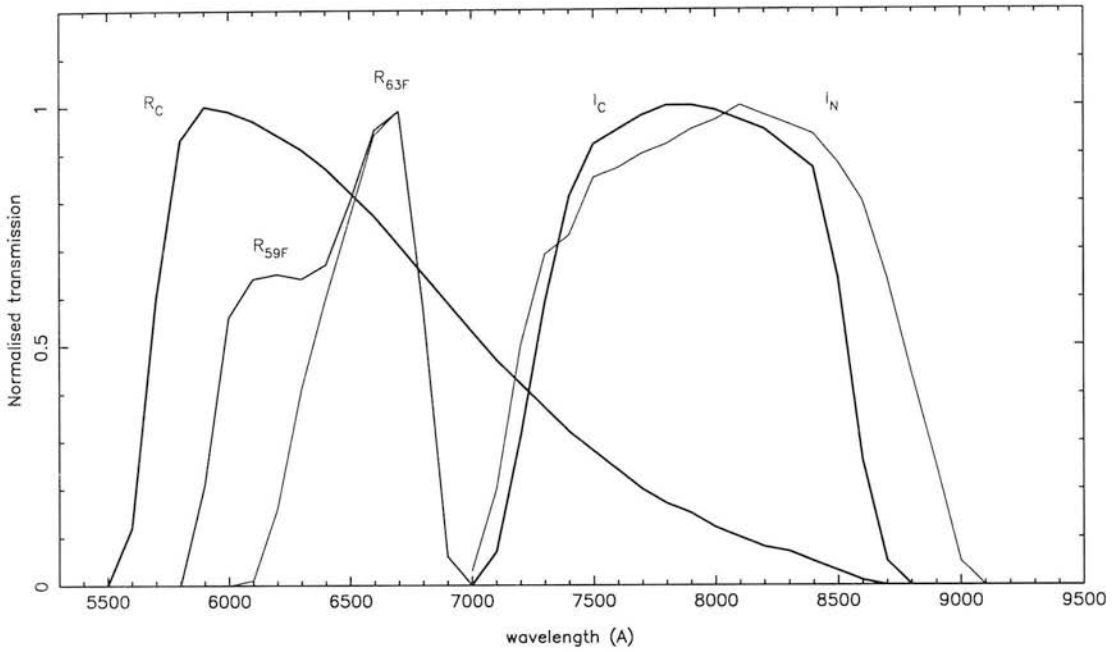

Figure 2.2: Transmission profiles for R and I band filters of the Cousins and photographic photometric systems.

figure 2.2).

The variation is due to the long, declining red-ward 'tail' of the Cousins R_C filter, a feature which does not occur in the photographic R filter; the 'R_F' band. Since the flux of cool stars rises rapidly in R–I region R_C is measuring much more of the stars light than R_F with the consequence that the Cousins R–I is much smaller. Also the extension of R_C into the I band leads to a 'saturation' of the the colour term in the coolest stars.

The most reliable and up-to-date corrections between the systems have been derived by Bessell (1986) and the relevant ones are given below. Leggett (1992) has also compiled a comprehensive list of colour corrections for many of the modern CCD systems used for visible and IR band photometry of cool stars. These terms transform most systems to Cousins' system and these values in turn can be transformed with Bessell's relations onto the photographic systems used by the UK and ESO Schmidt plates. The colour terms derived by Bessell which are relevant to this survey deal with the Cousins RI system and the two photographic bands R_{63F} and R_{59F}. R_{63F} refers to the combination of IIIaF emulsion and RG630 filter used

in early 'first epoch' UK Schmidt plates and the ESO Schmidt R survey. R_{59F} refers to the IIIaF emulsion and the OG590 filter which is used in the more recent 'second epoch' UK Schmidt plates. Bessell notes that separate colour terms are required for dwarfs and giants in the R_{63F} system. The following terms, as quoted are determined up to $(R-I)_C = 2.5$ and also extend to a single star at $(R-I)_C = 2.8$ with corresponding $R_F - I_N$ values are approximately 3.2 and 4.3 respectively.

$$R_{59F} - I_N = -0.005 + 0.934(R-I) + 0.095(R-I)^2 + 0.034(R-I)^3.$$

$$R_{63F} - I_N = -0.016 + 0.785(R-I) + 0.121(R-I)^2 + 0.027(R-I)^3.$$

Direct conversion between R bands can be made with following colour terms, which have the same range:

$$R - R_{59F} = 0.006 + 0.059(R-I) - 0.112(R-I)^2 + 0.0238(R-I)^3.$$

Relation for dwarf stars:

$$R - R_{63F} = 0.013 + 0.204(R-I) - 0.100(R-I)^2 - 0.0295(R-I)^3.$$

The I_C and I_N bands are essentially the same. The UKSTU handbook (Tritton 1983) gives the following nominal transformation:

$$I - I_N = (0.03 \pm 0.02).(V-I) \qquad 0.0 < (V-I) < 1.9$$

2.5.2 Bolometric corrections and effective temperature.

Having corrected a photometric measure to the appropriate system a colour-parallax relationship can be applied to derive an absolute magnitude which can be related directly to some physical property of a star. A colour such as R–I measures the ratio of the summed flux in two adjacent spectral regions. This ratio is related

to the underlying (Planck) flux distribution and so a relationship between effective temperature and colour can be found. Effective temperature and luminosity are related by $L = 4\pi r^2 \sigma T^4$ where r is the stellar radius and σ is the Stefan-Boltzmann constant. The best empirical determination of this relationship can de found using the Gliese catalogue. The determination of relationships between the photographic R–I index and the absolute magnitudes on the system is left until chapter 5. The most readily observable properties of a star are its luminosity and effective temperature and we relate our photometry to these via a *bolometric magnitude*, M_{bol}. The bolometric magnitude is a measure of the total luminosity of an object and is defined as

$$M_{bol} = -2.5 \log(L/L_{\odot}) + M_{bol,\odot},$$

where the luminosity L is that derived from the integrated flux distribution. The system is often based on the solar values, as quoted here, where $M_{bol,\odot} = 4.77$ due to the relative ease of measuring the solar energy distribution.

As cool stellar atmospheres deviate strongly from an ideal Planck distribution it is necessary to include a *bolometric correction*, BC to account for this. If we measure a photometric magnitude M_{λ} then

$$M_{\lambda} = M_{bol} - BC_{\lambda}$$

where λ is the appropriate photometric passband and BC_{λ} is the bolometric correction. This simple equation gives us the essential relationship between observation and theory.

In practice BCs have been calculated by fitting a Planck distribution to a spectral region that is assumed to be free of absorption/emission features and so measures the continuum flux. Where spectroscopic measures are not available, a method of the sampling the energy distribution over the widest possible spectral range by use of BVRIJHKLM photometry has been used. The total luminosity of the

star is found by interpolating between the spectrophotometric measurements and summing the flux under the derived profile and also under an assumed Rayleigh-Jeans tail red-ward of available data. The point used to 'anchor' the black body fit varies between authors, but there is a consensus that the fitting must be done in the infrared, near the peak of the flux distribution, and not in the absorption-dominated visible bands which contribute at least a factor ten less flux.

Berriman and Reid (1987) (corrected and updated by Berriman *et al.* 1992) chose the 2.2μm K band as their anchor point. The band is flanked by stellar and terrestrial H_2O absorption which leads to over-estimation of the flux contribution when interpolating across these features. Bessell (1991) used the broad-band photometry technique to derive far-red and infrared BCs for a larger sample of cooler stars than that used by Berriman and Reid and considered the relationship of R–I to absolute magnitude and temperature. Berriman *et al.* did not explicitly deal with R–I due to concerns over the quality of photometry and problems of establishing a flux zero point and effective wavelength for the Cousins R filter. Tinney *et al.* (1993) followed the method of Berriman and Reid but used the L' (3.82μm) band to anchor the flux distribution. This band is relatively clear of H_2O absorption though the problems of interpolation at shorter infrared wavelengths remains. As Berriman *et al.* point-out the temperatures quoted are *equivalent* temperatures that represent the effective temperature of the stellar photosphere *if* the flux at the 'anchor' point is true black body continuum. Since this is not the case, the measurements represent the best available estimates of effective temperature until the advent of detailed synthetic infrared atmospheres. The most recent attempt to use synthetic atmospheres is presented by Leggett *et al.* 1996.

These relations mostly deal with the important infra-red bands which measure the majority of the stars flux, but tend to avoid the photometric R band due to the aforementioned problems in calibration and excessive colour terms. The R band however remains an important tool for wide-area photographic surveys of cool stars and it is probably fair to say the continued importance of these surveys has kept the band 'alive'.

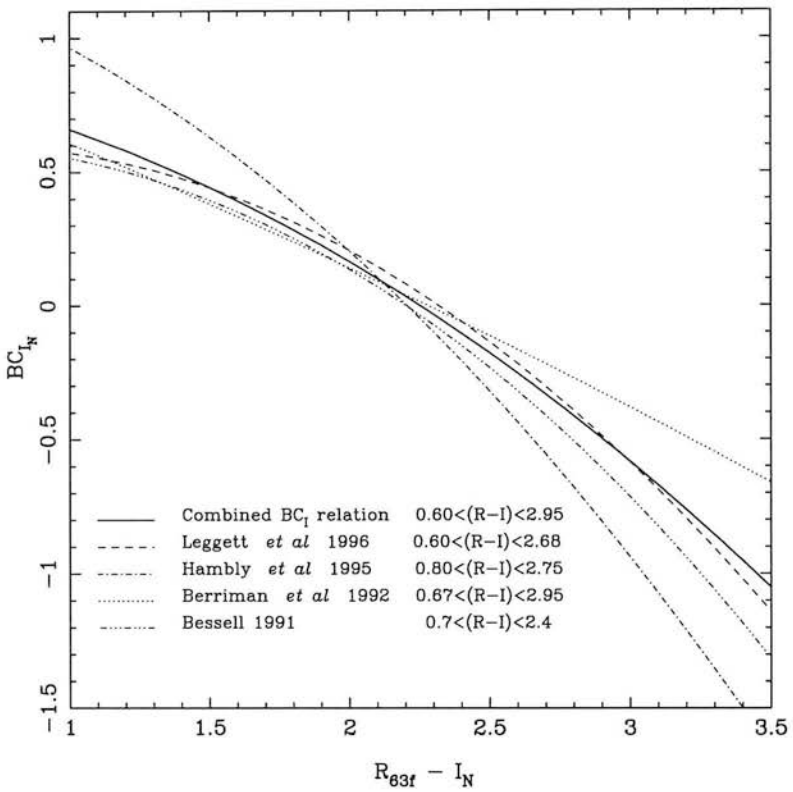

Figure 2.3: Bolometric corrections to I band based on R-I photometry

The I-band bolometric corrections determined by Leggett *et al.* 1996, Berriman *et al.* 1992 and Bessell 1991 are compared in figure 2.3 which also shows a composite curve representing a mean of the measurements from the four sources. Coefficients of the least squares polynomial fits to the measurements are given below, in terms of photographic R–I.

$$\text{Composite}: BC_I = 0.904 - 0.119(R-I) - 0.125(R-I)^2 \quad \sigma = 0.177 \qquad (2.1)$$

Leggett *et al.* 1996: $BC_I = 0.514 + 0.269(R-I) - 0.212(R-I)^2 \quad \sigma = 0.108$

Hambly *et al.* 1995: $BC_I = 1.349 - 1.262(R-I) + 0.219(R-I)^2 \quad \sigma = 0.237$

Berriman *et al.* 1992: $BC_I = 1.023 - 0.388(R-I) - 0.026(R-I)^2 \quad \sigma \simeq 0.1$

Bessell 1991: $BC_I = 0.590 + 0.139(R-I) - 0.167(R-I)^2 - 0.008(R-I)^3 \quad \sigma \simeq 0.1$

Figure 2.4 compares the $((R_f - I_N), T_{eff})$ relationship along with a combined function based on the source material quoted above. This new determination uses a wide range of temperature estimates based, where possible on several recently-published (post 1990) values. By using weighted mean values, the BC is less subject to the systematic errors in any one system. Where only one temperature measure is available an uncertainty of 10% is assumed, which is usually more than the quoted error, but closer to the scatter found in those stars with several measures. Three low mass stars not included in the bolometric studies along with three Pleiades brown dwarf candidates (see Rebolo *et al.* 1996b) have been included which illustrate the extension of the scale down to around 2000K and to show the differences between the young disc (Pleiades) and old disc stars (lower group). The R-band colour terms for the coolest of these stars however are not known which reduces the status of this extension to some thing of an 'encouraging extrapolation' and it is clear that agreement on the form of the relationship ceases for objects with (R–I) > 3. Coefficients for the composite fit are given below:

$$\text{Composite} : T_{\text{eff}} = 4335.8 - 822.6(R-I) + 65.7(R-I)^2 \quad \sigma = 159.0K$$

2.6 The stellar luminosity function.

A stellar luminosity function (LF) is defined as the number density of stars expressed as a function of luminosity, i.e. $dN = \phi(L)dL$ and is usually dealt with in its observational form as the number of stars per cubic parsec in the absolute magnitude interval $M_\lambda \pm \delta M_\lambda$, for a photometric band λ. The purpose of constructing a luminosity is two-fold; firstly, to study the effects of luminosity evolution in a given population and secondly to derive the corresponding mass function (MF) and mass density distribution for populations with no measurable luminosity evolution. This discussion concerns the work in this field relating to low mass dwarfs only. The luminosity evolution of very low mass stars, as discussed in section 2.2 is initially rapid and then essentially unmeasurable during main sequence lifetimes,

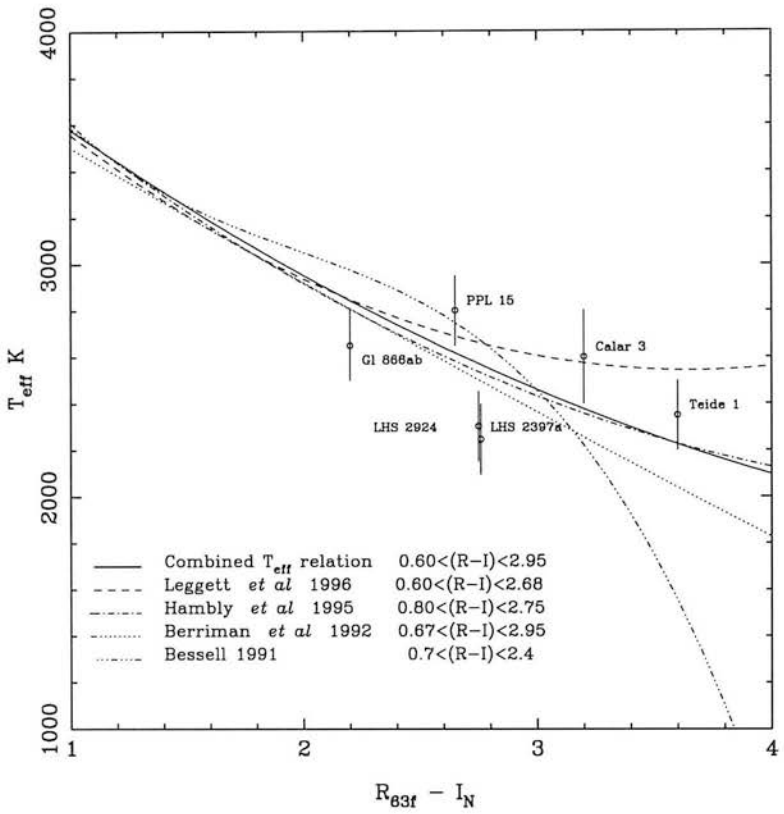

Figure 2.4: Colour-Temperature relation for R–I

which for these stars are comparable to the age of the Universe. Thus, the LF can be used to derive a mass function for low mass stars which represents the entire contribution of the Galactic disc star formation era to date and therefore the total mass density of these stars. For lower mass brown dwarfs, there is no period of stable luminosity (excepting 'transition' objects) and so the shape of the LF of these stars will be determined by their cooling rates.

The two basic measurements required to derive an LF are the luminosity (or M_λ) and distance for every sample member. This is only directly possible for a very small volume about the sun and for deeper surveys either kinematic or photometric parallax estimates have been used. These statistical methods introduce biases which are not significant in the nearby star data, but which must be understood and dealt with in order to a derive a deep and meaningful field LF. Stobie *et al.*

(1989) discuss these problems in detail and the salient features are summarised below.

- Completeness.

  The distance limit of a survey falls with increasing absolute magnitude since $5 \log d = (m + 5) - M$. This leaves the choice of setting a very small volume limit and rejecting valuable data on higher luminosity objects or retaining the brighter objects and incompletely sampling the fainter objects. The 'V_{max}' method (Schmidt 1974) addresses this problem by defining for the sample a set of maximum survey volumes. Defined by the survey solid angle and the maximum distance out to which each star could be detected in the survey, the sum of $1/V_{max}$ terms produces a luminosity function in which each star has been sampled out to the completeness limit for its luminosity. The method has been generalized to take into account variations in space density within a survey volume (Stobie *et al.* 1989).

- Contamination.

  The principal contaminants of photometric surveys of main sequence stars are distant giant stars, sub-dwarfs and galaxies. Stellar contamination can be removed by colour selection and galaxies by image morphology. The level of contamination is dependent upon Galactic latitude with giant contamination decreasing and galaxy and sub-dwarf contamination increasing with galactic latitude. Further details, with relevance to photographic surveys are left until chapter 4.

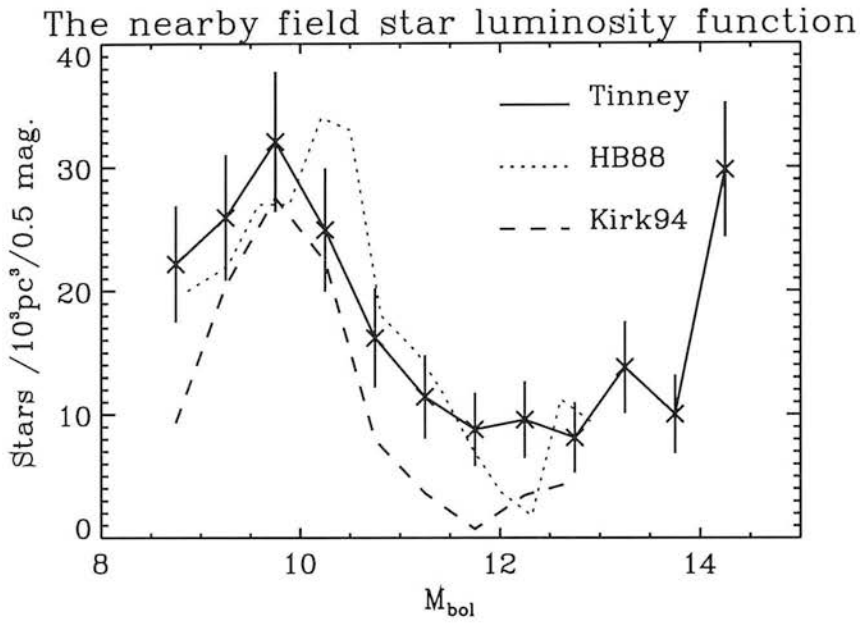

Figure 2.5: Recent measurements of the low mass stellar luminosity function. Hawkins & Bessell (1988), Tinney (1993) and Kirkpatrick *et al.* (1994). Conversion of HB88 to M_{bol} is by Reid (1987).

- Cosmic scatter

  The natural scatter in the empirical (colour, magnitude) relationships used to determine photometric parallaxes leads to a systematic mis-calculation of the distance of the brighter stars of a given colour with the consequence of increasing the mean magnitude for a given colour by sampling a larger volume than intended. Referred to as *Malmquist bias* (Malmquist 1927), this unavoidable feature of photometric surveys not only over-estimates the mean luminosity of stars at any given apparent magnitude but also over-estimates the number of stars at that magnitude. Correction for both effects is necessary and Stobie *et al.* point-out that corrections to previous surveys have not fully dealt with the affect of the bias on number counts.

2.6.1 Recent determinations of the low mass luminosity function

The photographic surveys of Reid & Gilmore (RG, 1982), Hawkins & Bessell (HB, 1987), Stobie *et al.* (SIP, 1989) and Tinney (1993) have consolidated our knowledge of the low mass field star LF. All have used wide-field photographic plates from Schmidt telescopes, all measured their plates with the COSMOS measuring machine and all used photometric parallax estimates based on V–I and R–I (RG & SIP and HB, Tinney respectively). Kirkpatrick *et al.* (1994) have also measured the field LF over an area equivalent to a photographic plate using a CCD array mounted on a transit telescope. As figure 2.5 shows, the LFs are in very good agreement. Most importantly, they all show a maximum near $M_{bol} = 10$ and a minimum near $M_{bol} = 12$. Beyond the minimum, the LFs diverge in their predictions as they approach the lowest main sequence luminosities. The origin of these features has inevitably been a source of debate.

On the question of the shape of the LF beyond $M_{bol} = 12$ there is no consensus other than to agree to differ. The reason is that no survey has yet to contribute more than a handful of stars to these faintest bins and so the true shape is still washed-out by statistical noise. The interpretation of any evidence of a rising LF as being suggestive of a significant brown dwarf population is not straightforward. The strong age-dependence of a brown dwarf LF and the steep mass-luminosity relation i.e. a sharply falling mass function can still yield a flat or rising LF. The minimum beyond $M_{bol} = 10$ is inconsistent with the LF derived from nearby volume-limited samples using trigonometric parallax measurements (Wielen *et al.* 1983, Dahn *et al.* 1986) which suggest a continuation of the maximum down to their completeness limits. The difference between these surveys and photographic surveys lies in the resolution of multiple star systems. The typical angular resolution of a photographic plate is 2-3", estimates of binary frequency amongst disc stars range from 30 - 100% (Reid, 1987) and Fischer & Marcy (1992) claim that around 70% of binaries are separated by less than 100 a.u. As a consequence, the majority of systems will go unresolved by photographic surveys which extend beyond 50 parsecs. This fact has been suggested as a reason for the fall-off of star

counts beyond $M_{bol} = 10$ in photographic surveys (Kroupa *et al.* 1991). The result of this is that we must distinguish between the local stellar LF which deals with stellar multiplicity and the *system* or *field* LF which does not. The minimum may or may not be real in the stellar LF but appears to be genuine in the system LF.

2.6.2 Brown dwarf luminosity functions.

Without an age measurement for every brown dwarf in a sample used to measure the LF, the BD mass function can not be found and this limits us to measurements of the MF based on binary systems. Unfortunately this has not yet been a problem since there are no brown dwarf samples to provide a real LF. Several authors have made predictions however. To predict a BD LF requires a model that accurately relates cooling rates and luminosity evolution to observational properties, in short a reliable model atmosphere. The earliest predictions did without such a luxury, assuming a simple black-body flux distribution (Staller & de Jong 1981) whilst other authors have limited themselves either to predicting an LF that deals explicitly with luminosity (Hubbard *et al.* 1992, Laughlin & Bodenheimer 1993). Nelson *et al.* (1986) and Nelson *et al.* (1993) present BD LFs in various standard visible and infrared bands based on their detailed stellar models. Apart from scale differences due to differing assumptions of the local mass density, the various predictions show a similar 'saw-tooth' trend. The LF falls sharply at the luminosity corresponding to the HBMM and then climbs steadily into the BD regime. For longer wavelengths (far-IR) the LF turns over again and falls to zero more rapidly than at shorter wavelengths. Perhaps due to the simplicity of the physical assumptions there is little structure in the predicted LFs for a given passband but the value of the LFs lies in the relative differences between these passbands since the distribution of objects viewed in several passbands contains information about the mass distribution via the relative cooling rates inferred from gradient of the climbing slope of the LF.

Prospects for future work in the field of low mass stellar LFs lie in studying the

binary distribution to resolve the differences between nearby and distant (system) LFs and in continuing to sample larger volumes at fainter fluxes in order to determine the true shape of the LF as it leaves the main sequence and enters the brown dwarf regime.

2.7 The stellar mass function

The stellar mass function, ψ is defined as the number density of stars in intervals of mass $M \pm \delta M$ *i.e.* $dN = \psi(M)dM$ The function is often represented by a power law of the form

$$\frac{dN}{dM} = \psi_0 M^{\alpha} \tag{2.2}$$

As with the luminosity function, the MF represents the space density in the Galactic plane, and in this discussion the abbreviation MF refers to the population I main sequence stellar mass function and its continuation/extrapolation into the brown dwarf mass function.

From the stellar mass function the total mass density in the Galactic plane can be derived which integrated vertically with a space density distribution function yields the surface mass density of the Galactic disc. Combining this with derived values for other less numerous populations (white dwarfs, giants, halo stars, gas etc) give a total mass density which can be compared to dynamic measures based on stellar motions. Discrepancies between the two measures lead to claims of *missing mass* in the form of *dark matter* and the relevance of this topic to low mass stars is discussed in the following section. Needless to say, controversial claims of dark matter demand a careful look at the methods used to derive the stellar mass function.

The mass function is related the luminosity function by a mass/luminosity relationship (M/L):

$$\psi(M) = \phi(L).(dL/dM)$$

Empirical measures of the M/L are sparse, especially for low mass stars (Henry & McCarthy 1993) and are based on measurements of binary systems. Since the physical conditions during the formation and evolution of multiple star systems inevitably differ from those experienced by single stars we cannot be sure that empirical M/Ls fairly relate mass and luminosity functions derived from deep surveys of field stars. These doubts and the paucity of low mass data lead most authors to use theoretical M/Ls such as those illustrated in figure 2.1, which also have the advantage of providing a range of epochs and self-consistent relationships with other stellar parameters.

Figure 2.1 also reveals the largest source of uncertainty in the transformation: the rapidly increasing steepness of the slope below $M/M_{\odot} \approx 0.3$ and the variation between models at a given epoch. The dependence of the slope on mass in this region rises from around M^3 to a more than M^{20} at the main sequence/brown dwarf transition. The model-to-model variation is only significant for M dwarfs at the earliest epochs where physical and environmental conditions are uncertain but for transition objects and brown dwarfs the differences amount to factors of up to 0.4 in luminosity for a given mass. The differences are most notable for lower mass BDs at later epochs, which are cooling into a range that is currently well beyond the scope of atmospheric models.

The 'seminal' mass function for Galactic field stars was derived by Salpeter (1955). The function extends down to $0.3M_{\odot}$ and is best fit by a power law of slope -2.35. By assuming a (constant) star formation rate and considering stars of masses below the main sequence turn-off point, the function actually measures the *initial mass function* (IMF). The IMF represents the mass function of a population at the point of creation, prior to the effects of stellar evolution. This is something of an abstract idea when applied to the Galactic disc population whose members are far from coeval. It serves as a useful baseline by which other MFs can be compared and is important especially when comparison is made to cluster MFs. Twenty-five years of updating and improving stellar structure and evolutionary models, and further studies of the age and history of the Galactic disc led to the derivation

of the 'canonical' field star mass function by Miller & Scalo (1979). Their IMF extends to $0.1M_{\odot}$ and can be fit by a log-normal power law with an index that varies from -1.0 to -3.8 from the lowest to the highest ($\approx 100M_{\odot}$) masses implying a flattening of the function towards the HBMM.

Investigation of the distribution below $0.1M_{\odot}$ has been carried-out by the authors responsible for the luminosity functions discussed in the previous section. Two consistent features of the MFs derived from deep (photographic) surveys are a peak around $0.25M_{\odot}$ and a sample that peters-out to statistical insignificance just short of the HBMM. The first of these features has hampered attempts to characterise the function by a single power law index; the 'bi-modal' mass function has raised discussion of the possibility of preferred mass scales in the star-formation process. Other authors have countered this argument by comparing the MFs to those derived from nearby star samples; again the problem of unresolved binarity in deep surveys has been seen as a possible reason for the fall-off of number counts in bins below the $0.25M_{\odot}$ peak. Kroupa *et al.* (1991) have addressed this and find that they can reconcile deep and nearby MFs for the lowest mass stars by assuming large binary fractions, in fact their best fit requires that all stars be in binary systems with a hydrogen-burning member. 'Acceptable' fits are possible with binary fractions of 0.43 to 0.56 in their model. Mera *et al.* (1996) have re-calculated previous wide field mass functions using a new set of stellar models and derive what they consider to be a theoretical MF that is consistent with the Kroupa *et al.* empirical determination. Their mass function rises sharply toward the HBMM ($-2.5 < \alpha < -1.3$) and they extrapolate this trend to infer the presence of relatively large numbers of brown dwarfs. As with all field MFs, the function can do little more the extrapolate the main sequence trend into the BD region due the the lack of age information in surveys, which as noted, is essential to transform brown dwarf cooling rates into M/Ls.

The study of open Galactic clusters offers a chance to study a coeval sample of stars and thus measure a brown dwarf MF directly. Being young, evolving low mass stars can be seen at their brightest. Favoured clusters are the nearby Hyades and

Pleiades, Praeseppe and young star-forming regions such as ρ Ophiuchus. Wide field survey techniques are used and follow the methods used for field star surveys, with the added complication of ensuring that each star in the sample is a genuine cluster member. This often involves kinematic selection criteria.

Table 2.3 reduces the results of several such surveys to a best-fitting power law index and compares these to values derived from recent field star surveys. The similarity between the indices, especially between field and cluster surveys may have implications for theories of star formation (Scalo 1986). A fact not shown in table 2.3 is that in all cases the IMF is flattening towards to HBMM, which may be a consequence of incompleteness in surveys or a real physical feature. Although several cluster surveys have produced promising brown dwarf candidates, notably in the Pleiades (Hambly *et al.* 1991, Rebolo *et al.* 1995) our continuing lack of knowledge of the very low mass IMF leaves us having to extrapolate our measurements of low mass main sequence stars into the brown dwarf region. The declining IMF inferred in this case does not necessarily imply a fall-off in the number of BDs with respect to M dwarfs since the integrated number of low mass BDs could be huge. The slope does however cast doubt on suggestions that low mass objects may balance the Galactic disc's suspected mass deficit.

Table 2.3: Recent measures of the initial mass function in Galactic clusters and wide-field surveys with best power law index quoted.

Survey	α	Ref.
Pleiades	-1.0	Hambly *et al.* (1991)
Hyades	0 to -1	Leggett *et al.* (1994)
Praeseppe	-1.5	Hambly *et al.* (1995)
Rho Oph.	-1.3 to -1.1	Comeron *et al.* (1993)
Nearby	$\approx$ -1.4	Miller & Scalo (1979)
Nearby	-0.47 to -1.1	Kroupa *et al.* (1991)

2.8 The local mass density.

The suspicion that the local Galactic disc contains dark, undetected matter has long been a source of motivation in low mass star surveys. Very low luminosity stars such as brown dwarfs are natural candidates and much work has gone into extrapolating the stellar mass function and comparing the integrated mass density to what has come be known as the *Oort limit*. Based on Oort's original estimate of the local Galactic mass density (1932, 1960) the work suggested that dynamic estimates of the local density exceeded observational estimates by 30 to 50%. Dynamical tracers used in previous surveys include Globular clusters, RR Lyrae variable stars and Halo stars all of which trace the Galactic velocity field beyond the edges of (visible) Galaxy (See Trimble 1987, table 1 for references). These methods allow a measurement of the total Galactic mass and imply a mass/luminosity ratio (M/L) of 10 – 50, which as Gilmore (1990) points out, is roughly consistent with orthodox cosmological estimates for baryonic matter. This value is considerably higher than the M/L $\approx$ 3 for the Galactic disc as inferred from the local stellar population and may suggest dark matter distributed with a large scale height or several populations with differing distributions. This second possibility incorporating a dominant dark halo population sufficient to flatten the Galactic rotation curve at large radii and a lesser disc component distributed as population I stars or the inter-stellar medium (ISM) is the most promising.

The standard method used to determine the local galactic mass distribution is based on the collisionless Boltzmann equation, reduced to the *Jeans equation* by the assumption of an isothermal population (of constant velocity dispersion) in equilibrium in a time-independent gravitational potential. The surface density Σ ($M_{\odot}pc^{-2}$) can be derived directly from the measured force component and application of Poisson's equation yields the volume mass density ρ ($M_{\odot}pc^{-3}$). The phase-space distribution required in this analysis can be expressed as a function of galactic height (z) and vertical velocity which can be measured directly. Principal uncertainties in the method come from photometric errors and biases which lead

to systematic errors in the distance scale used. This is especially important in determining ρ which is proportional to the square of the distance. The assumption of isothermality is an unrealistic one and Kuijken and Gilmore's (1989c) treatment of the Hill *et al.* (1979) F dwarf sample shows how even two populations with similar velocity dispersions can produce positive, negative or zero dark matter results depending on how they are combined. Thirdly, Σ and ρ are related via an assumed scale height in an assumed gravitational potential and these assumptions are set by expectations of the dark matter distribution. In practice many models based on differing fractions of light and dark matter with various distributions must be generated and compared to the often noisy measurements.

Differing populations require different tracers, as the tracer group must have a similar distribution to the suspected dark matter. Recent surveys of dynamical mass have studied disc population tracers to directly determine the local mass density (Kuijken & Gilmore 1989a,b, Bahcall *et al.* 1992). F dwarfs and K giants have been used, intended to represent isothermal disc populations. Until young stars are 'smoothly' distributed in the Galactic plane (dynamically relaxed into the Galactic potential) they can not be used as tracers in this way. Thus, studies of the *local*, i.e. mid-plane density have used samples that represent the older, more widely dispersed members of the disc. Such samples can adequately trace any dark matter with a old disc distribution but these samples are insensitive to matter that may be distributed closer to the plane with the ISM.

The use of F and K stars is mainly traditional and their repeated use has ensured a constant improvement in the quality of measurements. A tracer population must be numerous enough to be statistically significant and must be readily identifiable with a well-determined absolute magnitude scale. Both F and K stars meet these criteria, K giants being the original population of choice due to their intrinsic brightness and easily identifiable spectral features. They suffer from an absolute magnitude scale that is complicated by age, metallicity and altitude since this spectral class draws stars from a wide range of masses, ages and distributions. F stars have also been criticised (Kuijken & Gilmore 1989c) due to the effect

of the increasing evolutionary timescale across the spectral class which leads to earlier types showing velocity structure which breaks the required assumption of isothermality. The possibility of sub-dwarf contamination at the 20% level has also been suggested which casts doubt on earlier surveys that used insensitive selection techniques.

Results of recent dynamic surveys

Table 2.4 summarises the upper and lower limits to measured surface and mass densities (evaluated at mid-plane) published in the last ten years. Salient points are noted below.

Table 2.4: Recent measurements of the local surface and mass density.

$\Sigma_{0,min}$ $M_\odot pc^{-2}$	$\Sigma_{0,max}$	$\rho_{0,min}$ $M_\odot pc^{-3}$	$\rho_{0,max}$	Dark matter fraction	Source
52.0	76.0	0.084	0.11	10%	Bienayme *et al.* 1987
37	55	0.10	0.21	0%	Kuijken & Gilmore 1989b, 1991
66	72	N/A	N/A	43%	Gould 1990
60.0	112.7	0.1426	0.4535	53%	Bahcall *et al.* 1992

Bienayme *et al.* . This work differs from the others in that the authors use a Galactic model to derive a best-fitting potential based on general star counts. The advantage of this technique is that it removes the dependence on rare, hard to define homogeneous stellar populations. The main criticism (Bachall *et al.* 1992) is that one must essentially take into account every statistical property describing the disc population to ensure the removal of systematic effects.

Kuijken & Gilmore. The upper-limit quoted for ρ is taken from Bahcall (1984). The KG survey uses a high-altitude disc tracer that is relatively insensitive to near-plane mass distributions and they use their data to illustrate how previous studies of the sample (such as Bahcall 1984) can produce ambiguous results. The

second paper (KG 1991) attempts to address various criticisms (e.g. Gould 1990) and re-asserts the original result.

Gould. A re-appraisal of the Kuijken & Gilmore analysis attempting to account for the effects of Galactic rotation constraints within the maximum likelihood method employed by KG89. Gould points-out that the KG89 paper is the first time that the local missing mass has been measured to be zero.

Bahcall *et al.* conclude that their findings are *inconsistent with models involving no dark matter*. They quote 'odds of 6–1' against the local disc having no dark matter and the best fit to their data is a model with 53% more dark than luminous matter. The closest single exponential fit to their inferred density distribution has a scale height of 320 pc, representative of an old disc population.

Unlike other aspects of low mass star research a clear consensus has yet to emerge from this field of study. The paucity of independent samples that meet the strict criteria required has hampered work and given the authors ample opportunity to criticise each others analysis. As Gould (1990c) suggests, the differing conclusions of KG89 and Bahcall *et al.* are not necessarily inconsistent as their methods are unsuitable for the analysis of each others data and are better thought of as complementary methods for different tracers. The role of the ISM remains murky amongst the studies due to the mid-to-high altitude nature of the tracers. If there is a consensus it is that local dark matter does exist and may be associated with the ISM or cool degenerate stars. Difficulties in recovering the volume mass density from the surface column density are due to uncertainties in the mid-plane potential models (the ISM again) and may also contain the hidden influence of the Galactic halo. In this case, the contribution from low mass may not account for much more than 0.05 to 0.1 $M_{\odot}pc^{-3}$. Such a value would be difficult to verify observationally were it in the form of cool white dwarfs due to their rarity, but even for such a small mass density, an extrapolation of even the most pessimistic of mass functions would imply the presence of hundreds of faint brown dwarfs in the solar neighbourhood. Thus, even if astronomers must relinquish their previous

raison d'etre for studying low mass stars they still may have an opportunity to study a whole new population of stars on their doorstep.

Chapter 3

A Low Mass Star Survey: Materials, scope and expectations

This chapter discusses the instruments and material used to provide the raw data for the survey. The scope of the survey is determined by the quality of existing plate material and the limitations of the measuring machines involved, which are discussed in the following chapter. We shall see that due to cooling the most luminous brown dwarfs are concentrated near to the Galactic plane with the consequence that wide-area, near-by surveys are likely to fare better than narrow pencil-beam surveys in hunting these objects. Our chosen detector is the photographic plate, in particular those used by the UK and ESO Schmidt telescopes.

3.1 The Schmidt telescopes

The principle behind Bernhard Schmidt's 1930 telescope design is to achieve a large field of view by placing an aspheric 'corrector' lens at the centre of curvature of a spherical mirror. The resulting field is measured in degrees rather than minutes of arc and is ideal for wide-field survey work. The United Kingdom 1.2 m Schmidt Telescope (UKST) sited at Siding Spring Observatory, Australia began the first of its southern hemisphere blue, red and infrared sky surveys in 1974. The original

intention had been to copy the design and complement the survey programme of the 1.2 m Oschin Schmidt at Mount Palomar, USA. The Palomar POSS-I survey programme ran from 1950 to 1958 and the technical advances of the following years resulted in the final USKT design being different in every way from the original Oschin telescope (apart from the shutter design, Reddish 1992). The principal improvement was the use of an achromatic 1.2 m correcting lens, ensuring high quality wide field images at longer wavelengths (>650 nm). In 1973 the European Southern Observatory's 1.0 m Schmidt telescope (EST) began a similar task at La Silla, Chile.

Both the UKST and EST map their surveys onto the 1110 SERC equal area survey fields (UKSTU handbook 1983). The field size is based on the field of view available to a 1m class Schmidt; at least 6 x 6 degrees. The fields form an overlapping mosaic with a spacing of 5° covering the entire southern sky and extending northward by 15° for continuity with the Palomar fields (which do not overlap). The ESO blue and red surveys, which continued until 1990 cover the region with $\delta \leq -20°$ (606 fields). This border is also used in the USKT surveys to define the main ($\delta \leq -20°$) and equatorial ($0° \geq \delta \geq -15°$) programmes. The UKST short-exposure surveys are available for galactic latitudes satisfying $|b| < 10°$. The current strategy at the UKST is to complete the infrared SERC-I survey and to provide survey-quality first and second epoch material, separated by 15 years. The SERC-J (blue) survey is expected to provide the first epoch measurements, with the on-going AAO-R (red) survey providing the second epoch. A report on the progress of current UKST surveys is provided by Morgan (1995).

3.2 Photographic plate material

The UKST plates cover 6.4 by 6.4 degrees and are 356mm square and 1mm thick. The blue, red and infrared surveys use four emulsion/filter combinations between them and usually have a minimum exposure time of 90 minutes. With a quantum efficiency of a few per cent material with a depth of 18-24th magnitude is obtained,

Survey	Waveband	Emulsion	Filter	Flux limit (magnitude)	sky coverage
ESO-R (red)	R_{63F}	IIIaF	RG630	22	$\delta < -20°$
SERC-J (blue)	B_J	IIIaJ	GG395	23	$\delta < +5°$
AAO-R (red)	R_{59F}	IIIaF	OG590	22	$\delta < -20°$
SERC-I (infrared)	I_N	IVN	RG715	19	$\delta < +5°$

Table 3.1: UK and ESO Schmidt deep sky surveys (UKSTU Handbook, Tritton 1983)

as summarised in table 3.1.

Aside from the survey, the UKST unit (UKSTU) plate library (Edinburgh) holds a large number (>10,000) of non-survey plates. The archive of early R plates (RG630) is particularly useful to this survey for reasons discussed in the following section. Both ESO and the UKSTU assign a grade to each plate based upon the resolution. Typical seeing on survey-grade plates is 2-3" corresponding to image sizes of $30\mu m$ or larger. The ESO grade is a straightforward measure of this resolution in microns. The UKSTU scale is more subjective, being a combination of a single letter (a-e) and an optional string of letters. The first letter assesses the 'overall quality of the plate' with subsequent letters indicating various blemishes, image distortions and so on. Survey-grade material receives an A grade and is usually accompanied by a further number which represents increasing quality from three to one.

To achieve survey-grade depth the plates are exposed for 90 minutes or more. All plates are hyper-sensitised before use and the plate and holder are flushed with dry nitrogen prior to use to remove water vapour. Plates exposed before the nitrogen-flushing practice was introduced in 1982 show a systematic desensitisation due to water vapour trapped in the *curved* plate holder. The trend of the desensitisation is to increase radially from the plate centre and is believed to closely follow the

radial vignetting effect (to within 0.04 mag.). The affect of radial vignetting is small (less than 0.05 mag. below 3°), but then rapidly increases with losses of greater than 0.2 mag. above 4° (UKSTU handbook, Dawe & Metcalfe 1982).

There are several well-catalogued forms of unwanted images on Schmidt plates. These can be grouped into optical (diffraction spikes, halos and ghosts), exposure-time (light trails from artificial satellites and aircraft) and emulsion flaws (development stains, blemishes and microspots). Optical flaws are mostly due to internal reflections and are only severe for the brightest objects. Halos are formed due to back-reflection from the plate emulsion and are reduced by the application of an anti-halation coating on IIIaF and IIIaJ emulsions. The IV-N infrared plates can not be given this backing due to conflicting requirements of their hypersensitisation method and so they tend to show more intense halos of radius 1.5mm. Horizontal and vertical spikes are visible on stellar images below magnitude 16 and are caused by diffraction about the four plate-holder arms. The spikes are not necessarily unwanted, since the length is closely related to the magnitude of the star and also allows a degree of star/galaxy discrimination for the brightest objects (see §3.4). As these effects are correlated with brightness (see UKSTU handbook) it is possible to account for them during photometric calibration.

Light trails during exposure time can be easily removed from digitised images as they show extreme axial ratio values when reduced to an elliptical image. If the light source passes in front of a faint star it can introduce a photometric uncertainty which is difficult to remove, though the typical number density of images is sufficiently low to prevent this from being a serious problem. Another type of exposure-time flaw is that of under- or over-exposure which can result in large scale intensity variations. (i.e. much larger than that of individual images). Large-scale intensity variations can occur with emulsion flaws too, particularly at development time. Other emulsion flaws tend be singular image-like effects such as blemishes which can appear as very light (and hence bright) spots or erratic trails. The circular type of blemish can be identified by lack of image structure and the string-like blemishes can be rejected as they do not mimic the appearance

of any (known) astronomical object outside the Galactic plane.

Microspots or 'gold spots' are point-like reflective images which seem to occur due to irreversible chemical reactions with the emulsion and various atmospheric reagents. The spots can appear anywhere on a plate but concentrate in regions of high emulsion density such as bright stars, clusters and especially the step wedge: the graduated intensity calibration area at the edge of each plate. A second yellow variety has also been noted and differ in that they do not appear in reflected light and have a less well defined image boundary. There is statistical evidence to suggest that they are a pre-cursor to gold spots, although they are less strongly distributed about bright images. Measurements have been taken to retard the growth in number of these spots and Tritton (1994) reports recent progress. Removal of these objects from the survey data relies on the fact that they accumulate in regions of high emulsion density which are likely to be rejected, as discussed in chapter 4. Spots not accounted for in this way are assumed to be removed by the star/galaxy discrimination algorithm also described in chapter 4, since their lower surface brightness gives them a non-stellar appearance.

3.3 Expectations

The intention of this section is to assess the scope of a photographic survey for very low mass stars. The following points are discussed:

- Is a wide-field photographic plate a suitable detector?
- What is the likely distribution of very low mass stars?
- How will this distribution appear in a photographic survey?

3.3.1 Suitability of photographic plates

Photographic plates are regarded by some as an archaic choice of weapon in a very modern battle. The study of extremely cool, low luminosity stars would

seem to be best conducted with an efficient near-infrared detector. These devices have proved their worth in the field by revealing several brown dwarf candidates in the Pleiades (Rebolo *et al.* 1996) and by detecting other extreme objects such as Gl 229B (Nakajima *et al.* 1996). The nature of this survey though is not to select specific compact objects for deep photometry but to cast the net wide across the sky with intention of detecting nearby examples within the Galactic disc population. When the location of the quarry is unknown, maximising the sampling of the population is the key to success. In some cases this is just a matter of using the largest volume, for which a deep, narrow CCD frame can be of value. For Galactic disc surveys this technique can fall foul of both the declining density of objects with depth, and the increasingly crowded fields that are obtained.

Figures 3.1 compares the efficacy of a $6° \times 6°$ Schmidt plate (solid line) and a $10' \times 10'$ CCD (dashed lines) in detecting a population of $M_I = 15$ stars characterised by a simple exponential space density distribution of the form

$$\rho \propto e^{-z/H_z}, \tag{3.1}$$

where z is the vertical distance from the Galactic plane and H_z is the *scale height* of the population. $M_I = 15$ is assumed to be a likely value for a candidate object (see table 2.2). The CCD curves represent a range of limiting magnitudes from 22 to 25 and the Schmidt plate limit is set at I=19, values which represent similar exposure times on various telescopes and thus similar effort. Both figures show the total number of $M_I = 15$ stars that would be detected at a specific galactic latitude. The actual numbers are arbitrary and for the purpose of comparison only. The difference between the figures is in the value of the scale height used to integrate the sample. Figure 3.1 (a) uses H=50 parsecs and (b) uses H=350 parsecs. The former figure is suitable for a young disc population, perhaps less than 0.5 Gyr such as O, B and A stars. The latter value is typical for the old disc population as characterised by K and M dwarfs (Mihalas & Binney 1981). The CCDs are clearly less effective at higher galactic latitudes where the deep, thin volume suffers from the fall-off in number density of the stars. This is most severe for the H=50pc

sample which are more closely-bound to the Galactic plane. The figures tell us that for a similar effort, a Schmidt plate will yield more low luminosity stars when working at mid-to-high galactic latitude ($b > 40°$) and that the situation improves in the photographic plate's favour with decreasing scale height where area is more important than depth; a feature which is quantified below.

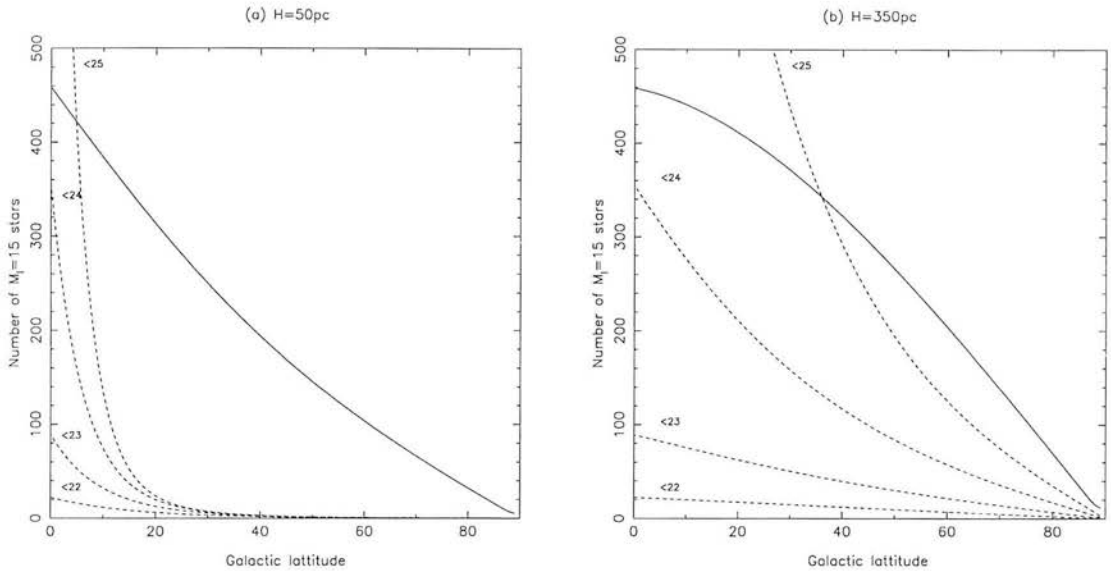

Figure 3.1: Relative number counts for a population of fixed luminosity as a function of Galactic latitude. UKST Schmidt plate and 10' CCD frame are compared for various limiting magnitudes (labelled) and for two scale heights: 50pc (a) and 350pc (b).

3.3.2 Space density

The integration of the previous section can be repeated with a more realistic space density function in order to gain some idea of the distribution of measurable properties of a low mass star population. In choosing a suitable luminosity function we have to make the decision of whether to use the results of previous observations or to 'build' a theoretical one. The advantage of using an observed LF of course is that there is some evidence for the fact that it does represent the true distribution. The marked difference between the nearby (individual star) and photographic (system) field LF has already been noted (§2.6) and is likely to be due in

part to unresolved binarity in photographic surveys. Choosing a photographically determined LF may seem appropriate to this study, but it seems likely that the nearby LF is a more accurate measure of the real physical distribution of low mass stars.

A counter-argument against using an existing LF as an input distribution is that it immediately adds its own biases to our study. If the chosen LF has under-sampled a particular population, then it will be under-represented in our predictions. For this reason the generation of an LF based on particular mass function is preferred. The chosen mass function is a generic power law (equation 2.2). As discussed in §2.7, $\alpha \simeq -1.5$ is a commonly derived value for low mass stars. This value along with a 'flat' function with $\alpha = 0.0$ and the Salpeter function, $\alpha = -2.35$ are compared here. Other authors (e.g. Tinney 1993) have presented non-smooth lower mass MFs but inclusion of these will complicate what is meant to be a simple study and so we shall use a smooth extrapolation of the functions discussed above:

$$\psi(M,t) = N(t)M^{\alpha}, \tag{3.2}$$

expressed in solar masses per cubic parsec (per unit magnitude) at the mid-Galactic plane (z=0). $N(t)$ is a normalisation factor which is a function of time via a stellar birthrate function. Conversion to a luminosity function is straight-forward:

$$\left(\frac{dN}{dL}\right)_t = \left(\frac{dN}{dM}\right)_t \left(\frac{dM}{dL}\right)_t . \tag{3.3}$$

The mass/luminosity relation can be obtained from a suitable stellar structure model. Since luminosity is not a directly observable quantity it is more useful to express the LF in terms of something that is directly observable. In this case absolute M_R and M_I magnitudes (in the photographic system). This requires a bolometric correction, and one that is potentially reliable when extrapolated down to the lowest luminosity brown dwarfs. Firstly, the stellar model of choice here is that published by Burrows *et al.* , 1993 (BHSL93) since the published tabular

version has a wide range of epochs (10^6 to 10^{10} years) and sufficient mass points to track any rapid variations in the transition region.

The bolometric corrections to the photographic R_F and I_N band have been calculated using a relationship derived from a compilation of published bolometric measurements. Table 3.2 summarises these data and figure 3.2 illustrates the derived relationships between M_I, luminosity and temperature. Not all of the tabulated data are used to derive the BCs. The most recently discovered brown dwarf candidates GD 165B, PC0025+0441, Teide 1, PPL 15 and Gl 229B are included for comparison only and the linear extrapolation that the fainter ones imply is encouraging. Using the BCs in the region occupied by these objects is done purely in the interests of exploring the consequences and is not expected to be a reliable extrapolation. The functional forms of the BCs are given below, the scatter in both cases being $0^m.3$:

$$M_{I_N} = 2.622 - 3.405 \log_{10}(L/L_\odot) \tag{3.4}$$

$$BC_{I_N} = -30.287 + 8.743 \log_{10}(T_{eff}) \tag{3.5}$$

Similar relationships for the R_F band are given below. As expected the r.m.s. scatter is larger: $0^m.4$ in both cases.

$$M_{R_F} = 3.120 - 4.015 \log_{10}(L/L_\odot) \tag{3.6}$$

$$BC_{R_F} = -56.429 + 15.755 \log_{10}(T_{eff}) \tag{3.7}$$

The application of the derived BCs to the BHSL93 models produces a set of isochrones relating mass to absolute magnitude, as illustrated in figure 3.3. By interpolating between the isochrones, a mass/luminosity relation can be derived for any epoch. Note that equation 3.3 must be evaluated at a specified epoch, t and so the present day distribution can be found by summing the *initial* mass function,

Name	M_R	M_I	M_{bol}	π (mas)	T_{eff} (K)	Ref.
GL406	14.81	12.63	12.27	145.1 ± 2.0	2651 ± 75	2,3,4,5
GL411	9.46	8.32	8.80	394.5 ± 1.2	3335 ± 106	2,5
GL644ab	8.96	7.59	8.13	155.7 ± 0.7	3450 ± 150	1
GL644c (VB 8)	15.53	13.22	12.68	155.7 ± 0.7	2544 ± 87	2,3,4
GL699	12.07	10.42	10.76	546.7 ± 0.8	3127 ± 87	2,4,5
GL752a	9.28	7.99	8.52	172.8 ± 0.8	3200 ±150	2
GL752b (VB 10)	16.28	13.98	13.16	172.8 ± 0.8	2484 ± 87	3,4,5
GL820b	7.21	6.41	7.40	287.0 ± 0.9	3900 ±150	1
GL831	11.2	9.51	9.78	125.5 ± 1.9	2920 ± 150	4
GL876	10.61	9.07	9.46	211.1 ± 4.8	3090 ±150	4
GL866ab	12.98	11.01	11.06	293.0 ± 2.7	2759 ± 87	2,3,4
GJ1002	13.80	11.80	11.90	212.8 ± 3.3	2910 ± 150	4
GJ1111	15.00	12.80	12.44	275.8 ± 3.0	2642 ± ±87	2,3,5
LHS2065	16.43	14.49	13.46	118.0 ± 1.7	2302 ± 106	3,4
LHS2397a	16.45	14.15	13.11	70.9 ± 2.4	2373 ±106	3,4
LHS2924	17.39	15.09	13.81	93.3 ± 1.5	2437 ±246	3,4,5
HB18	17.04	14.40	13.48	41.0 ± 4.0	2626 ± 150	3
HB19	16.44	13.75	12.79	32.4 ± 4.0	2618 ± 150	3
TVLM 513-46546	17.36	15.14	14.02	101.8 ± 5.2	2080 ±150	4
TVLM 513-8328	16.52	14.13	13.20	24.1 ± 4.5	2180 ±150	4
TVLM 832-10443	16.38	14.04	13.17	36.4 ± 3.0	2230 ± 150	4
TVLM 868-110639	16.87	14.59	13.44	61.2 ± 4.7	1975 ±150	4
TVLM 868-54745	–	12.43	12.33	32.0 ± 10.0	2450 ±150	4
TVLM 868-84947	14.78	12.56	12.41	18.0 ± 6.0	2350 ±150	4
ESO 207-61	17.03	15.31	14.35	65.4 ± 4.0	2618 ± 150	3
RG0050.5	–	14.63	13.59	39.4 ± 4.0	2600 ± 150	3
BRI0021-0214	16.97	14.65	13.42	82.5 ± 3.4	1980 ± 150	4
GL229b	>23.3	21.2	18.26	174.9 ± 4.5	1200 ± >150	7
GD165b	>20.3	17.2	14.83	27.8 ± 3.4	1780 ± 106	4,5,8
PC0025+0441	–	15.26	13.79	14.0 ± 4.0	2010 ± 200	4
PPL 15	–	12.26	11.96	$(m - M = 5.53 \pm 0.05)$	2800 ± 150	8
Teide 1	16.05	13.31	0.0	$(m - M = 5.53 \pm 0.05)$	2350 ± 150	6

Table 3.2: Stars used to define bolometric corrections and temperature relationships. Temperatures are mean values where more than source is available. The uncertainty in M_{bol} is assumed to be 10% unless stated. References: [1] Veeder, 1974, [2] Berriman *et al.* , 1992, [3] Bessell and Stringfellow, 1993, [4] Reid *et al.* , 1994, [5] Jones *et al.* , 1996, [6] Rebolo *et al.* , 1995, [7] Nakajima *et al.* , 1995, [8] Kirkpatrick *et al.* , 1993, [9] Leggett, 1992. Stars below the horizontal line are included for comparative purposes and are not used in defining the BC (note lower limits to M_R in first two).

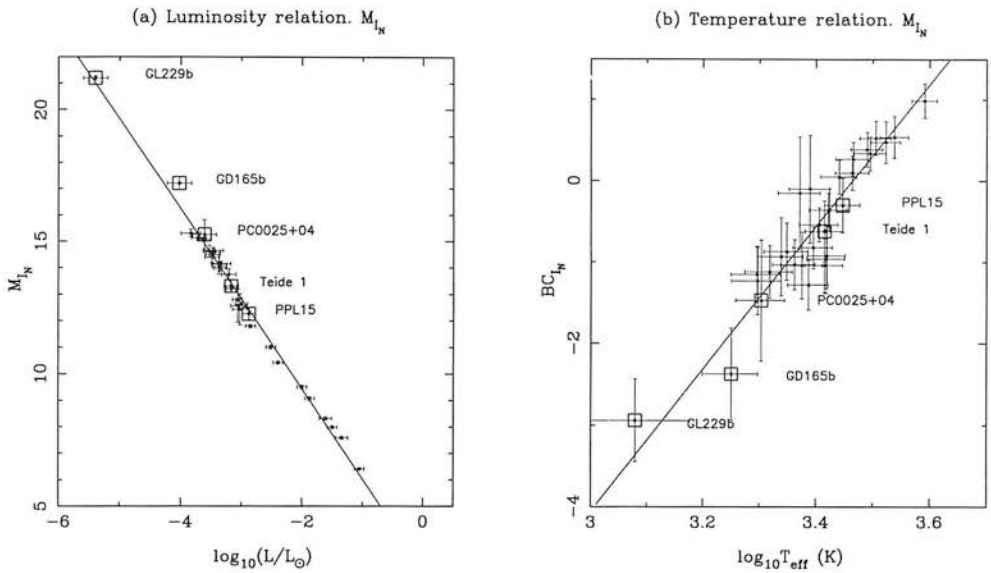

Figure 3.2: Bolometric corrections to the I_N waveband, derived from the measurements given in table 3.2

$\psi_0(M, t = 0)$ of each successive epoch of star formation from the formation of the Galactic disc (t_i) to the present (t_f):

$$\frac{dN}{dL} = \phi(L,t) = \int_{t_i}^{t_f} \beta(t)\psi_0(M) \left(\frac{dM}{dL}\right)_t dt. \tag{3.8}$$

Equation 3.8 includes the function $\beta(t)$ which is the stellar birthrate. The birthrate represents variations in the star-formation process over the history of the disc which may be due to physical effects such as the gradual depletion of molecular gas which is time-dependent and the enrichment of the inter-stellar medium which may affect the mass distribution. The star-forming history of the disc remains a mystery since the products of all but the most recent events have relaxed into the general field and are all but untraceable. Evidence of previous bursts could be gleaned from variations in the kinematic distribution of various stellar groups. For example, Gómez *et al.* (1990) present such measurements which they suggest point to three

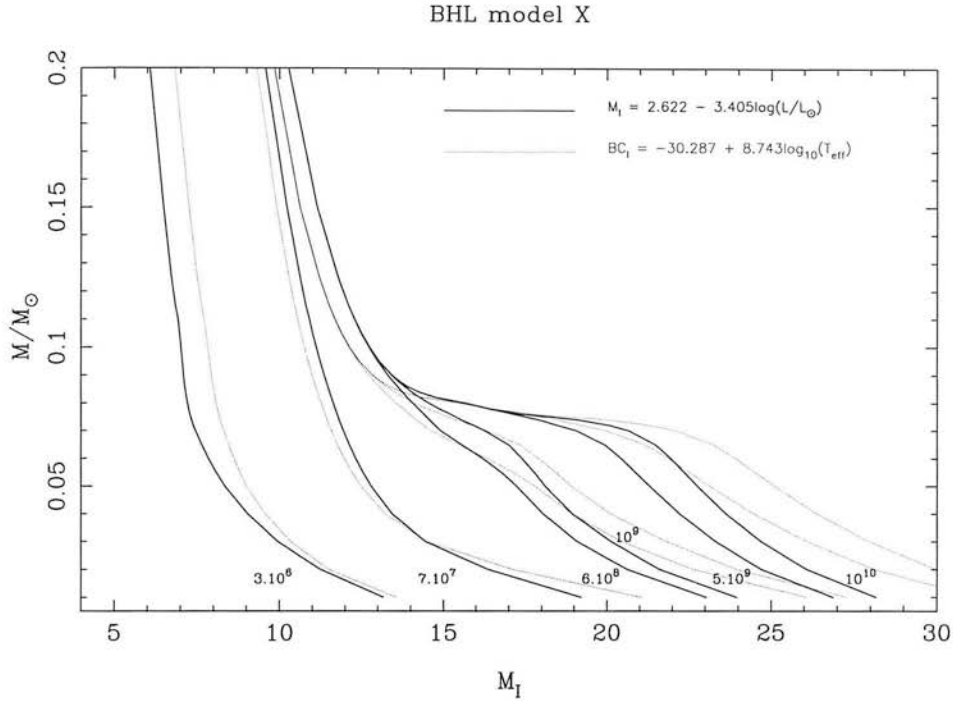

Figure 3.3: Comparison of absolute magnitude-mass relationships for six isochrones of the BHSL93 model based on the bolometric corrections discussed in the text.

events during the past 10^9 years. Such data are sketchy and not yet compelling.

Miller & Scalo (1979) and Scalo (1986) have reviewed work in this field and conclude that the current picture is consistent with a roughly constant rate of star formation over the ten billion years or so of the disc's history. A time-independent birthrate can be scaled to the number density of low mass dwarf stars (later than spectral class K) which have main sequence lifetimes comparable to the 'Hubble' age of the Universe, i.e. 10^{10} years. These stars will not have evolved significantly in luminosity and represent the cumulative result of the star forming history of the disc. For a constant birthrate then, dividing the integrated number density by an estimated Galactic disc age yields β. The general condition for β is

$$\int_{t_i}^{t_f} \beta(t)dt = 1, \tag{3.9}$$

which reduces to $\beta(t) = \overline{\beta} = \frac{1}{t_f - ti}$, i.e. the reciprocal of the age of the Galactic disc, T_{gal}.

The final step is to normalise the mass function to some likely value. For this example, the most interesting case is that in which a brown dwarf population accounts for any local dark matter, as discussed in §2.8. The scaling then involves taking a possible value for the missing mass density, ρ_{mm} and setting this equal to the integrated mass of the brown dwarf region of the low mass star MF:

$$N \int_{0.01M_{\odot}}^{0.085M_{\odot}} M^{1+\alpha} dM = \rho_{mm} \quad M_{\odot} pc^{-3}. \tag{3.10}$$

The parameters chosen here to fully determine equation 3.8 are: $T_{gal} = 1 \times 10^{10}$ years, implying $\beta = 1 \times 10^{-10} yr^{-1}$ and $\rho_{mm} = 0.1 M_{\odot} pc^{-3}$ for upper and lower mass limits of $0.01M_{\odot}$ and $0.085M_{\odot}$. The upper limit is reasonably well established as a suitable red/brown dwarf boundary but the lower limit is somewhat arbitrary and is chosen to coincide with the published limit of the BHLS93 model. The BHLS93 model suggests a lower limit to the stellar main sequence of $0.078M_{\odot}$, lower than the earlier Burrows *et al.* (1989) models and those of Nelson *et al.* 1993 (NRJ93). In this case, $0.085M_{\odot}$ is chosen for comparison to the NRJ93 work and to act as an upper limit on the number of detectable brown dwarfs and transitional objects, though the published BHLS93 value is adopted later.

The resulting luminosity functions, generated with the $M_I - \log(L)$ relation are shown in figure 3.4. The distribution for all objects in the range $10 < M_I < 30$ is shown along with the contribution for objects below $0.085M_{\odot}$. This gives some indication of how much the M dwarf population is 'contaminated' with brown dwarfs. Comparing the features to previous work, the functions generated by NRJ93 are the closest in style. They show the contribution of populations below various temperature limits, the highest being 3000K. The temperature cut-off for the LFs presented here is roughly 2700K. Comparing the x-intercepts: $M_I \simeq 10$ for a 2700K population in the Nelson *et al.* LF and $M_I \simeq 11$ for this work. The normalisation used is the same and the overall shape and scale of the functions are similar.

The saw-tooth variation of the fainter bins of Salpeter-based LF appears to be due the level of digitisation of the BHSL93 model. Although interpolated onto

various grids ranging from 2 to 20 Myr the steepness of the mass function and mass-luminosity-time relation leads to unreliable results in the regions where the relationships are varying most rapidly. Coarser interpolation reduces this effect but also masks the important variations in the brown dwarf population during the first few hundred million years. It should be noted that the youngest BHLS93 models are for 3 Myr objects, representing T Tauri stars in earliest visible stage of stellar evolution. Stellar modellers are unanimous in their warnings regarding the uncertainty in the models of these youngest objects due to the as yet un-modelled and poorly understood processes of pre-main sequence evolution. The predictions given in this section are based on models of objects older than 10 Myr to alleviate some of this uncertainty.

Armed with a luminosity function, a study of the observable surface distribution for a given set of survey conditions (detector, field of view, Galactic latitude) can be predicted.

3.3.3 Surface distribution

To calculate the surface distribution as a function of apparent magnitude $S(m_\lambda)$, the luminosity function must be integrated through space according to some density function $\rho(x, y, z)$ i.e.

$$S(m_\lambda) = \Omega \int_0^\infty \phi(M_\lambda)\rho(x, y, z)r^2 dr. \tag{3.11}$$

$S(m_\lambda)$ gives the number of objects projected on the celestial sphere in solid angle Ω per unit apparent magnitude of waveband λ, where the luminosity function is expressed in the absolute magnitude of the same waveband and r represents radial distance from the observer.

A barometric density function of the form given in equation 3.1 is usually used for $\rho(x, y, z)$. This simplifies matters by assuming uniformity in the (x,y)-plane of the Galactic disc and symmetry about the perpendicular z-axis. The z-distribution is

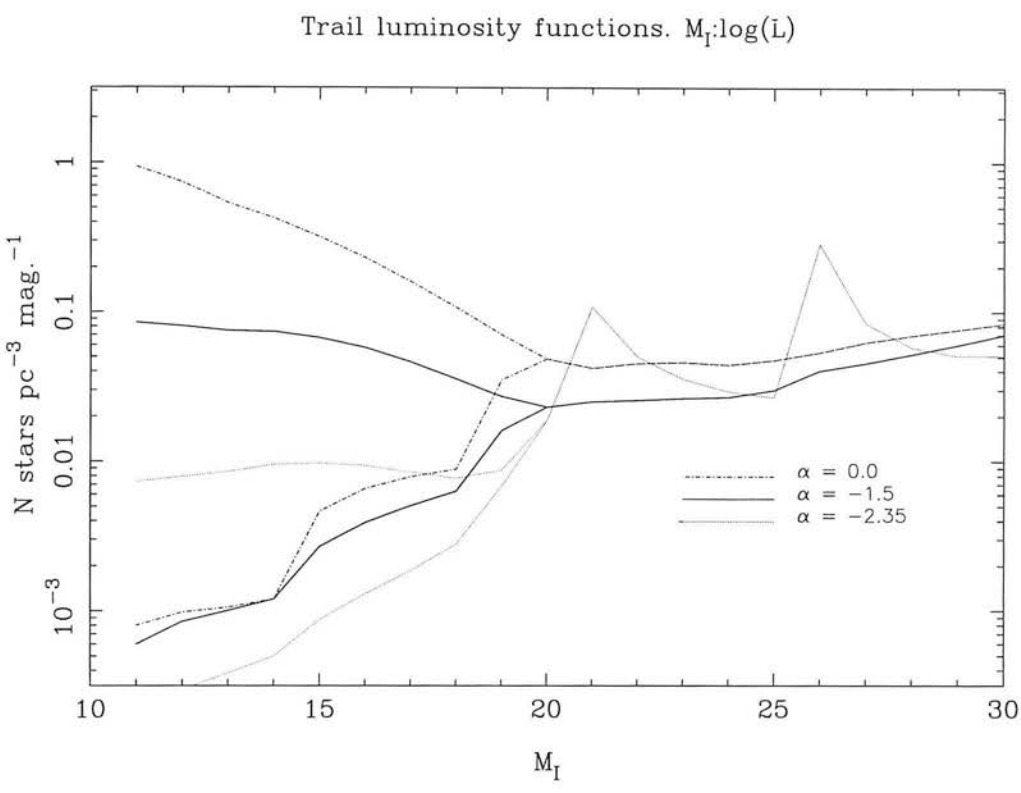

Figure 3.4: Simulated luminosity functions for three power law mass functions with all objects and brown dwarf contributions shown for each.

generally assumed to be centred both in the Galactic mid-plane and the observer (the Solar system) implying that the Sun lies at z=0. For a field at Galactic latitude b and a density function characterised by a scale height H_z, the surface distribution becomes

$$S(m_\lambda) = \Omega \int_0^\infty \phi(M_\lambda) e^{\frac{-r \sin b}{H_z}} r^2 dr. \tag{3.12}$$

By computing $S(m)$ for the stellar and sub-stellar populations under the conditions of a photographic survey some idea of the relative numbers of the two populations at a given magnitude can be gleaned. This method can be extended to other functions such as temperature, photometric colour or spectral type. Figure 3.5 shows the computed I band surface distributions at two Galactic latitudes (-45° and -90°) for each of the mass functions discussed and the R band distribution

at -45° for the two bolometric corrections available (equations 3.7 and 3.6). The bolometric correction for $S(I)$ is given by equation 3.5 and a density distribution of scale height 350pc is used. The MF normalisation and birthrate are as discussed above. In each case the thicker line shows the distribution for all objects within the mass range under consideration (0.01 to $0.2M_{\odot}$) and the thinner line shows the contribution from the brown dwarf population alone (defined as being objects less massive than $0.085M_{\odot}$).

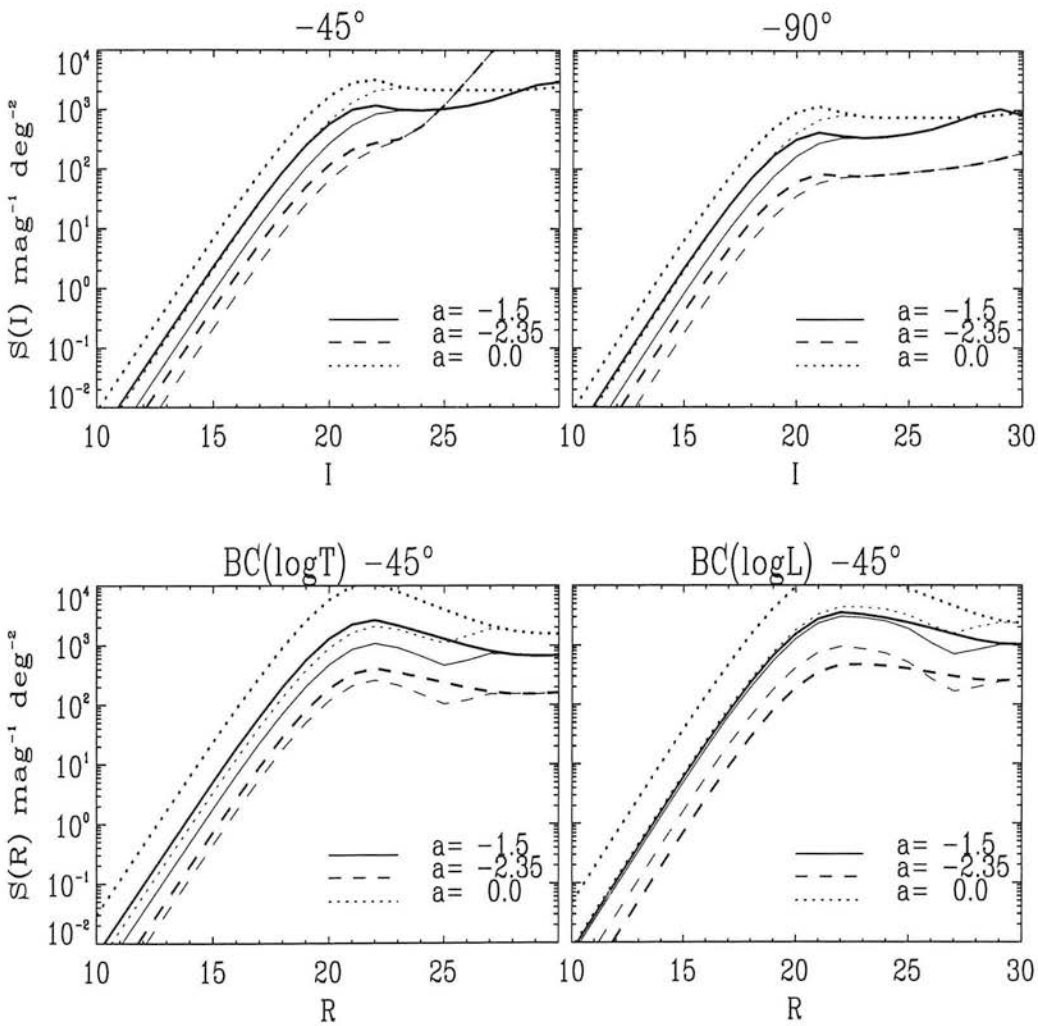

Figure 3.5: R_F and I-band surface distributions for three power-law mass functions.

The distributions confirm several expectations. Firstly, the number counts fall towards the Galactic poles. In this case, between a mid-latitude and polar field, by a factor of approximately five for the fainter objects in the flat region of the distribution. For the brightest bins, the curves are linear with gradient 0.6 (for

log N), due to the fact that for the nearest objects the density functions are essentially constant and the surface distribution reduces to $S(m) \propto 10^{0.6m+const.}$ for a given absolute M. Note that these distributions concern objects in the mass range of the BHSL93 model only. According to the most recent work on calibrating the mass/spectral type relationship (Baraffe and Chabrier 1996) this mass range represents dwarfs of type equal to or later than type M4.

The apparent magnitude limit of an I-band UK Schmidt survey plate is around 19 which means that the interesting region of these distributions for photographic work is this mostly linear region. The magnitude limit at which the plates are *complete* in terms of the detection of all real objects in the field is higher than this value by one to two magnitudes. For this reason a limit of I = 18 is used here, with the caveat that detections in the I = 17 to 18 range may be incomplete on all but the deepest UKST I plates. Note the sharp up-turn in counts for the Salpeter mass function in the $b = -45°$ case, a consequence of the previously noted saw-tooth nature of the corresponding LF acting on a large number of objects. For the range of mass functions considered here, the integrated number density over the I = 10 to 18 range varies from around 120 ($\alpha = 0.0$) to 8 ($\alpha = -2.35$) for the $b = -45°$ case. The numbers are slightly (15%) lower for the $b = -90°$ case when the whole distribution is considered, but the integrated number of brown dwarfs *remains much the same.* This is due to the effect of the density fall-off acting on the more luminous objects (M dwarfs) but not on the less luminous brown dwarfs which are sampled to smaller distances.

Thus, although the number counts decrease towards the pole, the expected *fraction* of brown dwarfs increases. The fractional increase grows with decreasing α and varies from 0.3 to 0.5 in the cases considered here (with the vast majority occupying the I = 17 - 18 bin [1]. This may be a consideration in surveys that can only expect to detect bright young BDs in the observationally ambiguous stages (in terms of photometric colour and broad-band spectroscopy) of their evolution. In comparison the variation between the two bolometric relations available (equations

[1]The bins are actually centred on integer values $\pm 0^m.5$

3.5 and 3.4) are negligible. The variation between the R band BCs is larger and it seems clear from the figure that extrapolation of the log L relation in particular gives very unreliable results. This is an inevitable consequence of the weaker R-band flux leading to poorer measurements and of the large colour terms between R band filters adding further uncertainty to the inter-comparison of red objects.

Some idea of the model-dependency of these distributions can be found by comparison with the NRJ93 distributions. They publish results for the polar case (though other distributions are easily generated by re-scaling as discussed in their paper). The curves agree to within less than a factor of ten, even at the extreme faint end (I = 30). For the brighter bins, the curves are in closer agreement. NRJ93 apply an upper temperature limit (T_{max}) to measure relative number counts (as opposed to the equally model-dependent mass limit used in this work). Their $T_{max} = 3000K$ is the closest case to BHLS93 model range used here and the Salpeter mass function considered here shows the closest agreement to their 'standard model' result. So the variation between these models, accepting the different initial conditions, is comparable to the variation between mass functions.

As noted by NRJ93 the surface distribution is sensitive to the normalisation of the mass function. The important factor is the missing mass density. To test this, the $\alpha = -1.5$ mass function was normalised in the mass range $0.01 - 0.09 M_{\odot}$ to three values of ρ_{mm}: 0.05, 0.1 (the default) and 0.2 $M_{\odot} pc^{-3}$ for $b = -45°$. Figure 3.6 presents the generated functions which show a large variation in actual number counts. Note the contribution from all objects (thick lines) and brown dwarfs (thinner line) for each case. The integrated numbers over the I = 10 to 18 range are just scaled by the fractional ρ_{mm} assumed and the brown dwarf density remains a reasonably constant 1/3. The integrated BD counts over the ρ_{mm} range are similar to those obtained over the range of α discussed above. For example, the $(\rho_{mm} = 0.2, \alpha = -1.5)$ case gives counts that are close to the $(\rho_{mm} = 0.1, \alpha = -2.35)$ case, and varying the mass function produces a wider range of number counts that scale accordingly. So due to the very low mass of the objects under consideration, modest variations in the missing mass density result

in large variations ($> 100\%$) in the uncertainty in number counts for a given mass function. and increased uncertainty between mass functions.

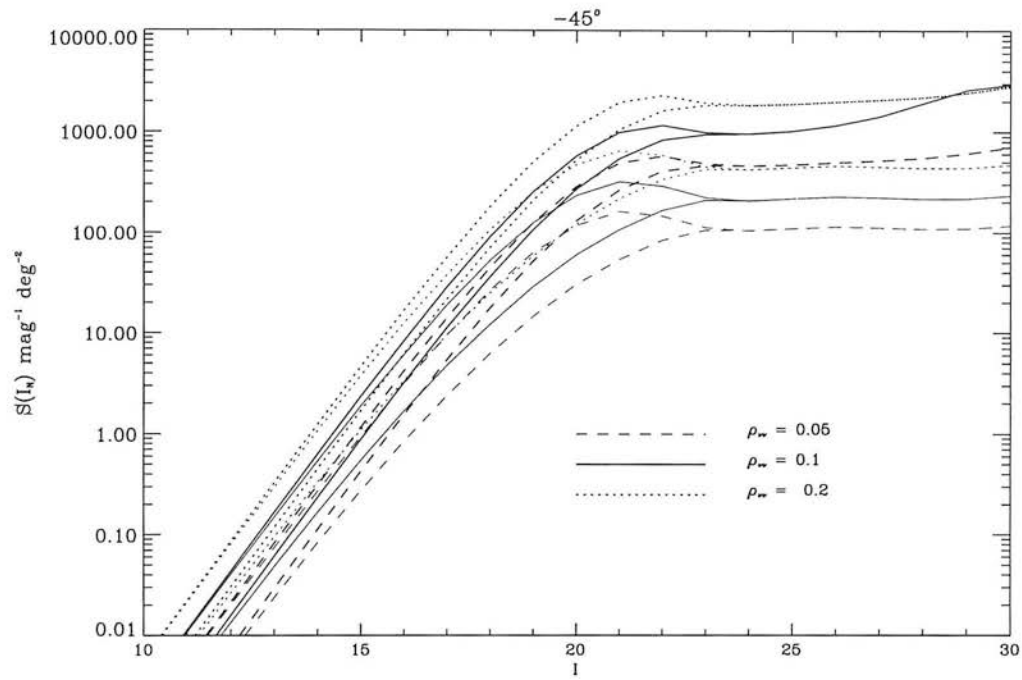

Figure 3.6: Surface distributions for three mass function normalised in the mass range $0.01 - 0.09 M_{\odot}$ to the quoted mass density for an assumed dark matter component of the Galactic disc; $\rho_{mm}(M_{\odot} pc^{-3})$.

It is worth reviewing figure 3.1 which essentially plots $S(m)$ for a single bin for various b_{gal}. The choice of scale height is clearly important and its effect is now considered. Implicit in equation 3.11 is an assumption of time-independence which reduces H_z to a constant. However it is commonly known that H_z varies with M_{λ}. Although the precise reason in unknown, a mechanism suggested by Spitzer and Schwarzchild (1951,1953) fits the observed variations. The model requires the presence of large ($10^5 M_{\odot}$) clumps of matter in the Galactic disc to interact with the stars and evidence for such bodies occurring commonly is weak. More recently Wielen (1977) proposed a mechanism based upon the diffusion of stellar orbits which describes the observed trend in velocity dispersion with time and relates it to other orbital parameters.

These models have a population of stars born close to the Galactic plane with a 'thermal' velocity dispersion that is small compared to the overall disc system. The cumulative effect of random interactions with mass clumps is to increase the group's velocity dispersion. The z-dispersion is predicted to be largely independent of the x,y motions and the three components do not increase equally with time. During this time the thermal motion of the stars acts to scatter them above and below the plane with mean distance increasing with the age of the group. For a coeval stellar group described by a Maxwell-Boltzmann distribution as discussed in §2.8 a scale height can be associated with the velocity dispersion and thus the age of the group, i.e $H_z \propto \sigma_{v_z}^2$, scaled by the z-component of the disc's gravitational potential.

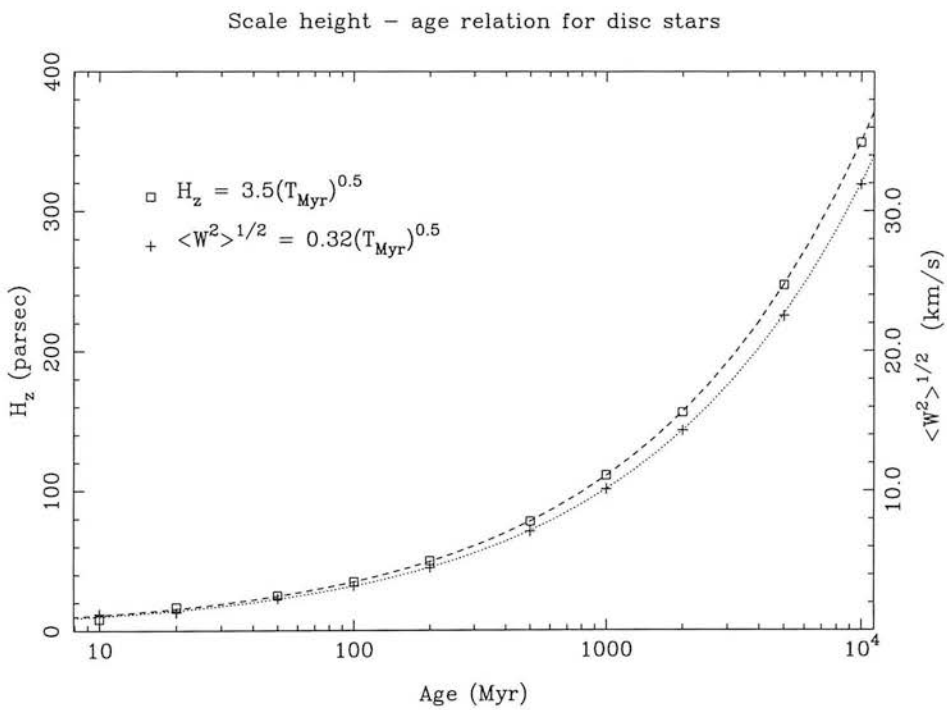

Figure 3.7: The predicted change of vertical scale height and velocity dispersion with time, based on data from Wielen (1977).

Figure 3.7 shows the trends in scale-height and W-component velocity dispersion as determined by Wielen for a constant diffusion coefficient (which gives the best empirical fit, of those tried by Wielen). The lines through the points are

relationships determined for the surface distribution study of this section. The chosen $H_z(t)$ relationship is quoted below, where t_6 is the age of the population in megayears (a relationship for σ_W is given in the following section). Note the similarity in shape of the curves, but difference in scale, as expected.

$$H_z(t) = 3.5(t_6)^{0.5} \tag{3.13}$$

Since a significant fraction of sub-stellar objects in the $M_I < 14$ range will be younger than 1 Gyr this time-dependence will affect the observable fraction of brown dwarfs. The largest uncertainty in using this form of $H_z(t)$ comes from the assumption that the populations move smoothly from one isothermal distribution to the next throughout their evolution. For the oldest stars this appears to be reasonable but for the youngest objects, most tightly coupled to the star-forming regions of the mid-plane the group dispersion is likely to represent the local conditions during formation. It may take several hundred million years before the younger groups have relaxed into the overall Galactic potential. Wielen notes that the predicted trend of $\Delta z(t)$ is more accurate for young stars whereas the trend in ΔW becomes more uncertain with time. With this in mind, it worth comparing the standard approach to the time-dependent one and suggesting that even if the distribution of the youngest objects is not well represented by $H_z(t)$, it likely to be even less well represented by $H_z = constant$ and that the Wielen model gives a 'first order' improvement.

The surface density distribution now becomes

$$S(m_\lambda, t) = A \int_0^\infty \phi(M_\lambda, t) e^{-\frac{r \sin b}{Hz(t)}} r^2 dr, \tag{3.14}$$

and

$$S(m_\lambda) = \int_{t_i}^{t_f} S(m_\lambda, t) dt. \tag{3.15}$$

The effect of a time-dependent scale height is plotted in figure 3.8, in which the stellar (solid line) and sub-stellar (dashed line) contributions are shown for both

density distributions. Plot (a) shows the absolute difference in number counts between the constant and time-dependent cases. The counts have been scaled by 25, to represent the variation over an area of 25 square degrees: the COSMOS - measured area of a Schmidt plate. The difference over this scale is unmeasurable for I < 18, which is roughly the completeness limit of a IV-N I-band survey plate. Beyond this, the use of a constant scale height appears to greatly over-estimate the numbers with respect to the time-dependent case. Plot (b) shows the fractional contribution of brown dwarfs to the distribution for both cases, which sheds some light on the variation below I = 18. The time-dependent case suggests a smaller fraction of sub-stellar objects which is most significant in the I = 18 to 21 range: within the range of CCD surveys. In these examples, $\phi(M_I)$ is based upon an $\alpha = -1.5$ mass function normalised over the previously discussed range and generated with BC given by equation 3.5.

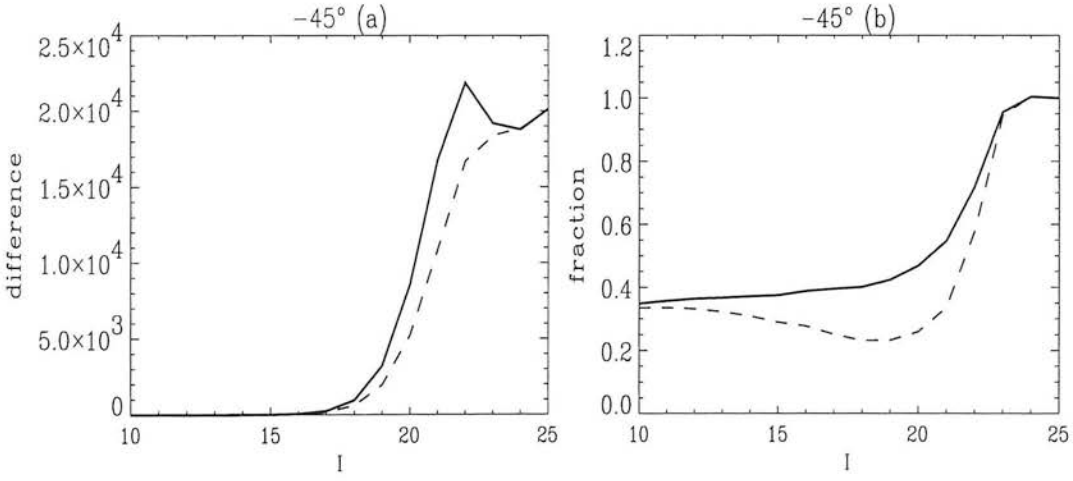

Figure 3.8: A comparison of the expected number counts for constant (solid line) and time-dependent (dashed line) density functions. figure (a) compares absolute numbers and (b) shows the fractional variation, both for the same 25 deg^2 field

Implicit in all of the preceeding distributions is the assumption that the observer (the Earth or Solar System) lies at the mid-Galactic plane in the centre of the

$\rho(z)$ distribution. Numerous studies recently have suggested that the Sun lies several tens of parsecs above the plane: The low mass star luminosity function of Kirkpatrick *et al.* 1994 derives a north/south Galactic number density fraction that implies $Z_\odot \simeq 41$pc. Stobie & Ishida (1987) also use north/south (polar) stars counts to infer $Z_\odot \simeq 42$pc. Van der Kruit (1989) measures 12pc from deep space Galaxy surface brightness measurements and numerous authors (Brand & Blitz, 1993, Combes 1991 and references therein) have used the distribution of molecular clouds and CO to infer values in the range 20 ± 20pc. The collective strength of these arguments lies in the variety of different techniques that have independently suggested a value in the range $0 < z_\odot < 40$ (parsecs). These values are small compared to the scale of the old disc star distribution ($H_z \simeq 350pc$) but are a considerable fraction of the scale height for younger stars. To examine the likely variation in surface distribution for $z_\odot > 0$, the density function is modified to

$$\rho/\rho_0 = e^{-|z_*|/H_z}, \tag{3.16}$$

where $z_* = z_\odot + r \sin b$.

The result of this change is determined for both the constant and time-dependent scale height cases. Figure 3.9 shows the result, by directly comparing the $S(I)$ distributions. Two groups of curves are apparent, the solid lines (thick: all objects, thin: brown dwarfs only) represent the basic 'constant scale height, $z_\odot = 0$' case. The dashed lines show the affect of assuming $z_\odot = 50$pc with a constant scale height of 350pc: a minor increase in numbers, as expected for a density function that is varying on a much larger scale than the $z_\odot$ variation. The dot-dashed lines show the $z_\odot = 0$ distribution for the time-dependent scale height, with the dotted curves showing the equivalent $z_\odot = 50$pc case. Here, the relative increase in numbers is more pronounced, particularly in the I < 18 region. Over this range, which is accessible to Schmidt survey plates, the integrated (brown dwarf) counts for the time-dependent case increase by around 50% from 7 to 11. Compare this to the time-independent case, where the absolute numbers are larger but the fractional change is smaller: 20% from 15 to 18. Note that the $z_\odot = 50$pc

distributions, in both cases predict *less* objects in the range I=10 to 13 and then more beyond this. This is due to the fact that observer is not lying in the densest part of the distribution and because the survey beam is pointing south through the Galactic plane where the density increases, before falling-off again for negative z.

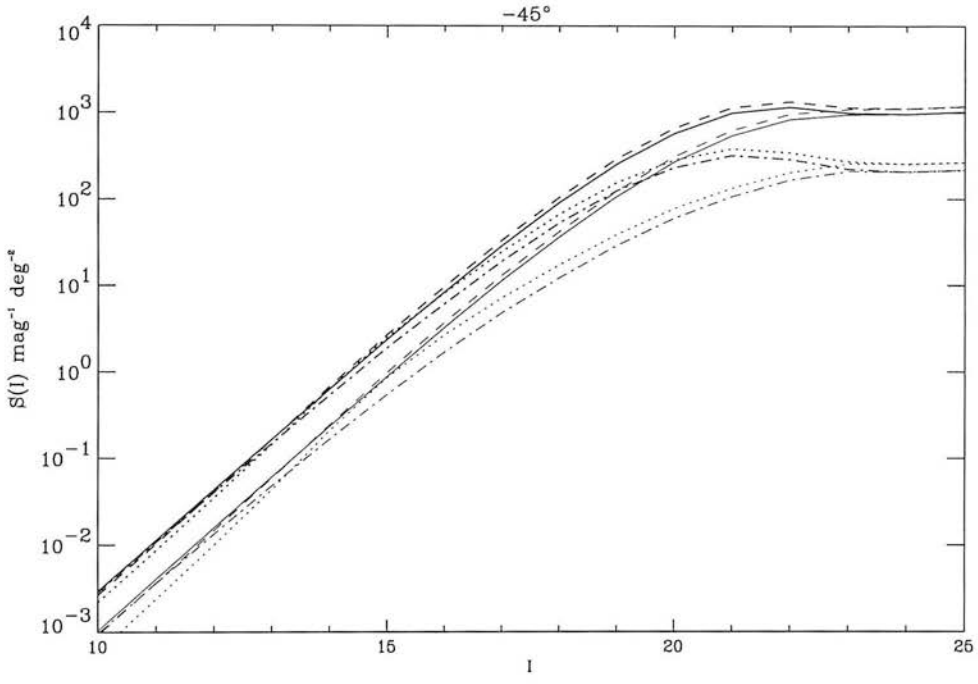

Figure 3.9: A comparison of the expected number counts for constant (solid line) and time-dependent (dot-dashed line) density functions at $z_\odot = 0$ and the corresponding cases: constant H_z (dashed line) and time-dep. $H_z(t)$ (dotted line) for $z_\odot = 50$pc

To summarise this section, the integrated number of brown dwarfs within the flux limit of an I-band survey plate is around five to twenty per square degree for the favoured mass function in a mid-latitude field. Of the variables considered here, this estimate is most sensitive to the mass function parameters, particularly the normalisation, which scales directly with the number density. The assumption of a time-dependent density function reduces the expected counts by a factor of 0.5, and the variation due to raising the Sun's position above the plane by 50pc acts

to oppose this loss, by doubling the numbers to within 60% of the standard case (i.e. to about 10 deg^{-2}). In terms of age, the brown dwarf distribution in the I < 18 range is almost exclusively made-up of objects less than 1 Gyr in age: 95% by number, of which >60% are younger than 0.5 Gyr and most are *fainter* than I=17. This has the important implication that any detected brown dwarfs will almost certainly mimic the properties of dM stars and thus some kind of follow-up programme is required to discriminate between the populations.

The fractional contribution of brown dwarfs to the distribution of stars with masses less than $0.2M_{\odot}$, corresponding approximately to type dM4 and later, is around 0.35, though this falls to around 0.2 for objects near the plate limit in the time-dependent density case. To quantify this further, the figure 3.10 shows the expected fraction of brown dwarfs within each spectral sub-class, and the relative numbers between them. This was produced by generating the surface distributions for stars within a given range of temperatures which have been chosen to roughly represent the range of dM sub-classes. The counts are for the constant scale-height case, refer to figure 3.8 to scale the relative counts for the time-dependent case and figure 3.9 to scale the absolute numbers. Table 3.3 gives the adopted effective temperature range for each sub-class, which are each about 150 to 200 K wide; the size of typical quoted uncertainties. The basis of this scale are the references given in table 3.2.

Spectral class	M4	M5	M6	M7	M8	M9	M10
$T_{eff}(K)$	3250–3050	3050–2900	2900–2700	2700–2550	2550–2300	2300–2050	2050–1800

Table 3.3: Approximate temperature range for dM spectral sub-classes.

The are two striking features about figure 3.10, The paucity of objects of class dM4 and of hydrogen-burning stars beyond dM7. The first feature is fictitious and due to the fact that the stellar model used does not extend, in terms of T_{eff} to the upper limit of the dM4 range and so this bin is unreliable. The dearth of M dwarfs beyond M7 is again model-dependent. As discussed in Chapter 2, differences in model

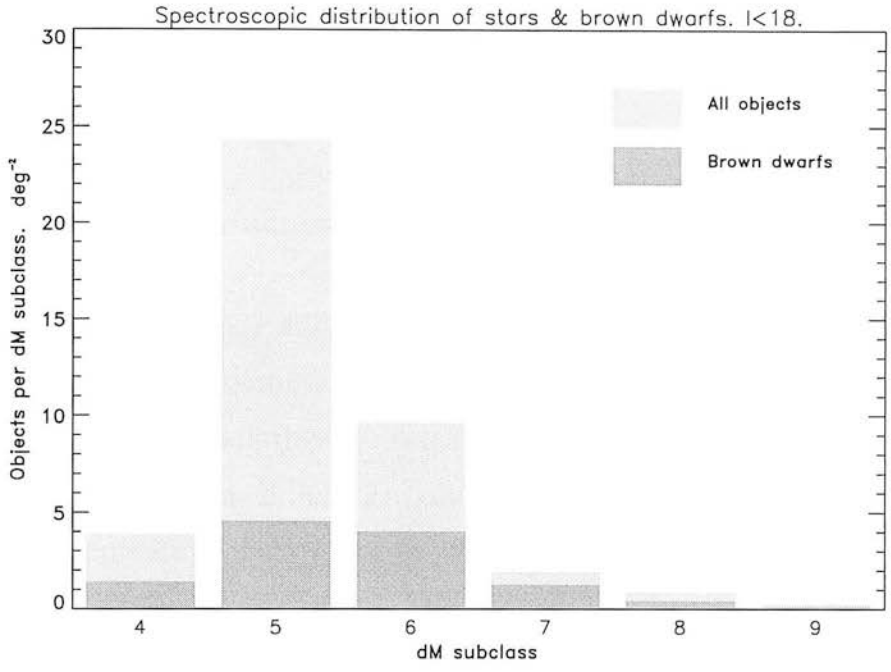

Figure 3.10: The relative number of brown dwarfs and hydrogen-burning stars per spectral sub-class per square degree for I< 18.

atmospheres lead to systematic shifts of 100 to 200K in effective temperature. If this figure were plotted with the Nelson *et al.* (1993) models the counts would be shifted late-wards by about 1 sub-class. For the D'antona & Mazzitelli (1994) model, the shift late-ward is one to two sub-classes. The choice of stellar/brown dwarf mass limit, the HBMM is also important. Here, a value of $0.078M_{\odot}$ has been used as discussed earlier. Again, this is model dependent, with the NRJ93 model predicting a higher HBMM and therefore *fewer* stars in later bins. The mot recent Baraffe and Chabrier (1996) model estimates HBMM $\simeq 0.07M_{\odot}$, the use of which would lead to predictions of more stars of later type and correspondingly less brown dwarfs.

In the light of this uncertainty figure 3.10 should not be taken too literally. What it does tell us is that for I-band Schmidt-plates *the observable distribution of brown dwarfs is likely to peak around M6* and then fall-off. Brown dwarfs of later type are of course much more numerous than the young M6 objects, but they will

not be detected in any significant numbers below I=18, whereas the number of hydrogen-burning M dwarfs really does fall off to zero beyond about dM6, as previous luminosity functions have shown.

3.3.4 Observable kinematic distribution

In this section, the likely distribution of proper motions for very low mass stars is considered. The assumptions made in the previous section about the space distribution of the population are combined with a simple kinematic model. The intention is to determine if there are any measurable properties that may be useful for the discrimination of stars and brown dwarfs.

The basic model requires a distribution of velocities. In Galactic co-ordinates stellar velocities are resolved in to U, V and W components. The axes are oriented toward the Galactic centre (U), the local direction of rotation about the Galactic centre (V) and the north Galactic pole (W). The distribution about each axis is assumed to be (independently) random with Gaussian dispersion, implying an ellipsoidal velocity distribution. This model has been shown be reasonably realistic (Mihalas & Binney p. 418), particularly for the W component, which does seem to be strongly independent of U and V. As discussed in the previous section, the velocity dispersions of a stellar population appear to increase with age. A functional form for the growth of σ_W was shown in figure 3.7 and equations for each component, derived from Wielen's data are given below. In each case, the age of the population t_6 is supplied in megayears. These fits are based on Wielen's constant dispersion coefficient case, and the curves are just scaled by the dispersion at 10 Gyr. The dispersions for the 'time independent' case vary with the population that is used to define them. Wielen determines the values for the K and M dwarf sub-set of the Gliese catalogue at a mid-plane value ($\sigma_U : \sigma_V : \sigma_W = 39 : 23 : 20$) and the average integrated over z (48 : 29 : 25), this latter set are adopted here (all velocities are given in km/s).

$$\sigma_U(t) = 0.60(t_6)^{0.5} \tag{3.17}$$

$$\sigma_V(t) = 0.38(t_6)^{0.5} \tag{3.18}$$

$$\sigma_W(t) = 0.32(t_6)^{0.5} \tag{3.19}$$

The vertex of the largest component of the UVW distribution is oriented toward a direction that is called the *longitude of the vertex* and is found to be $\ell_v \simeq 0°$ for 'mature' populations. The correction to the projected UVW components for deviation from this vertex direction is given by Mihalas & Binney (p. 421):

$$U = U_1 \cos \ell_v + V_1 \sin \ell_v \tag{3.20}$$

$$V = -U_1 \sin \ell_v + V_1 \cos \ell_v \tag{3.21}$$

$$W = W_1 \tag{3.22}$$

There is an observed trend of increasing *vertex deviation* with younger populations (more exactly, populations of earlier spectral type). Again Wielen's study explores this and a time-dependent vertex deviation function can be extracted from it. Equation 3.23 gives a cubic fit up to 250 Myr (t_6 is age in Myr) with a linear extrapolation to $\ell_v = 0°$ at 500 Myr. The predictions and fit are shown in figure 3.11 which shows the increasingly positive deviation for younger distributions. Real variations are negative as well as positive but there is no model as yet which can describe this.

$$\ell_v = 91.2 - 0.79(t_6) + 0.0024(T_6)^2 - 2.37 \times 10^{-6}(T_6)^3. \tag{3.23}$$

To derive proper motions from this, the velocities can be corrected for the solar motion with respect to the local standard of rest, which is directed towards ($\ell = 53,° \; b = 25°$) with components $U_\odot = -9, V_\odot = 12, W_\odot = 7$ in km/s (Mihalas

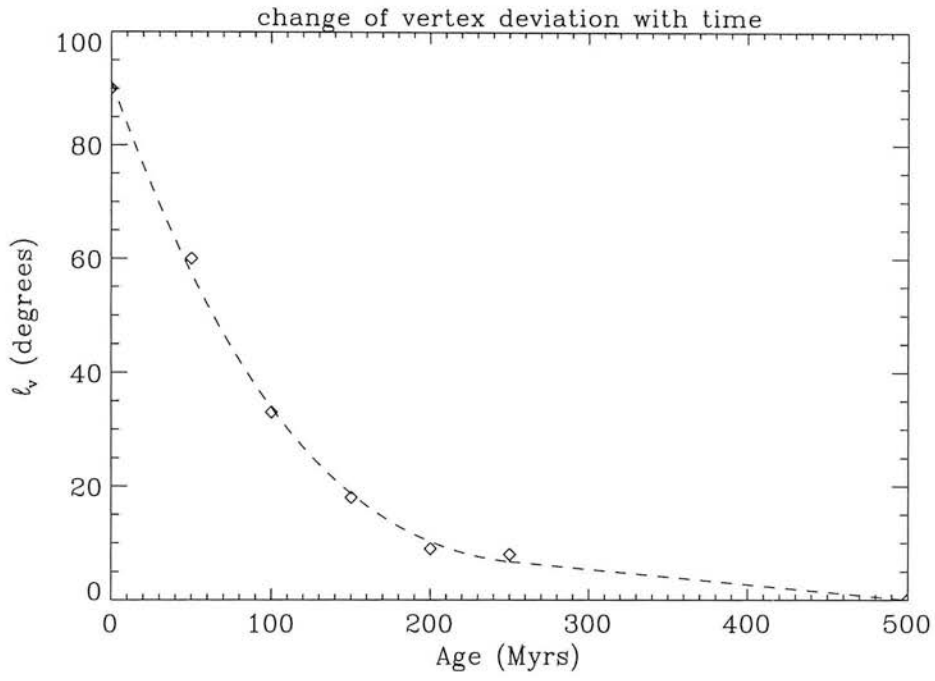

Figure 3.11: The relationship between longitude of vertex and age, for young stellar populations. Based on calculations by Wielen (1977).

& Binney p. 399). Transforming from the Galactic (UVW) to the rectangular equatorial frame (heliocentric $\dot{x}, \dot{y}, \dot{z}$) and applying the following transformation[2] yields the required proper motions
(and radial velocity).

$$\dot{x}\cos\delta\cos\alpha + \dot{y}\cos\delta\sin\alpha + \dot{z}\sin\delta = V_r \tag{3.24}$$

$$-\dot{x}\sin\delta\cos\alpha - \dot{y}\sin\delta\sin\alpha + \dot{z}\cos\delta = d\mu_\delta \tag{3.25}$$

$$-\dot{x}\sin\alpha + \dot{y}\cos\alpha = d\mu_\alpha\cos\delta \tag{3.26}$$

Here, α, δ are the celestial co-ordinates of the object, $\mu_\alpha, \mu_\delta\cos\delta$ the corresponding proper motion components and d is the distance of the star from the Sun. The distribution is produced using a 'Monte Carlo' method, by randomly generating a distance according the density distributions defined earlier. UVW velocities

[2]see Trumpler & Weaver p. 244 for example

are similarly selected from their distributions and combined with absolute magnitudes and randomly-generated positions within a specified field. Three cases are considered:

(i) Constant scale height, mean velocity dispersion.

(ii) Time-dep. scale height, time-dependent velocity dispersion.

(iii) Time-dep. scale height, time-dep. velocity dispersion, vertex deviation

In each case, the favoured $\alpha = -1.5$ mass function, normalised to $\rho_{mm} = 0.1 M_{\odot} pc^{-3}$ over the range $0.01 - 0.09 M_{\odot}$ is used.

Figure 3.12 shows the predicted case (i) distribution of old (> 5 Gyr) disc dwarfs (upper plots) and brown dwarfs (lower plots) for two fields studied in this survey: $21^h, -45°$ ($b_{gal} = -41°$) and $1^h30, -40°$ ($b_{gal} = -74°$). The contours represent the number of objects per square degree on a linear scale, with the largest ring containing about 65% of the objects. The distributions show the expected stream toward the antapex of the Solar motion, with increasing μ_{α} and decreasing μ_{δ} with the brown dwarf distributions being further off-axis than the old disc group by approximately $0''.05$ yr^{-1}. There is no evidence of the BD contours being skewed with respect to the old disc.

Cases (ii) and (iii) for the brown dwarf population are given in figure 3.13 and show that a) the assumption of time-dependent velocity dispersion results in a considerable off-axis shift, acting to exaggerate the case (i) distributions and b) the additional assumption of time-varying vertex deviation does not add any further significant variation. The old disc distribution for cases (ii) and (iii) is not shown since both variables are significant only for young and intermediate aged-objects and so the prediction is unchanged. The contribution made by younger hydrogen-burning stars is more relevant though, and the contours of the combined brown dwarf and stellar distribution for objects younger than 2 Gyr are overplotted on the case (iii) figures as fainter, dashed lines. These distributions show

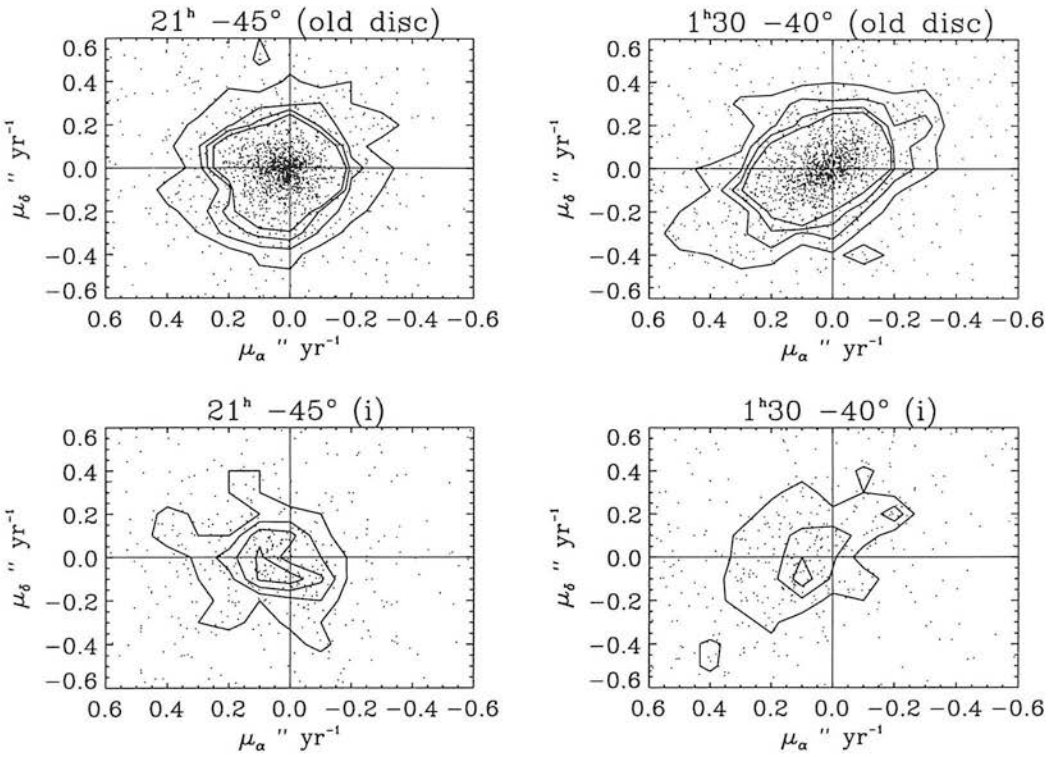

Figure 3.12: Predicted proper motion distributions for old disc dM stars and brown dwarfs in the same fields (case i).

a similar inclination but are not so far displaced from the origin. The difference in displacement is larger for the $1^h30, -40°$ field, as much as $0''.1$ yr^{-1} compared to approximately $0''.05$ yr^{-1} in the $21^h, -45°$ field. In order to use this information, sufficient objects must be detected to ensure good definition of the distributions. Since the populations are mixed, the measured effect is an overly-elongated distribution in the third quadrant. For the $1^h30, -40°$ field, at least 60 objects are needed in order to constitute the barest minimum over-density, which by optimistic estimates from the previous section may require between four and thirty square degrees; within the range of single survey field.

In summary, the majority of hydrogen-burning stars have proper motions of less than $0''.1$ yr^{-1}. Due to the relative nearness of any detected brown dwarf, the group will show a larger mean proper motion by up to $0''.1$ yr^{-1} which may allow them to be distinguished *en masse* from young disc stars which may otherwise be

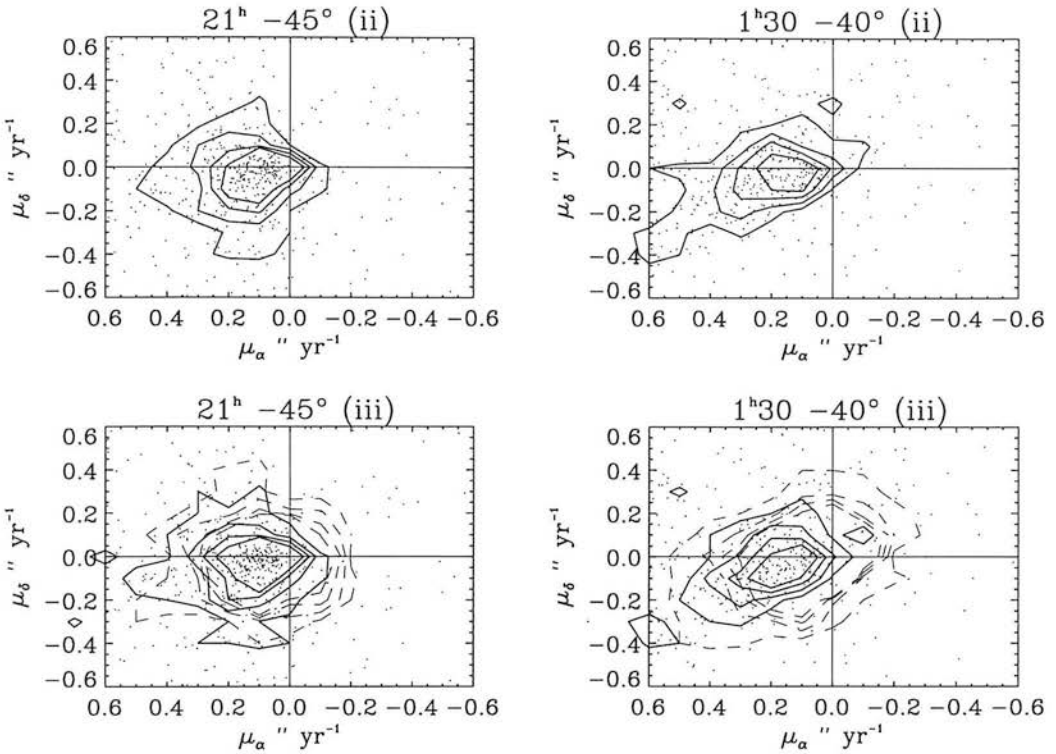

Figure 3.13: Predicted proper motion distributions for brown dwarfs (case ii: time-dependent velocity distribution, case iii: as case ii plus time-dep. vertex deviation).

indistinguishable.[3] Given the relative number of M-dwarfs and BDs in a sample (see previous section) and the extent of overlap of the M-dwarf proper motion distribution it is unlikely that the observed proper motions alone can be used to identify objects. Any objects with a motion in excess of $0''.1$ yr^{-1} will be of interest though and plate material can be selected with this in mind.

3.4 Requirements of the survey.

The basic philosophy behind the project method is to use red-sensitive photographic plates to detect brown dwarf stars in the field. The wide field of survey plates compensates for their poor 'quantum efficiency' (sensitivity to light). Previous photographic surveys of cool stars have selected objects with the V–I colour (Reid & Gilmore 1982, Stobie *et al.* 1989) and others have used R–I (Hawkins &

[3] As discussed previously, young brown dwarfs are predicted to follow a similar evolutionary path to pre-main sequence stars, giving them similar broad-band colours and spectra for the first 0.5 Gyr or so.

Bessell 1988, Leggett & Hawkins, 1988, Tinney *et al.* 1993). The areal coverage of these surveys has varied from a single field to 270 square degrees (ten fields) and the emphasis has been on selecting the reddest objects, which, as discussed above, is not necessarily equivalent to selecting the most likely brown dwarf candidates. In this survey, attention is given to those objects which show apparent youth in terms of over-luminosity for a given colour and distinctive proper motion. Extreme red objects are obviously not rejected as these are interesting in their own right, but hotter objects of class M5 or M6 are not necessarily rejected either.

The preceeding sections have suggested several constraints which should be considered in order to make the best use of the available material. The plate material for the programme has been chosen on the basis of waveband, plate quality and temporal baseline. R and I band plates are used for the photometric selection of near infrared objects and the construction of a luminosity function via a colour-luminosity relationship. As the bolometric relationships discussed in §2.5 suggest this is likely to be reliable for R–I < 2.0 and unreliable for R–I > 3.0. A third waveband, B_j has been included in order to provide 2-colour distributions which allow identification of the main sequence and possible contaminants and to act as a 'null result' in the detection of extremely red objects (*i.e.* objects with no B_J counterpart). The projected I-band number counts are very sensitive to the flux limit and so the best possible survey-grade plates are required to ensure a consistently deep plate limit. Assuming an I-plate limit of 18.0, and an upper-limit to the R–I index of approximately 3.0, An R-band plate limit of 21.0 is implied, which is a reasonable value for an A or B-grade plate.

More than one deep plate of each photometric band is required for each field in order remove spurious images from each plate by inter-comparison. Since the UKST R and I surveys are not yet complete, and are only required to have one 'a' grade plate per waveband, poorer quality 'b' grade plates must also be used to meet this requirement. Fields close to the Galactic plane are ruled-out due to the large number of images which crowd to the point of over-lapping. The UK Equatorial R survey replaces the deep R survey in this region, defined as $|b_{Gal}| > 20°$. This

survey uses short exposures and so is unsuitable for this project.

The measurement of proper motions requires plates to have been exposed at epochs that are suitably separated to provide a good measure of the image displacement. This temporal *baseline* determines the quality of the proper motion measurement; the longer, the better. To detect objects with total proper motions of $0''.1$ yr^{-1} as discussed, requires a baseline of at least two years since, as shown in the following chapter, the typical positional transform uncertainty is 2 to 3 microns ($0''.1 = 1.5\mu$m). It follows that a baseline in excess of four years is need to determine a $0''.05$ yr^{-1} displacement, though the use of centroiding to identify the different proper motion groups discussed above will add some leeway to this value if numbers permit. These values give the barest 1σ detection and so a baseline of at least 6 years is necessary to ensure measurements of reasonable quality.

The following table lists all plate material used in this work. ESO Schmidt R-band plates are prefixed with an 'e' in their plate number. The table is ordered by increasing field number, with increasing plate number (and hence epoch) within each field). Plates scanned by SUPERCOSMOS are indicated with a tick mark ($\surd$) in column three, others having been scanned by COSMOS . Only five of the fields have plate scans and photometric data of a high enough quality to produce a reliable luminosity function (see Chapter 4 for further details on quality estimates). These fields are 117, 341, 342, 343 and 349. The remaining plate material was selected for various pre-survey studies and was not originally intended to be part of the programme. The three year gap between COSMOS and SUPERCOSMOS has led to the use of this material to extend the red object survey. This type of work does not require such high standards of material and calibration but, as discussed in Chapter 5 has provided the most interesting result of the project. The right-most column lists the sources of principal photometric calibration sequences, which are listed in table 3.5. The reference is given for the first plate in each field and applies to all material for that field, unless a further reference is given for a specific plate.

Table 3.4: Plate material used in the colour-selection programme and the space distribution measurements. Each field has two or more plates in both R and I bands.

Field	α_{B1950}	δ_{B1950}	b^{II}_{gal}	Plate No.	SUPERCOS.?	Grade	Epoch	Ref.
117	03^h 48'	–60°	-45°	J 2635		A	76.7	1,3
				eR 5364		-	83.8	
				I 9647		b	84.8	
				OR 9746		b	84.9	
				I 9747	√	b	84.9	
				OR 15825	√	B2	93.8	
296	01^h 18'	–40°	-76°	J 3524		A2	77.6	4
				eR 4429		-	81.8	
				OR 13216	√	B4	89.6	
				I 13820		a	90.7	
				I 13821	√	a	90.7	
297	01^h 44'	–40°	-73°	J 3593		A2	77.7	2
				eR 4506	√	-	81.9	
				OR 10353		a	85.6	
				I 10435	√	A2	85.7	
				I 10441		A2	85.7	
				R 12688	√	b	88.6	
341	20^h 48'	–40°	-39°	J 2375		A2	74.4	1
				R 4341		B	86.5	
				eR 6600		-	86.6	
				I 7254	√	B2	81.7	
				I 8067		A2	82.6	
				OR 14521	√	A2	91.7	

Field	α_{B1950}	δ_{B1950}	b_{gal}^{II}	Plate No.	SUPERCOS.?	Grade	Epoch	Ref.
342	21^h 14'	–40°	-44°	J 3564		A2	77.7	1
				eR 6596		-	85.6	
				OR 11184		A2	86.5	
				I 11422		B4	86.8	
				I 13883	√	B4	90.8	
				OR 14588	√	A2	91.7	
343	21^h 40'	–40°	-49°	J 828		A1	74.6	1
				R 4478		B4	78.7	
				eR 6227		-	85.8	
				I 7247	√	B3	81.8	
				I 12809		A2	88.8	
				OR 13844	√	A3	90.7	
349	0^h 0'	–35°	-77°	I 3533		a	77.6	5
				R 5363	√	B3	79.8	
				J 6145		A2	80.5	
				eR 7636		-	88.7	
				I 16393	√	A2	94.8	

#	Reference
1	Stobie *et al.* 1983a,b
2	Lasker *et al.* 1988
3	Mighell 1990
4	Cunow 1993
5	Cunow & Ungruhe 1995
6	Metcalfe *et al.* 1995

Table 3.5: Photometric calibration sources for table 3.4

Chapter 4

Plate measuring machines: properties and techniques

4.1 Measuring machines at the Royal Observatory.

This project spans the period which saw the end of one of Edinburgh's plate measuring machines and the start of another. It has not been possible to construct a survey based on a set of measurements from a single machine and so the properties of both are reviewed and compared. Subsequent sections in this chapter discuss reduction of analysis of this data, noting differences, similarities and attempting to assess the quality of SUPERCOSMOS measurements in the project's early stages. The history of the measurement of photographic plates at the ROE goes back to the GALAXY project in 1965. GALAXY is claimed to be an acronym for **G**eneral **A**utomatic **L**uminosity **A**nd **XY** measuring machine. The goal of the machine was to provide astrometric and photometric data limited only by the fundamental accuracy of the plate material (and not the measuring device). GALAXY was limited to the measurement of stellar images and could process up to 900 per hour. The impending southern hemisphere Schmidt surveys promised a supply of data

that far exceeded GALAXY's working speed and so the COSMOS[1] project began. COSMOS began measuring its **C**o-**O**rdinates, **S**izes, **M**agnitudes, **O**rientations and **S**hapes in 1979 (Reddish 1992, assures us that the acronym is genuine). Measuring a whole Schmidt plate with sub-micron accuracy in about 6 hours, COSMOS fulfilled its astrometric role and retired gracefully in 1993. The next generation promised to extract the full range of photometric information from a photographic image as well as improving positional accuracy (by a factor 10) and reducing measuring time by a factor of 3 or so. At The ROE, the SUPERCOSMOS machine has been built to achieve this. It officially began measuring in 1996 and is one of 8 microdensitometers designed for wide-field astronomy currently at work around the world (see Lasker 1995, Guibert 1992, Deul 1992 and de Vegt *et al.* 1992 for details of the other seven).

The principal use of both COSMOS and SUPERCOSMOS is to measure the photographic plates that store the Schmidt sky surveys. In practice this means measuring the (x,y) position and light transmission through the emulsion for each of the 10^9 $10\mu m$ -pixels per plate. Any other information derived from a scan is a function of position and transmission and so these values determine the accuracy of all subsequent uses of the data. As stated for the GALAXY project, the intention of the measuring machines is (ideally) to contribute no noise to the measurement process. The designs employed by the two (real) machines to ensure that photographic noise dominates are very different.

4.1.1 COSMOS

(Figures quoted in this section are from the report by MacGillivray & Stobie (1985) unless stated otherwise.) The light source used to measure transmission in the COSMOS machine was a spot generated by a cathode ray tube. A photomultiplier tube recorded the light intensity and the photographic plate sat between the two instruments. COSMOS achieved its speed by using a 'flying spot' which

[1] When the text refers to COSMOS, I am referring to both the COSMOS and SUPERCOSMOS machines. Individual machines are referred to by quoting the name in SMALL CAPITALS style.

swept in the x-direction whilst the carriage holding it moved in the y-direction, producing a television-style raster scan of a rectangular 'lane' on the plate. The positional accuracy is registered prior to each lane measurement using Moiré fringe gratings and scanning began after the carriage had stabilised to $0.5\mu m$ in x and y. Accuracy within the lane depended upon the chosen spot and pixel size. For a $16\mu m$ increment, used to produce the data used in this survey, an accuracy of $\pm 4\mu m$ was attained for a single pixel. Image positions based on intensity-weighted centroids can reduce this random noise to about $1.2\mu m$. Consistency during the six hours of a scan was achieved using a climate-controlled room with a temperature stabilised to 20±0.5 °C, to reduce physical expansion and contraction. The room was kept dust free by filtering particles larger than $2\mu m$ and maintaining an over-pressure in the room.

The halo generated by the CRT spot accounted for 5% of the light and led to reduction in the measurable contrast. The limiting dynamic range of COSMOS emulsion density measurements as a result of this is given as 1.2 density units above the local sky density. The IIIaJ emulsion is used as an example: COSMOS noise exceeds photographic noise when measuring densities above 2.5D, where emulsion range is from zero to three. The quoted photometric accuracy, based upon intensity-weighted measurement is ±0.03 magnitudes, though in practice measurement of a single plate is limited to about ±0.1 mag. (Reid 1992). A final restriction on the scanning of Schmidt plates should be mentioned: the physical arrangement of the table limits the measurable area of a plate to the central 286 x 286mm square. This usually results in the loss of images close to the plate edge. As these images suffer heavily from the effects of vignetting, they are usually discarded unless a study of plate-plate overlapping is being made. This is not important in this project and so the limitation is not important.

4.1.2 SuperCOSMOS

SUPERCOSMOS differs from its predecessor in the way that it measures light. As

with the nascent PPM machine at the US Naval Observatory (Lasker 1995) it uses a single-dimensioned CCD-based system. Each of the CCD's 2048 pixels has a size of 10 x 10 μm which measure light from a slit-focussed laser source as the array is drifted in the y-direction. Spanning the width of a single (1280-pixel) lane, the fixed line of pixels performs the job of the flying spot in COSMOS . The granite measurement table is designed to give a positional accuracy of better than $0.3\mu m$ which is achieved partly by controlling temperature in the dust-filtered room to within 0.05 °C. Working under these conditions the machine can scan a plate at $10\mu m$ resolution (0".7) in 2 hours. The physical design of the machine enables plates of 0.5 x 0.5 m to be fully scanned which removes the 286 x 286 mm restriction of COSMOS and allows the edges of plates to scanned. In terms of astrometry and photometry SUPERCOSMOS promises to work close to the measured limits of photographic emulsions. Astrometric precision is limited by emulsion granularity and, according to Lee & van Altena (1983) is around $0.4\mu m$ and is independent of image size provided the images are over-sampled by at least a factor 3 (which SUPERCOSMOS should just achieve for images with 2-3" seeing discs). The CCD array allows measurement of densities of up to 2.3 units above the sky level (*c.f.* 1.2 for COSMOS). As yet, the effect this has on the quality of photometry has not been reported.

4.2 The reduction and analysis of COSMOS data

The following sections describe the process of taking raw COSMOS data and producing a catalogue of stellar positions, displacements and photometric colours. Five stages are involved:

1. Reduction by rejection of unwanted parameters.
2. Pairing images on a plate with their counterparts on all other plates.
3. Classifying the images as stars, galaxies or other.
4. Calibrating the COSMOS magnitude scale to a photometric system.

5. Measuring image displacements to give relative proper motions.

The density map produced by a typical COSMOS scan is roughly 1 gigabyte in size. Before the methods listed above can be applied, this map must be reduced to a catalogue of images. The COSMOS unit's image analysis software performs this task which involves producing a median-filtered map of the background sky intensity. A pixel-connecting algorithm (Thanisch *et al.* 1984) builds images from those pixels that lie above a given intensity threshold. This threshold is usually set to around 10% of the local (interpolated) sky intensity. Each detected image is then described by a set of pixels from which up to 32 parameters are calculated. This *Image Analysis Mode* (IAM) dataset is typically a few tens of megabytes in size and it is in this form that the measurements are subjected to the five stages listed above.

The first stage involves the reduction of the dataset by retaining only 10 parameters. These parameters are right ascension, declination, rectangular plate X,Y centroid co-ordinates, area, peak image intensity, local sky intensity, semi-major (a) and -minor (b) axes of the ellipse fitted by IAM software to the image and 'COSMAG', the instrumental magnitude. The X, Y, a and b values are intensity-weighted. The first pair of parameters are required for image pairing, the second pair for proper motion measurement, the next five for image classification and the final one for photometry.

4.3 Image Pairing.

To produce a multi-colour photometric catalogue from digitised photographic plates, each scan of a survey field must be matched image-for-image with the other scans of the field. This *pairing* stage is carried out on COSMOS IAM data files that have been reduced and re-formatted as discussed above. The pairing process allows the rejection of spurious images due to emulsion and machine noise as such images have no counterpart on other plate scans. The process requires a *primary* plate to

act as the co-ordinate frame on to which the other *secondary* scans are matched. A pairing radius around each primary image defines the detection criteria. The size of this radius determines the efficacy of the process and places limits on the survey's completeness and level of kinematic bias. The best pairing radius to use depends upon the photometric colour, the brightness, plate position and number density of the images. Two pairing stages are used to deal with these factors. A preliminary pairing stage is carried out to match as many of the primary images as possible. A further pairing stage then refines the result of the first stage by filtering out likely mis-pairs using criteria based on the images' brightness and plate position.

4.3.1 Choosing a primary plate.

The primary plate should ideally contain more real images than any other plate of the survey field. This generally means that the IAM file with the most images is chosen. Since the survey requires R and I colours for each image, the primary should be in one of these wavebands. Although the infra-red subjects of this survey will be brighter on an I band plate, an R plate is chosen as the primary for each field for 2 reasons; firstly, R plates are usually more sensitive and so go deeper in terms of faintness, detecting more objects (compare $R_{lim} \approx 21.5$ to $I_{lim} \approx 18.5$). Secondly, the ability to detect an object with the extreme red colour of R–I$\approx$ 3.0 is fixed by the limiting faintness of the R plate since an I=18.5, R–I=3.0 object will be detected on an I plate but not on an R plate).

The total image count can be affected by large numbers of spurious images usually due to emulsion noise peaking above the COSMOS detection threshold and from images being *blended*. Such contamination shows-up as fluctuations in the generally smooth rise in image count as a function of magnitude (increasing faintness). Figure 4.1 shows the log(number)/magnitude curves for two plates of similar waveband in field 117. One measured by COSMOS (a) and the other by SUPERCOSMOS (b). Both plates show excess images at the faintest magnitudes which contribute

significantly to the overall image total. The SUPERCOSMOS measurement shows a marked deviation from smoothness, almost certainly due to the machine since this is preliminary SUPERCOSMOS project data. Such deviations would rule-out the use of the plate as a primary, and in this case raise doubts about the overall quality of the data.

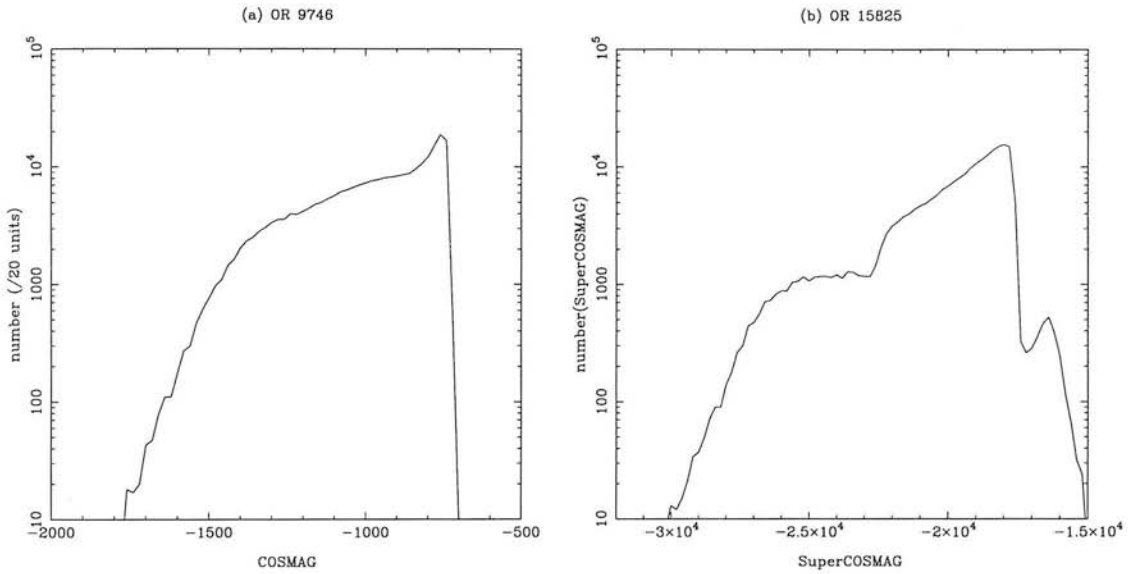

Figure 4.1: Raw magnitude distribution for R band plates of same field. (a): COSMOS , (b): SUPERCOSMOS

4.3.2 Image quality.

Image *quality* refers to the how well the COSMOS image represents the original image produced at the telescope. Uncertainty in the measurement of position occurs due to distortion of an image during the photographic plate's exposure, development and digitisation stages. The causes of image distortion are summarised below:

- Trailing due to telescope tracking errors during the exposure time of the plate.
- Variations in emulsion sensitivity across the plate.

- Image 'quantisation' due to digitisation limits of the faintest images.
- Two or more close or over-lapping images being blended into a single image.

As discussed in section 3.2, all UK Schmidt plates are graded by the UKSTU. This grade is the most reliable indicator of the overall quality of the *plate*. The quality of the COSMOS *scan* of this plate can be studied by examination of image axial ratios based on the COSMOS intensity-weighted semi- major and minor axial values assigned to each image ellipse. For stellar images the axial ratio should be close to one since the images are just near-circular seeing discs.

4.3.3 The first pairing stage: Image number density.

For the preliminary stage the primary plate is chosen as a reference frame to which other plates are compared. COSMOS data provides two image co-ordinate systems. Celestial co-ordinates based on astrometry of FK5 stars and accurate to $\leq 0''.5$ are given as equinox J2000 and scan-dependent cartesian co-ordinates quoted to $0.01\mu m$ are available based on both intensity weighted and un-weighted image centroids. For the job of image pairing the celestial co-ordinates are sufficiently accurate and avoid the necessity of plate-to-plate transformations required by the more accurate X,Y values. Having chosen the primary plate and reference frame, a search radius is defined around each primary image. The closest secondary image found in this area is chosen as a successful pair with the secondary image record appended to the primary image record. This produces a file which contains all of the original primary images plus those secondary images which were matched to a primary. Any other secondary images are lost at this stage and are assumed to be spurious.

The size of the search radius used varies with each plate pair. The value is determined by calculating the mean image separation on the secondary plate. The pairing radius is set at one arcsecond below this distance, to a minimum of 5

arcseconds (a lower limit based on the results of testing the first pairing stage). The pairing radius has a typical value of 20" and ensures that almost all of the primary images are matched including any high proper motion objects which may be important in nearby star survey.

Many mis-pairs ($\sim$ 15%) are introduced into the data however and the problem is exacerbated by the fact that the chosen pairing radius is a mean value. There are generally fewer images towards the plate edges due to optical vignetting and so the pairing radius over-estimates the mean separation of images in more densely-packed central parts of the plate which encourages mis-pairing. The problem is offset by compiling, for each primary image, a list of all candidate pairs. The nearest of these candidates is chosen as the pair and rest rejected. This ensures that a primary is unlikely to be paired to a spurious secondary image at the expense of a genuine one but does not alleviate the problem of primary images being paired to spurious secondaries when no genuine pair exists (either due to the poorer quality of the secondary plate or the fact that the primary itself is a spurious image). To correct for this type of mis-pair, a second pairing stage is carried-out rejecting spurious images on the basis of a statistical analysis of this first pairing stage.

4.3.4 The second pairing stage: Image brightness and position.

The actual co-ordinate scatter for genuine image pairs is much less than the twenty-or-so arcseconds used in the first pairing stage. The distribution of the scatter for all images paired at that stage is illustrated, for typical plate pairs between four wavebands, in figure 4.2. The distributions show a narrow Gaussian peak with a small tail. The peak, whose full width is generally less than five arcseconds, is the contribution from genuine image pairs and the tail is due to mis-paired images and accounts for around 15% of the total number of primary images. Around 10% of these images are lost due to blending (Heydon-Dumbleton *et al.* 1989), leading to genuine secondary images being mispaired. The remaining 5% or so are

due to the pairing of spurious images caused by the use of a large pairing radius and the presence of many spurious images on both plates. The figures reveal the wavelength-dependence of the image-pairing process. For the R_{63F} to R_{59F} and R_{63F} to I_N pairings, there is a small transformation error of around one arcsecond and relatively low dispersion about this compared to the scatter in the R_{63F} to B_J pairing about an offset two arcseconds and scatter extending to four arcseconds (in agreement with previous measurements: Mitchell, 1989).

By fitting a suitable curve to the genuine image distribution we can filter out the large-separation mis-pairs, but this does not solve the problem of the mis-pair distribution underlying the normal curve. A study of how the images within the Gaussian are distributed reveals that the genuine image scatter is dependent on image brightness and plate position.

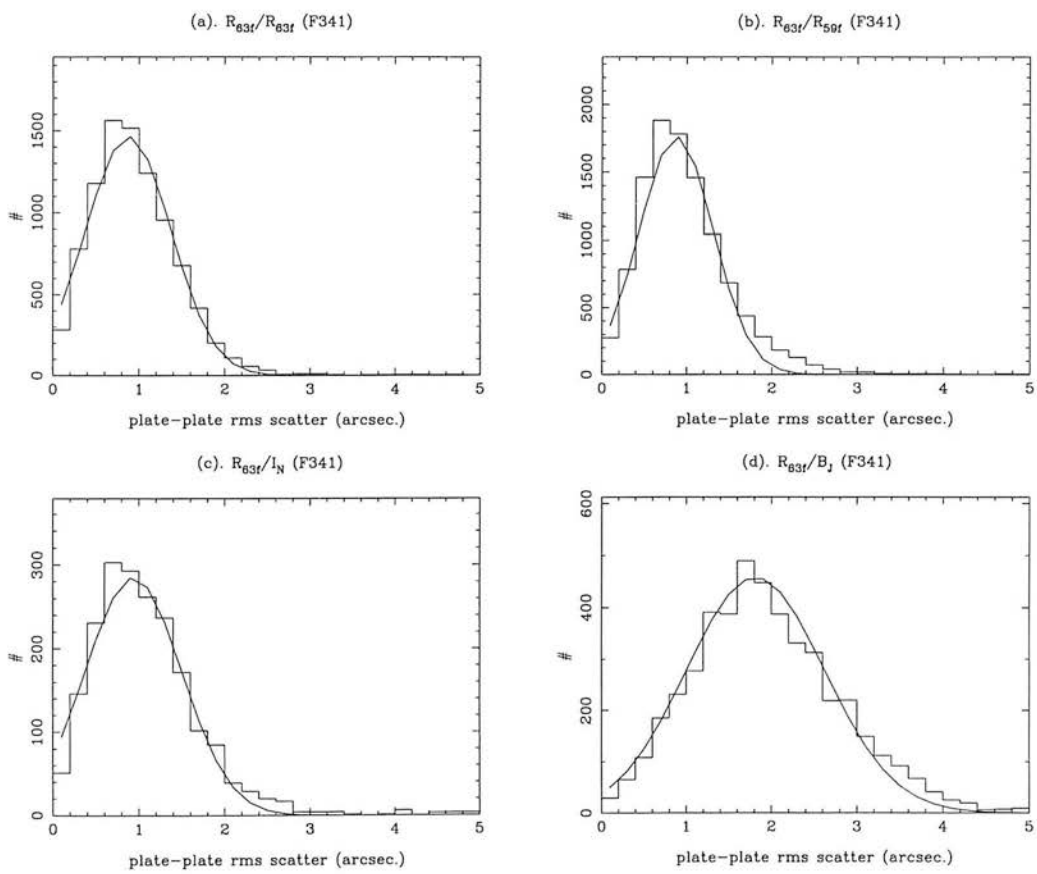

Figure 4.2: Pairing scatter between plates of various wavebands.

Image brightness.

The plate co-ordinate assigned to an image is determined from the centroid of an intensity-weighted ellipse fitted to the pixels that make-up the COSMOS image. The lower limit to image size can be set prior to the COSMOS scan and is set at 3 pixels for all scans used in this survey. Because of the east-west direction of the scanning head, such small images are measured as east-west ellipses rather than true circles and this reduces the accuracy of the positional measurement. The brightest images show large diffraction spikes which align themselves east-west and north-south. These spikes can be broken-up into separate images by the image analysis software and this leads to asymmetries in the overall shape of the image which, again affects the positional measurement.

This variation in positional accuracy is dealt with by determining the scatter distribution (the primary/secondary image separation) for each magnitude bin (in this case, bins are 20 COSMAG units wide). An upper limit to the genuine image distribution (defined as $\mu \pm 3\sigma$) is determined and secondary images with larger scatter are rejected. The mean value, μ accounts for the underlying transformational error and the width, 3σ is chosen such that the limit results in the rejection of no more than 15% of the primary images (as discussed above). The effect of plate position on the scatter for each brightness group is also accounted for. The variation in the measured 3σ width with instrumental magnitude for each of the plate pairs represented in figure 4.2 is shown in figure 4.3. It is clear that there are minor variations across the common range with a slight decline for the brightest images, partly hidden by the poor numbers counts in these brightest bins.

Image position.

The optical vignetting of photographic plates, the effects of differential atmospheric refraction and the random variations in emulsion sensitivity all contribute to the variation in the brightness, size and therefore quality of images across the plate. The vignetting function and refraction properties are well understood (UKSTU

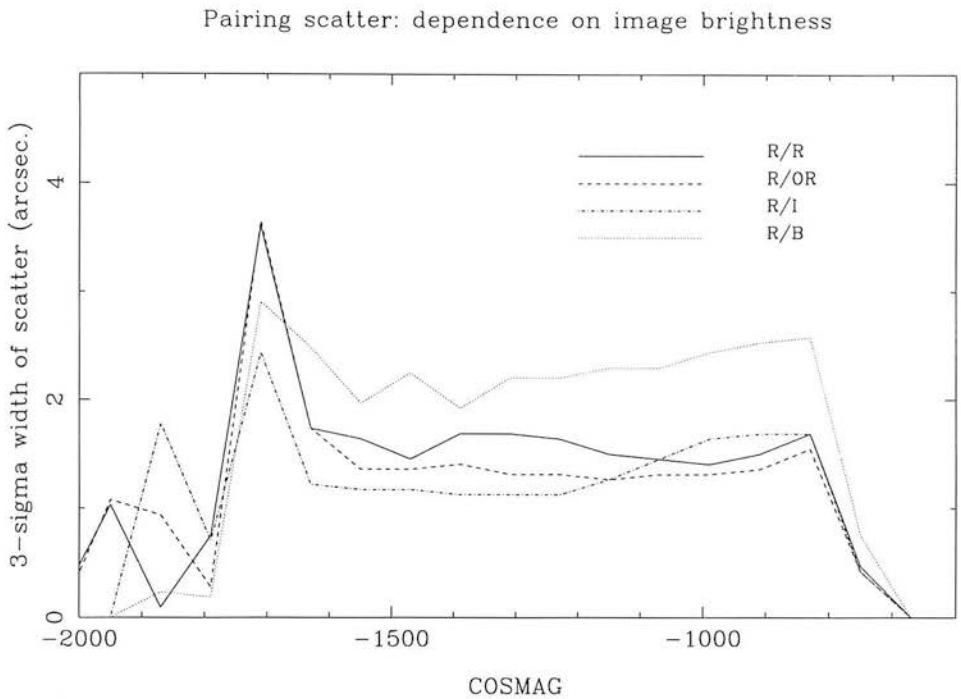

Figure 4.3: Variation in the width of the plate-to-plate pairing scatter with instrumental magnitude (COSMAG: see §4.5). The four lines represent the pairing of a single R_{63F} plate to a single plate of one of the following wavebands: R_{63F}, R_{59F}, I_N or B_J, based on field 341 measurements.

handbook , Tritton 1983) and result in a quite sudden drop in the number of images with radius beyond 3° from the plate centre. Emulsion variations are generally randomly spread and therefore impossible to account for analytically, although the magnitude of the variations seems to be emulsion-dependent (with the IV-N emulsion being the worst case). By producing a magnitude-binned scatter distribution for small regions of the plate, the affects of local emulsion variations can be compensated for and the affects of vignetting and refraction are automatically dealt with. The chosen area is 30mm x 30mm, which produces a 10 x 10 grid on the plate and should account for variations in positional accuracy over scales of a few centimetres (see §4.6 for further details).

summary.

The positional scatter of each image pair then, is added to a histogram on the basis of the primary brightness and plate position. A Gaussian curve is fitted with the least squares method and an upper limit to the genuine image scatter is defined as $\mu \pm 3\sigma$ where μ is the curve's mean value, σ is the standard deviation and the factor 3 has been chosen by manual examination of the results of the initial pairing process on several sets of plates. The usually results in a cut-off radius of four to five arcseconds. Images which lie outside this limit are flagged as a likely mispair but retained for further study as a proper motion objects (see §4.6). Pairing the IAM data in this way results in a catalogue of images with comparative measures of brightness, position and shape which can be used to discriminate between the different populations of detected objects.

4.3.5 Kinematic bias

A stellar survey based on the photometric selection of images from photographic plates is subject to a kinematic bias due to the fact that the sample has been compiled by pairing images of each member on different photographic plates. This process involves defining a pairing radius around each master (or 'template') image within which the corresponding image is searched for on secondary plates. Any star whose proper motion exceeds the pairing diameter will not be detected, resulting in a biased sample. The baseline between the photographic plates, i.e. the difference in time between the exposure of the plates will determine whether the chosen pairing radius is large enough to detect a given proper motion. For example, a 1" radius used to pair plates with a baseline of 5 years will only detect stars that have motions of 0".2 yr^{-1} or less.

In a photometrically-limited survey this bias acts against less luminous stars which must be relatively closer to be detected. The nearer a star, of a given tangential velocity, the larger its proper motion and thus the more likely it is to be excluded form the sample. Using too small a pairing radius then leads to a sample which under-represents both low-luminosity and high-velocity stars. Expressed differ-

ently; we can define the magnitude and velocity range of our survey by choosing a pairing radius to meet our needs. An upper-limit to the pairing radius is given by the surface density of images on the plates, which can be treated as a function of Galactic latitude.

The relationship between the various parameters is derived below. The following symbols are used; R : Pairing radius ("), μ : proper motion ("/yr), V_t : tangential velocity (km/s), D : distance to star (parsec), Δt : baseline between plates being paired (yr). Stars are excluded when $\Delta t.\mu > R$. Since $V_t = \mu.D$ (μ in radians) we can write the bias condition as

$$\frac{V_t \Delta t}{\alpha D} > R,$$

where α scale the parameters to the units given above. The distance, D is related to the brightness of a star by $(m - M) = 5log(D) - 5$, where (m - M) is the 'distance modulus'. The bias condition, written in terms of a star's magnitude and combining the baseline and pairing radius into a single measurable quantity is

$$\frac{V_t}{\alpha 10^{0.2(m-M)+1}} = R/\Delta t. \tag{4.1}$$

The observable limits necessary to avoid bias in a survey can be determined from equation 4.1

Figure 4.4 illustrates how increasing the baseline (epoch difference) with respect to the chosen pairing radius leads to a loss of high-velocity stars and that the effect is most extreme for near-by stars. In this case the radius has been set as 5" which is the typical value used in the pairing routines (see above). The ten curves represent values of the plate baseline from one to 13 years. By using a five year baseline for example, all stars with a tangential velocity below 50 km s^{-1} will be detected whereas a 13 year baseline will lose any stars of this velocity within about 20 parsecs. 80 km s^{-1} is the chosen velocity cut-off for the survey, ensuring the

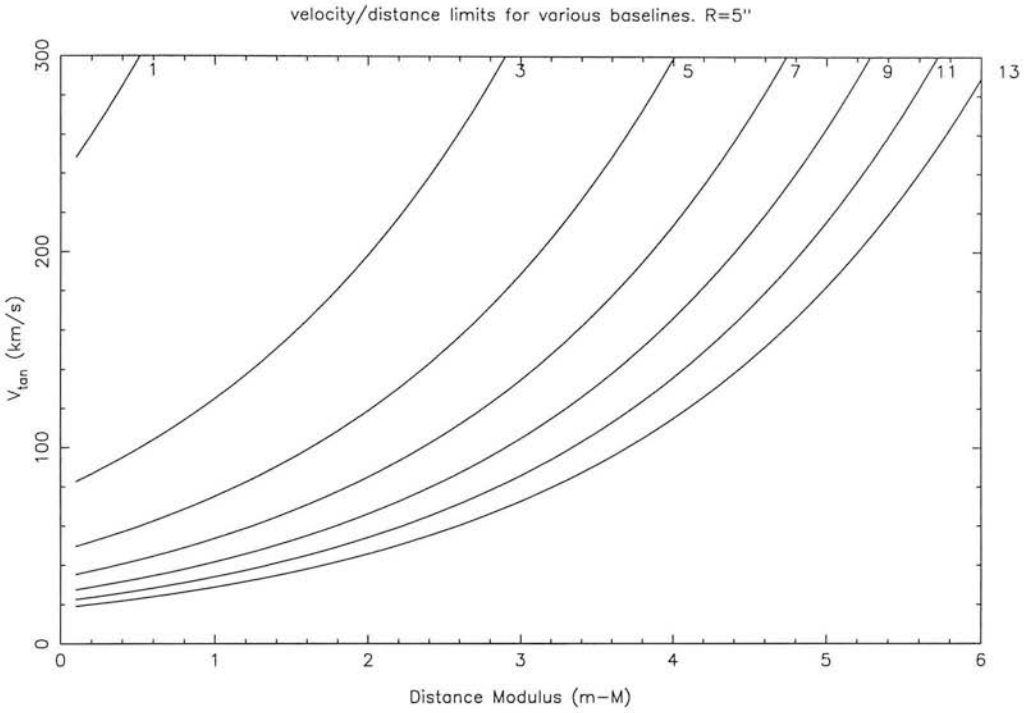

Figure 4.4: The V_{tan} completeness limits for plate-pairs of various baseline paired with a 5" search radius.

full detection of disc dwarfs and the possible rejection of sub-dwarfs. The value $R/\Delta t = 5/3$ must be used for each plate pair which in practice means setting the pairing radius to a value appropriate to the plates being paired. The largest baseline used in this survey is 13 years which thus requires a pairing radius of 21". This radius is close to the typical image separation in mid-latitude fields and so represents an upper-limit to the choice of baseline.

4.4 Image Classification

A stellar survey must contain only stars if it is to be statistically complete. This section discusses the methods used to ensure that images are accurately classified according to type. A measured image could be any of the following types:

Star	Dust (on the plate surface during scanning)
Galaxy	Emulsion blemish
Star-star merged	Satellite trail
Star-galaxy merged	Stray light (internal reflections)
Galaxy-galaxy merged	Unclassifiable

As we are just concerned with deciding whether an image is a star or not the task of classifying according to the types listed above is greatly simplified if we can measure an image property that is unique to stars. The parameters available are those described in §4.2. The principal difference between stellar images and others is that they are essentially point sources of light, convolved with the atmospheric 'point spread function' (PSF) - the seeing. The images are circular (excluding optical and digital distortion) with an intensity profile that is strongly centrally-condensed. If conditions are stable during the plate exposure and the emulsion response even across the field, we can expect all stars of a given magnitude to have the same profile: in fact, to have the same physical image size. Galaxies on the other hand are characterised by low surface brightness and are more likely to have an irregular and less circular profile. Dust reveals itself due to its high opacity for its size and emulsion blemishes frequently appear as spots or irregular shapes and are thus identifiable by a uniformly high light transmission (a non-stellar PSF) and/or by non-circular shape. Satellite trails are reduced by the image analysis routines to a series of highly elliptical images which are easily rejected. Stray light, such as the 'ghosts' discussed in §3.3 either distort large areas of a plate (which must be cut from the survey) or contribute to background intensity variations which affect the photometry of saturated images.

The number of merged images can be reduced by application of *deblending* software which filters each image through a series of isophotal thresholds in order to detect local intensity peaks (Beard *et al.* 1990). A study by Heydon-Dumbleton *et al.* 1989 (HD89) shows that, for South Galactic Pole fields, blended images contribute approximately 10% of the total. Although there is a tendency for the faintest, most crowded images to suffer most from blending, the 10% value appears constant 'over a wide range of magnitudes' due to the effects of overlapping diffraction spikes on brighter stars. The HD89 study was concerned with the effect of blended galaxy clusters; regions with galaxy image densities around 20 arcmin^{-2} compared to the average plate value of 2 arcmin^{-2}. The effect of deblending in this case was to increase the completeness level from 50% to greater than 80% at the expense of creating many spurious images around larger star and galaxy images and having to reject images near to reflection haloes. A study of completeness levels with and without deblending (Beard *et al.* 1990) suggests that for stellar surveys dealing with low surface stellar number densities (i.e. ≈ 2 arcmin^{-2}) the effect of blended images is barely measurable (and above 95% within estimated uncertainties). The quoted improvement due to deblending is on the same level as the uncertainty: less than 5%. Because of the uncertainty introduced by and effort required to remove the unwanted products of deblending, the method is not used in this survey. Tinney *et al.* (1993a) came to a similar conclusion for their photographic star survey, finally deciding to employ the method simply 'on the off-chance that we find that elusive, world-beating brown dwarf candidate among them'.

Two tried-and-tested classification methods have been chosen for this work, based on the image properties discussed above. The first compares image area to (instrumental) magnitude and the second compares a measure of the point-spread width (the sigma or 'S' parameter) to magnitude. MacGillivray & Stobie (1985) and Shanks *et al.* (1984) among others have demonstrated the use of the image area test to discriminate between stars and galaxies for images of intermediate brightness (approximately $15 < B_J < 19$). The log(Area) parameter is preferred due to the large range of area measurements. For fainter images, the S parameter

is preferred. Measuring the 1-sigma width of a Gaussian approximation to the intensity profile of an image, the S parameter as used in this work is defined as

$$S = \frac{-Area}{2\pi} \frac{1}{\log(I_{thresh}) - \log(I_{peak})}.$$

I_{peak} is the peak intensity recorded in the image and I_{thresh} is the background sky intensity threshold for image detection. I_{thresh} is calculated by multiplying the local sky intensity measurement by (skycut/100) where 'skycut' is the percentage sky cut used by the image analysis software. *Area* is the image area expressed in pixels. The S parameter contains intensity information which allows it be used to fainter magnitudes than the Area measurement which is more rapidly affected by image digitisation. HD89 find that it is effective to $B_J \approx 20.0$ but is increasingly less reliable for brighter images due to saturation. Thus the use of both Area and S measurements allows for classification of both saturated and unsaturated images, with only the brightest objects ($B_j < 14.0$) susceptible to systematic misclassification. Being a low mass star survey, such bright images would merit inspection by eye and so the quality of image classification for these bright, rare objects is not of concern.

To quantify the ability of these methods to correctly classify stellar images, a region of field 342 has been chosen as a test field. The region is 25mm^2 in size and centred at $\alpha_{b1950} = 21^h14^m$, $\delta_{b1950} = -39°48'$. Within the field, 214 images ranging from the brightest magnitudes down to a cut-off point several magnitudes above the plate limit have been classified by eye and assigned a type from the first 5 items in the list above. Figures 4.5 and 4.6 show the logarithmic area and 'S' distribition for this field. The six survey plates listed in table 3.4 make up the paired data for this field. Four of these plates are COSMOS data, the other two are measured by SUPERCOSMOS . In both figures plot 'a' shows the distribution for the COSMOS -scanned plate OR 11194 and plot 'b' shows the SUPERCOSMOS -scanned plate OR 14588 to illustrate the machine-dependent differences. Classified and unclassified images are plotted according to the colour-coded key on each plot and further discrimination is made based on an axial ratio cut-off of b/a = 0.7. The axial ratio

cut is chosen by experiment to illustrate the tendency for elliptical images to lie *above* a locus of near-circular images. The locus represents the stellar population, with galaxies and merged images lying above. The choice of magnitude cut-off for the visually classified images coincides with the merger of the populations and represents the limit of accurate image classification.

The distribution is resolved into discrete vertical bands for the faintest images. This is due the 'pixelation' of the smallest digitised images at which scale, the information required by the classification methods is lost. Images this small show a large variation in measured ellipticity as a single extra pixel is added. Figure 4.7 illustrates such variations and informs us that the use of axial ratios in image classification must be dealt with as a function of magnitude. The actual use of the axial ratio data is this work is more subtle than a straight magnitude-dependent cut. The solid line plotted on each of figures 4.5a,b and 4.6a,b represents the result of the *automatic* classication method designed for this survey. The method used is as follows:

1. Divide the plate into a grid of 40×40 mm cells, based on the co-ordinate frame of the primary plate in the paired data set.

2. In each cell: Calculate the log(Area) and log(S) parameters of the images for *each plate scan in the data set* and assign to the appropriate one of 15 instrumental magnitude bins spanning the full magnitude range.

3. Use the first 30 randomly occuring images in each bin to derive a least squares quartic polynomial fit to both distributions on each plate scan.

4. Weight the points contributing to each fit according to $1/\sigma^2 = (a/b)^n$.

5. Calculate the mean χ^2 value for the fits to each plate scan and find the mean scatter. Any plate whose χ^2 deviates by more the 2.5 standard deviations is flagged as unreliable.

6. Classify each image in the cell: above the locus = galaxy = 0, below = star = 1.

(a) COSMOS

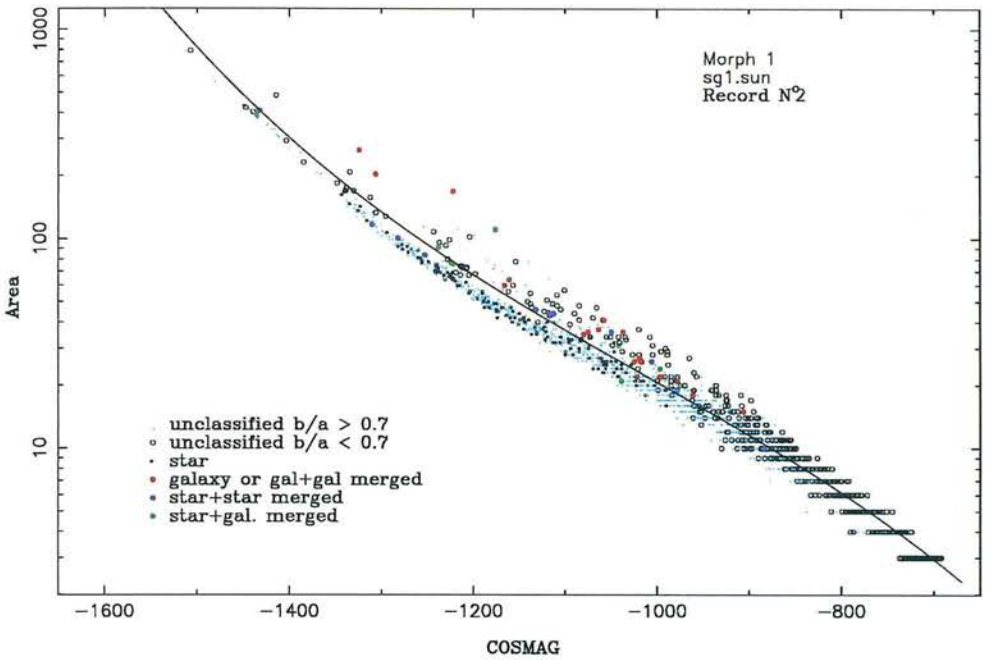

(b) SuperCOSMOS

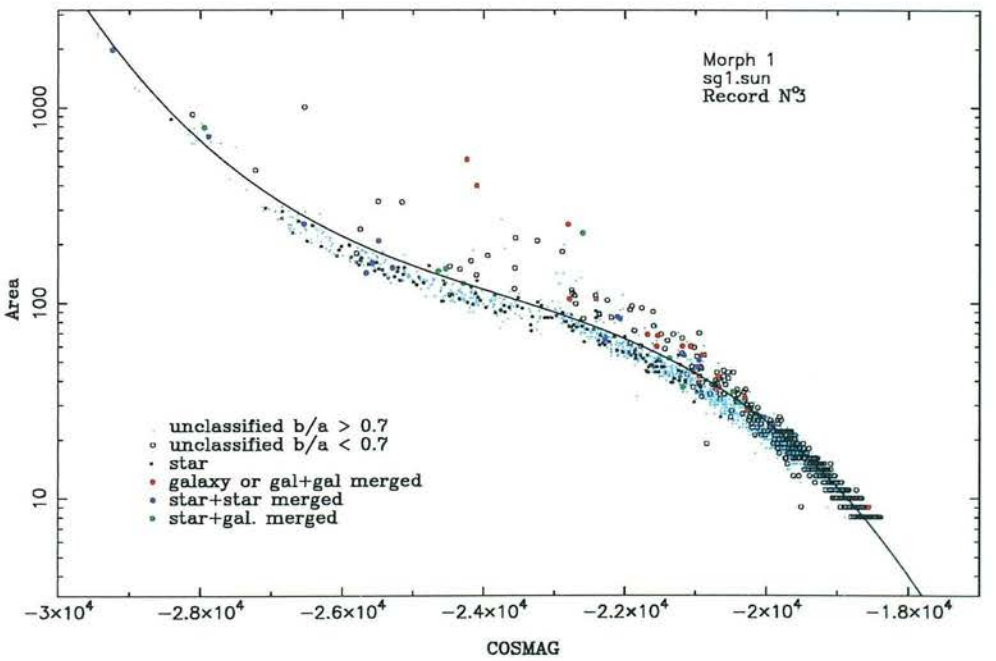

Figure 4.5: Image classification by area.

(a) COSMOS

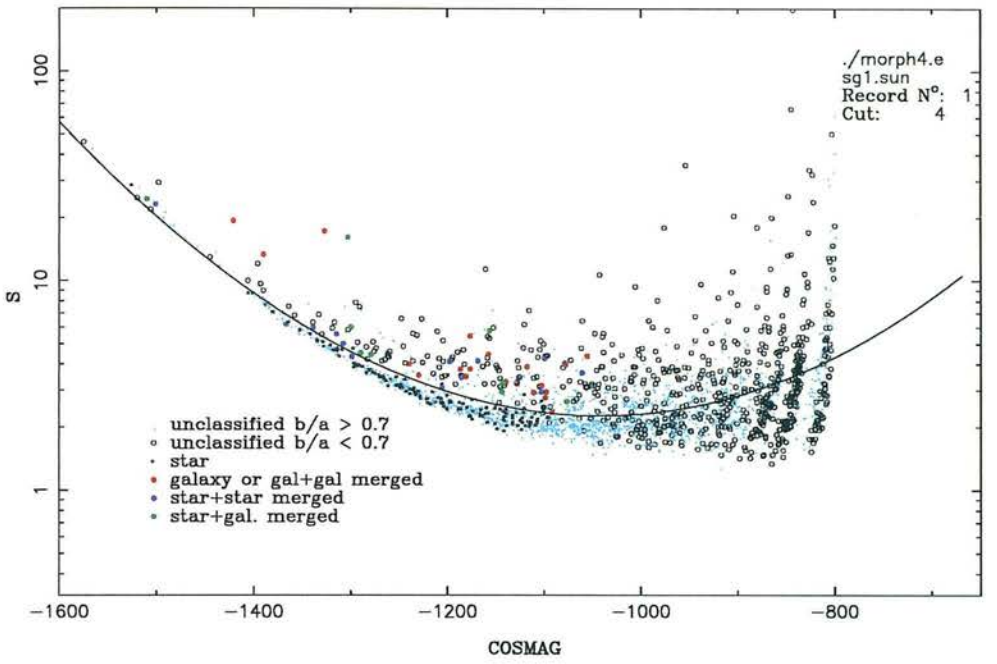

(b) SuperCOSMOS

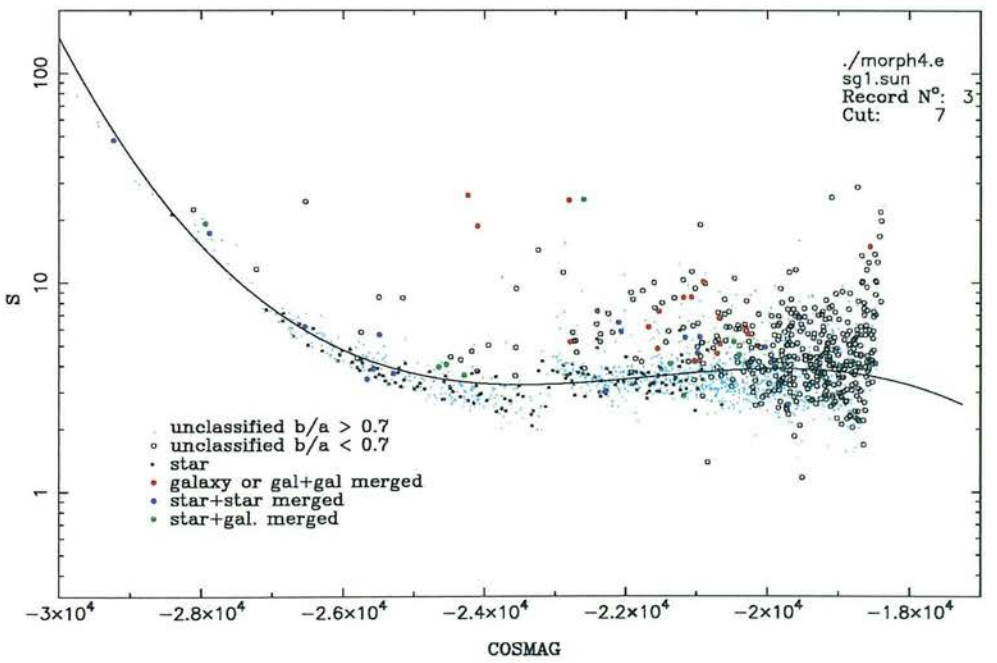

Figure 4.6: Image classification by S parameter.

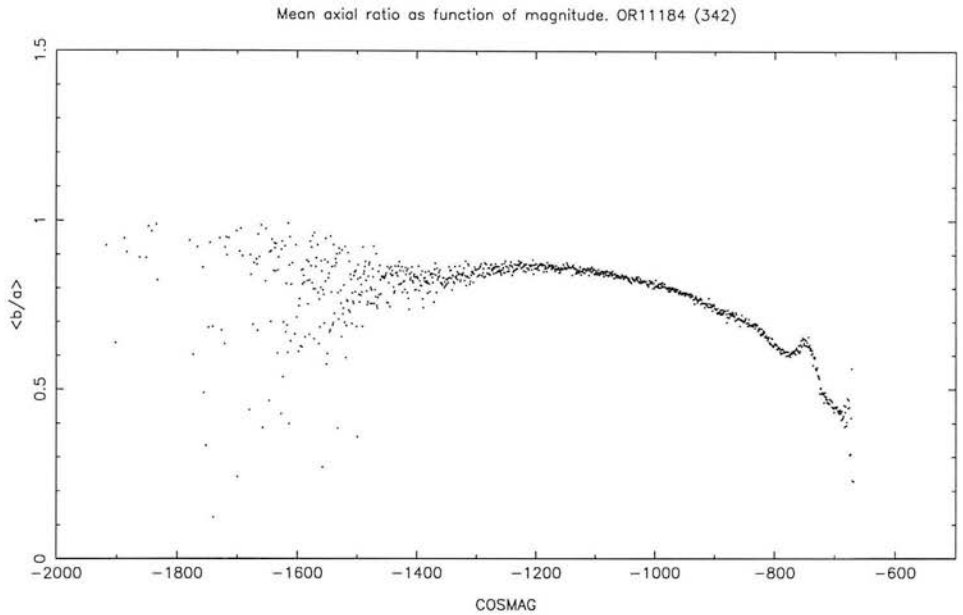

Figure 4.7: Distribution of mean axial ratio in bins of width = 40 COSMAG units.

7. For each image, the accumulated number of stellar classifications (one per plate scan in the data set, excluding unreliable χ^2 rejects) is used to provide an over-all mean classification ranging from 0 to 1 (star to galaxy)

Discussion of the method

The data is divided into cells to account for field variations in both the background sky intensity and the axial ratio distribution. Maddox et al (1990) report (extreme) sky variations of 20% ($\approx 0^{\rm m}.2$) on scales of $0°.5$ (27 mm) and Mitchell (1989 PhD) discusses the effects of axial ratio gradients. The cell size is sufficient to include several thousand images.

Magnitude binning ensures that axial ratio variations are accounted for. The restriction on the number of objects in each bin that is allowed to contribute to the curve fit is to ensure that the fit is not heavily biased towards the faintest images which make-up the majority of the data but cannot be classified due to their poor signal-to-noise level. The value of 30 was found by experiment to ensure that images of intermediate magnitude do not dominate the less numerous bright objects for which the classification method is valid. The images used are chosen

randomly to avoid introducing any further bias.

Weighting the fit with the images' axial ratio to some power is found to be a more valuable use of the ellipticity measurements than a straight cut-off. By experimenting with visually classified images in field 342, indices of $n = -2.0$ for the log(Area) distribution and $n = +1.0$ for log(S) were found to give the best results for all six fields. Using $n = -2.0$ for log(Area) has the effect of weighting the curve *in favour of galaxies* which pushes the curve up above the concentrated stellar locus and ensures that a minimum number of stars are rejected. For log(S) the stellar locus is much less concentrated and the galaxies much more distant, thus the best fit will tend to sit above the stellar locus and the 'pull' of the most distant galaxies is offset by the weakly positive index.

In the case of the field 342 test field, applying both tests to each of the six plates in the data set gives 12 independent classifications for each image. In each case, classification as a star is given the value 1, and 0 for a galaxy. The final classification parameter assigned to each image is a single number in the range 0-1 which is the mean score based on all independent classifications that were not rejected by the χ^2 criterion. Comparing the visual classification to the automated method for the field 342 data suggests that the lowest overall mis-classification rate can be obtained (using the quoted weights) by stipulating that at least 50% of the independent classes must be stellar for an image to be reliably classed as a star. The method described above correctly classified 91.2% of the visually classified images (assuming visual classes to be correct). Variation *either way* produced poorer results. Figure 4.8 illustrates the fractional misclassification of images as a function of stellar classification fraction. That is, a stellar fraction 0.5 implies that at least 50% of the 12 independent classes is stellar for the object as a whole to be treated as a star. The five curves illustrate some of the variation with axial ratio weighting about the global minimum values of $n_{Area} = -2.0, n_S = +1.0$.

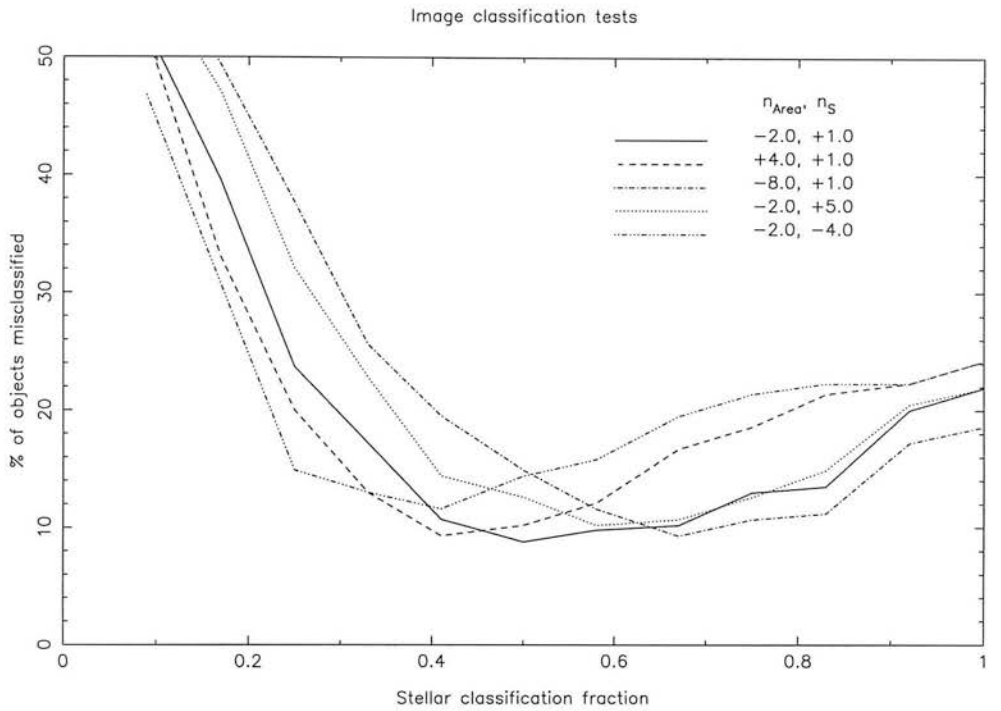

Figure 4.8: Image classification tests.

Galaxy counts

As a test of the classification method across a whole field the surface number density of galaxies in field 342 has been determined in the R_F and I_N bands. The surveys of Tyson (1988) and Jones *et al.* (1991) provide R and I band counts based on CCD and Schmidt plates with which the F342 data can be compared. Tyson's CCD data is based on fainter ($> 19^m.0$) objects which lie beyond the flux limit of UKST survey plates. These data are useful for the I band counts since this band is under-represented in the literature, which mostly deal with the B band. The Jones *et al.* survey uses UKST B_j and R_F plates. The authors present differential log(number) counts that are approximately linear and compare their data to several previous surveys. Although the slopes of the distributions are in good agreement the zero-point varies by up to 20% between the surveys. This is likely to be due in part to uncertainties in colour corrections between the different photometric systems used and variations in the completeness estimates. Table 4.1 summarises the slopes by Jones *et al.* and Tyson along with the values measured

Author	R		I	
	slope	range	slope	range
Tyson 1988	0.41	20-25	0.34	19-23
Jones *et al.* 1991	0.37	19-21	n/a	n/a
This work	0.36	15-19	0.40	14-18

Table 4.1: Comparison of galaxy count gradients.

from the F342 study.

Figure 4.9 shows the differential number counts from F342 in the two wavebands. The distributions are linear as expected from previous work and the measured R and I band gradients are 0.36 and 0.40 respectively. The Tyson and Jones *et al.* linear fits are plotted as dashed lines. The R band gradient and zero-point agree well with the earlier studies and begins to underestimate galaxy counts around $18.^{m}0$ with an uncertainty of greater than 40% at the completeness limit of R = 20.0 where the counts fall-off. The I band distribution is systematically smaller in absolute numbers by around 30%. Metcalfe et al (1995) have noted discrepancies of up to 70% between their deep R band CCD counts (a continuation of the Jones et al study) and that of Tyson. They have transformed Tyson's isophotal photometry to their total photometry and derive a slightly steeper slope (≈ 0.41). It is suggested that the Tyson's choice of survey field may introduce a systematic bias into the counts. The uncertainty that Metcalfe *et al.* introduce by the R_{Tyson} to R_f transform should also be considered.

In conclusion, the image classification method is able to satisfactorily reproduce previous differential galaxy counts in field 342. For images brighter than 18.0 (R) and 17.0 (I) around 92% are correctly classified and below this comparsion to previous number counts suggests that $\geq 40\%$ can be classified correctly to the completeness limit of 20.0 (R) and 18.0 (I). For the intermediate and high galactic latitude fields studied in this work the number-magnitude distribution of classified galaxies provides a measure of completeness limit of the photographic survey which

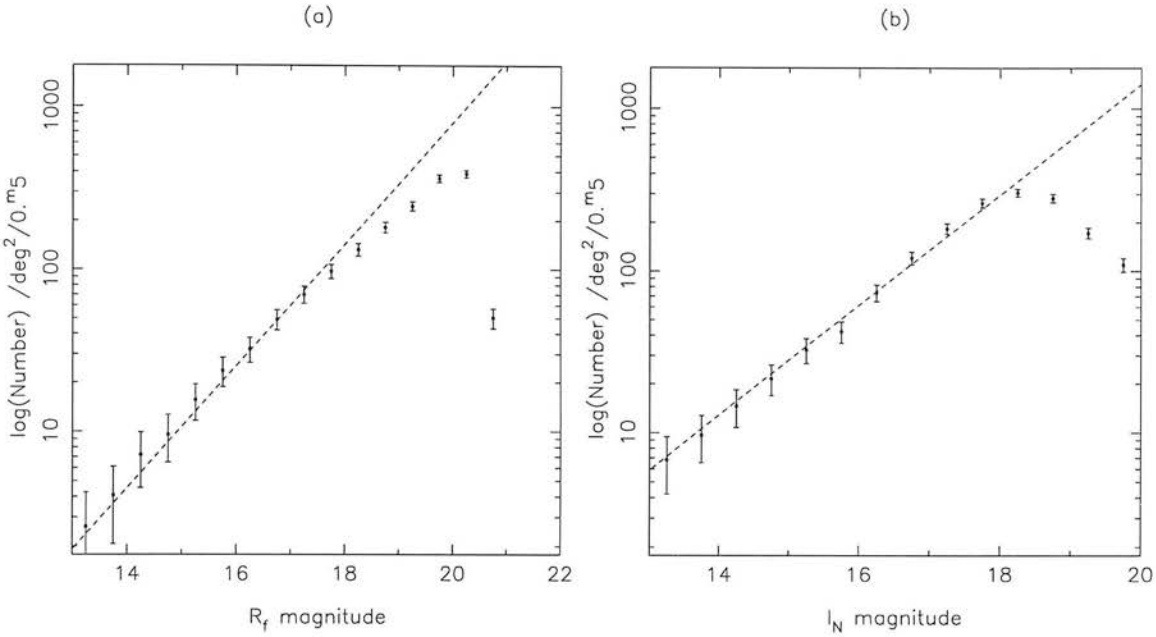

Figure 4.9: Differential galaxy number counts for Field 342. (a): $\log n(\mathrm{R_F})$ compared to Jones *et al.* (1991) slope. (b): $\log n(\mathrm{I_N})$ compared to Tyson (1988) slope.

is simple to measure (log-linear) and less model-dependent than stellar number counts.

4.5 Photometric calibration

4.5.1 Magnitude calibration

The COSMOS machines provide an instrumental magnitude measurement for each detected image. This is defined as $m_{inst} = -250 \log \sum_i (I_i - I_{sky})$. That is, the intensity above the background sky threshold of each pixel, i in the image contributes to the sum which is expressed logarithmically and scaled by -2.5 by convention and by 100 for storage as an integer value. Intensity measurements are based upon light transmission values derived from measurement of the photographic plate's *step wedge* at scan time. The step wedge is a region of the plate edge with several discrete squares of emulsion with densities that have been determined at the tele-

scope using a known light source and a set of neutral filters. The dynamic range of intensity/transmission has been discussed in §4.1.

The photometric range of interest, from about 5^m to 25^m is represented by approximately 2000 discrete values on the COSMOS m_{inst} scale and by 20,000 on the SUPERCOSMOS scale. Calibrating this scale to a standard photometric system requires a set of images in the field of study to be photometered by both instrumental and standard systems. A direct comparison of the values yields a relationship which can be applied to all images in the field. It is important to correct for any colour terms between the photometric sequence and the photographic system. Colour terms such as those given in §2.5.1 are required and thus the photometered objects' colours should not exceed the range of the colour equations. For a stellar survey the images used should preferably be stars, since galaxies generally show a different image profile: a broader exponential shape as opposed to a tighter approximately Gaussian profile. This difference can lead to variations in the isophotal COSMOS magnitude for images of equal total magnitude.

As figures 4.10 a and b show, the response of the photographic emulsion to light across the whole range of measurement varies noticeably. The relationship is characterised by three approximately linear regions of differing slope. For the faintest images, down to about R = 15, there is a straight-forward intensity-magnitude relation which results in a straight line if the density-intensity calibration is good. The curve adopts a different slope for brighter images due to the *saturation* of the instrumental intensity scale. The appearance of a halo and diffraction spikes above the sky threshold for the brightest images is the cause of the second change in slope. For these images, the size of the spikes is also proportional to image brightness and can be used as a simple calibration scale. (see UKSTU handbook for example).

Fitting a low order (cubic or quartic) polynomial is usually sufficient to give a reliable magnitude calibration. Occasionally a sharp change in slope from saturated to unsaturated images and a non-linear density-intensity relation require a spline

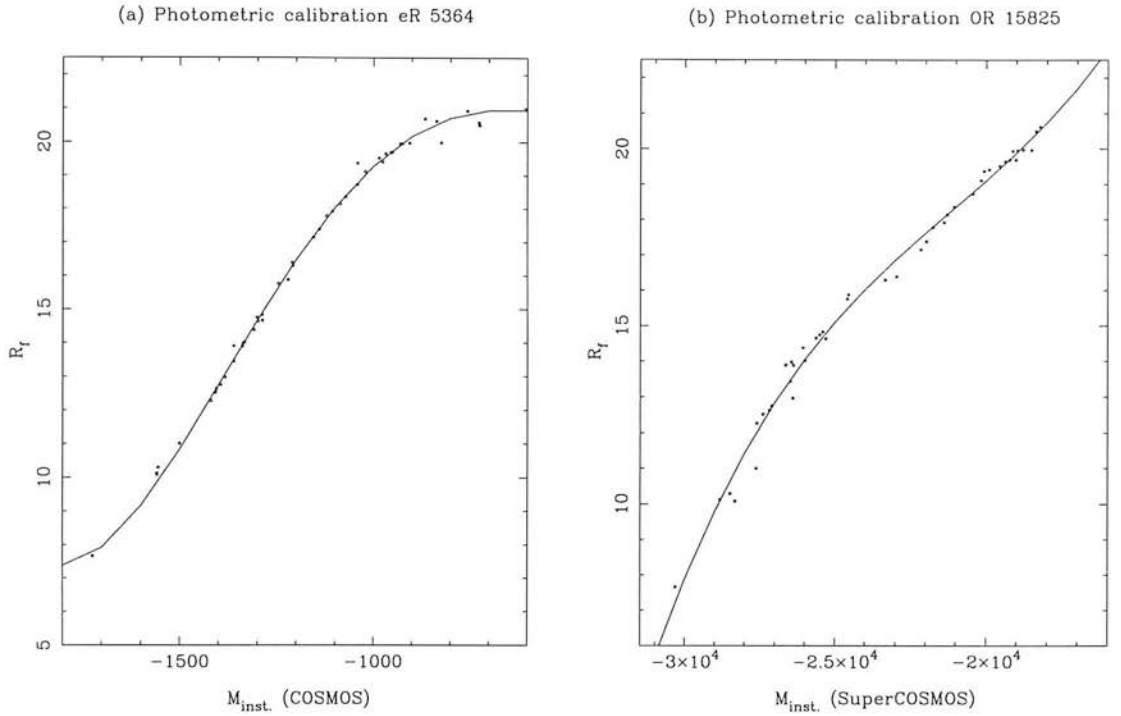

Figure 4.10: Typical photometric calibration curves for the COSMOS (a) and SUPER-COSMOS (b) instrumental magnitude scales.

fit to cope with the kinks. As expected, the scatter about the curve increases with magnitude toward the plate (sky) limit. The scatter for a particular sequence can vary from below $0^m.05$ to over $0^m.5$ across the magnitude range but this is a poor measure of the photometric accuracy. To measure the real variation in magnitude, it is useful to study the rms plate-to-plate scatter about mean magnitude for a set of paired-up images. Figure 4.11 shows this distribution as a scatter plot for the magnitude calibrated R plate data (1 in every 75 stars only) for field 342 (see table 3.4). It is clear from this figure that despite small scatter about magnitude calibrations for brighter (saturated) images, the variation in practice remains in the range $0^m.1$ to $0^m.2$ but increases sharply within a magnitude of the plate limit. Reid (1982) has shown that this value is a broadly applicable lower limit across the range of common emulsion/filter combinations with sets of up to five plates. The independence of this scatter from the fit to the photometric sequence suggests that the reason lies with the variation in applicability of the magnitude

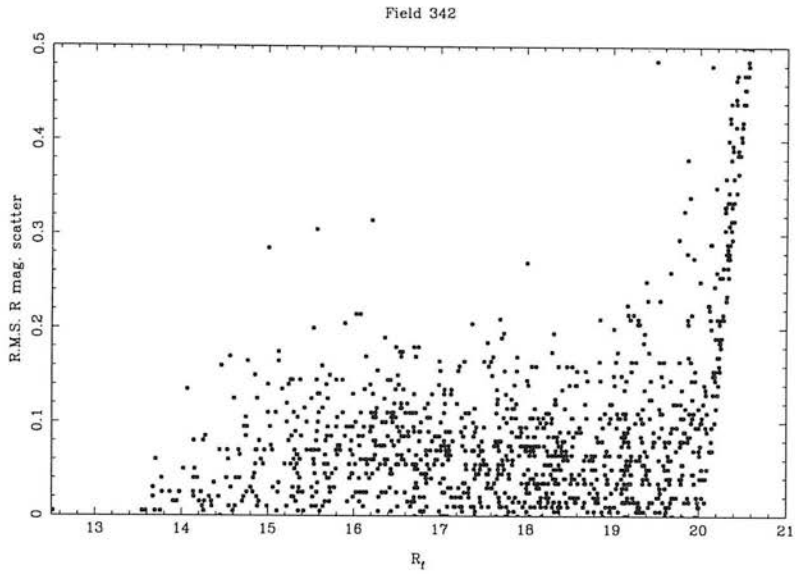

Figure 4.11: Scatter plot of the R.M.S. variation of R band magnitudes for a set of paired stellar images in field 342.

calibration across a whole plate scan. The most important requirement of the calibration is that the resulting scale is *uniform* across the whole field. Although the instrumental-to-standard comparison is straightforward, the achievement of uniformity is not and requires a study of where photometric variation originates, how it varies and how it can be corrected or compensated for.

4.5.2 Field variations

Variations in photometry arise due the unevenness of the sky intensity across a field since this defines the baseline for the isophotal COSMAG scale. As figure 4.12 illustrates this is partly due to photographic emulsion density variations and partly due to the COSMOS sky measurement technique. The figures are based upon measurements of the same plate (I 13883) as measured by COSMOS (a) and SUPERCOSMOS (b). The grey scale measures variations in sky intensity with respect to the median value in the region of a photometric sequence used in the magnitude calibration. The step size being 2 per cent. The immediately obvious difference is the presence of small circular regions of extreme over-intensity (greater

than 14%) in the COSMOS scan, which are due to the presence of bright stars. The SUPERCOSMOS field does not show these features due to improvements in the flat-fielding algorithm used with the new machine. Apparent on both scans however are changes of several per cent (5 to 10) on scales of a few centimetres. This is a feature of the emulsion and the radial vignetting pattern of the telescope.

To appreciate how these variations affect the photometry, consider the method used to determine the instrumental magnitude. Figure 4.13 illustrates the method as applied to unsaturated and saturated images. Using the simple approximation of a $\sigma = 2''.5$ Gaussian profile for a stellar image, a local sky value is determined and a detection threshold I_{th} defined above this. This threshold is typically [2] 10 per cent above the sky intensity and determines which pixels will contribute to the summed intensity of the image (in this case, all those within the isophotal radius R_{iso}). For saturated images (Fig. 4.13 a) the peak intensities are truncated which leads to loss of the signal from the unshaded region at the peak of the profile. The effect of a varying sky intensity on the measured magnitude of an image with respect to the true sky level (that which is measured, say in the region of photometric calibrating sequence) is shown in figure 4.14.

Figure 4.14 a shows how the competing effects of signal-loss through saturation and the over-all growth of the image balance and that the effect of sky variations remains roughly constant, gradually lessening with increasing brightness. In this case image measurements are assumed to saturate at 5 magnitudes brighter than the sky level. For unsaturated images, the increasing importance of the sky intensity inevitably leads to an increasing deviation of measurement from the true magnitude, reaching several times $0^m.1$ within 1 mag. of the plate limit. Despite being a simple simulation, the curves do show the observed behaviour of a relatively magnitude-independent level of photometric scatter of order 0.05 to 0.2 mag. (e.g. Reid 1982). We can be confident then of having identified the largest contribution to photometric scatter across a field in the form of emulsion intensity variations of several percent.

[2] For this work, the COSMOS scans have a threshold of 7-9% and the SUPERCOSMOS scans use 12%

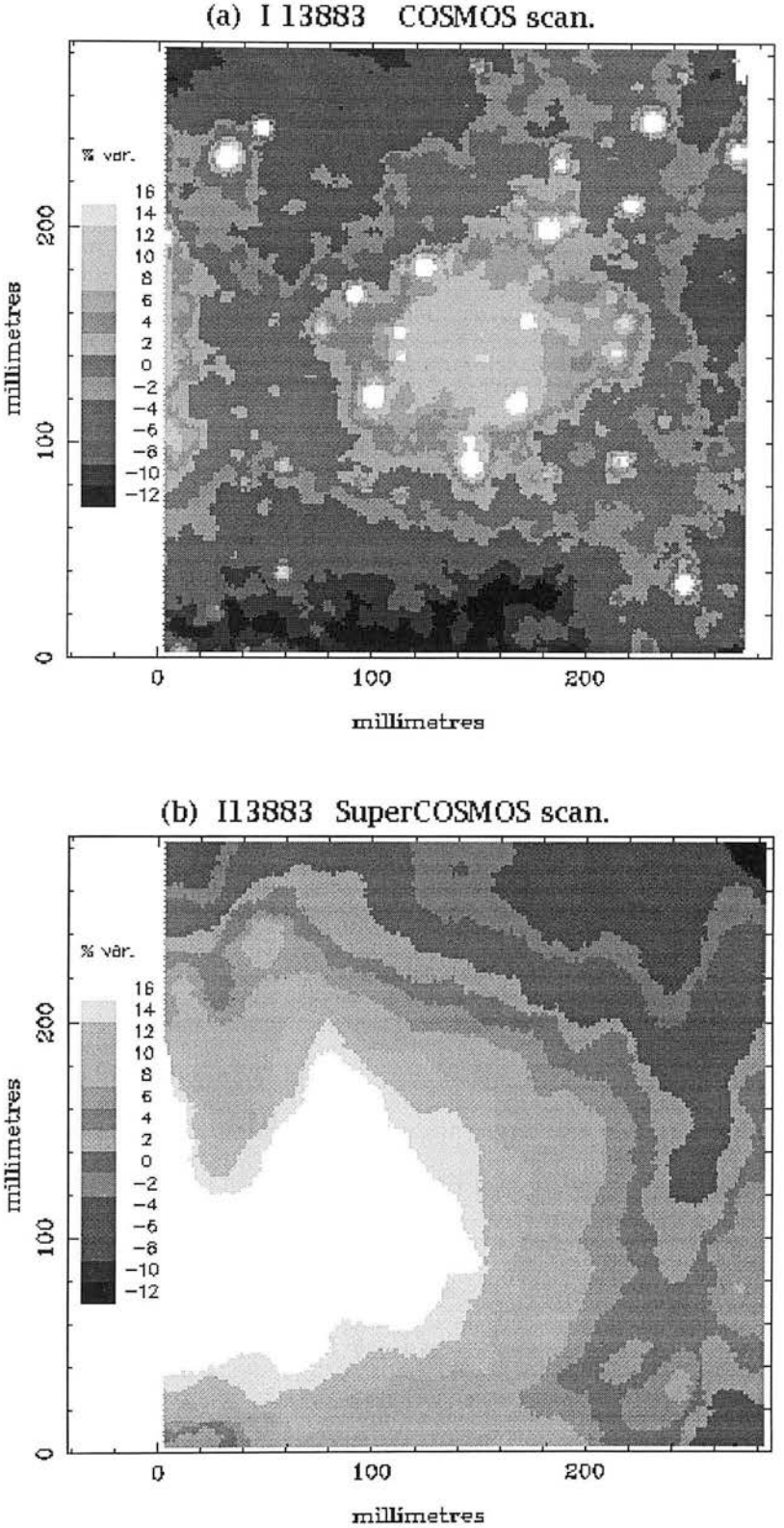

Figure 4.12: Sky intensity variation with respect to the region of a magnitude calibration sequence. Figure (a) shows a COSMOS scan and (b) a SUPERCOSMOS scan of the same plate. Grey-scale steps are 2% variations.

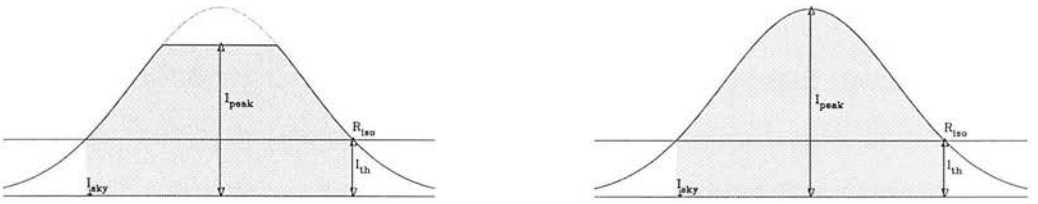

Figure 4.13: COSMOS isophotal magnitude method.

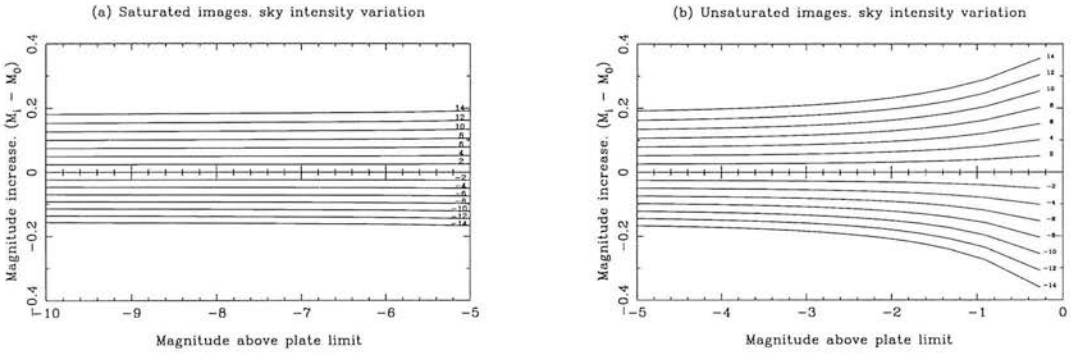

Figure 4.14: The effect of sky variation on magnitude measurement.

In summary, it is not possible to correct for sky-dependent photometric variati unless the sky level in the region is externally calibrated. Figure 4.12 shows how the use of a single photometric sequence can lead to large field variations and thus large photometric uncertainties over a significant fraction of the field. The effect is worsened if, as in this case, the sequence lies near the plate edge or in a region of over or under-dense emulsion. Wide-field variations can be reduced by using several photometric sequences located in regions of differing sky intensity. Ideally, each sequence is used for the magnitude calibration of images found in regions of similar sky intensity. A further measure, that of masking-out regions with sky intensity above a chosen fraction of the sequence sky intensity is also advisable. Figure 4.14 gives some idea of the fractional threshold to apply for a given upper-limit to photometric variation. A $\pm 10\%$ threshold is chosen for this work which should ensure photometric variations of less than $0^{\mathrm{m}}.3$ for all but the faintest objects.

4.6 Proper motion measurement

This section discusses the methods used to measure the proper motions of images detected in the photometric survey. The reason for wanting to know the space motions of the objects has been discussed in chapter 3. Since the displacements are expected to be of order $0''.1$ yr^{-1}, this determines the accuracy of the co-ordinate transformation involved. We have seen in §4.3.4 that the celestial co-ordinates provided with COSMOS IAM data are only reliable for matching images within one to three arcseconds and so these measurements are clearly not of sufficient accuracy for proper motion work. The IAM data also includes the rectangular plate co-ordinates of each image centroid (both unweighted and intensity weighted), quoted to $0.1\mu m$ and $0.01\mu m$ for COSMOS and SUPERCOSMOS respectively.

4.6.1 Choice of reference frame

As discussed previously the requirement of a large epoch difference between the plates under comparison is checked by the need to use plates of the same waveband to minimise the effects of atmospheric refraction. Since the first UKST I band survey is not yet complete, the number of fields that can boast two survey quality I plates of any epoch is small. The story is similar though less severe for R plates and the use of ESO R survey plates can fill the gaps south of $\delta = -20°$ where necessary. Thus the R band plates are used for the measurements. With only two or three R plates per field, the X,Y frame of the *primary* plate is chosen, as opposed to determining a mean frame, which is more appropriate to larger plate sets.

The set of images already paired by α, δ are used to determine the transform from the secondary to primary rectangular co-ordinates. The measurements are thus *relative* as opposed to *absolute* proper motions since the displacements are measured with respect to a non-fundamental frame that is defined by objects that are also moving. The motions within the reference frame will contribute to the

uncertainty in the transformation accuracy and so it is desirable to reduce these effects. The simplest way is to remove a sub-set of images that are likely to show relatively high displacements: galaxies and nearby stars being the obvious candidates. Galaxies may seem to be an ideal fixed reference frame but as figure 4.15 shows, erroneous displacements are often measured due to their often irregular shape and low surface-brightness which hinders accurate centroiding.

4.6.2 Co-ordinate transformation

The transformation of the secondary co-ordinates X_s, Y_s to the master frame accounts for translation, rotation and scale differences, as expressed below.

$$X' = \beta(Y_s \sin\theta + X_s \cos\theta) + A$$

$$Y' = \beta(Y_s \cos\theta - X_s \sin\theta) + B$$

where X' and Y' are the transformed secondary co-ordinates, β is the scale factor, θ the rotational shift and A and B are the translational shifts for X and Y respectively). Higher-order terms (shear) not required as these vary by fractions of $1\mu m$ over the whole plate.

4.6.3 Field variation

The COSMOS measurement tables are designed to preserve their positional accuracy on the scale of one lane and so drifts are inevitable on larger scales. The dominant source of drifts in positional accuracy comes from the variation of temperature during scanning which causes the plates to expand and contract on a scale of several microns. Figure 4.15 shows the variation in R.M.S. transform residuals with field size using COSMOS measurements of survey field 342 plates eR6596 and OR11184. Smaller field sizes remove large-scale effects but reduce the number of images available for the transform. The error bars on the stellar curve

show the variation between the measured X and Y scatter. Dividing the scanned data into cells of side 30mm and using stellar images ensures that large-scale drifts in positional accuracy are avoided and also that there are sufficient stars (several hundred) in the region to provide a reliable transform.

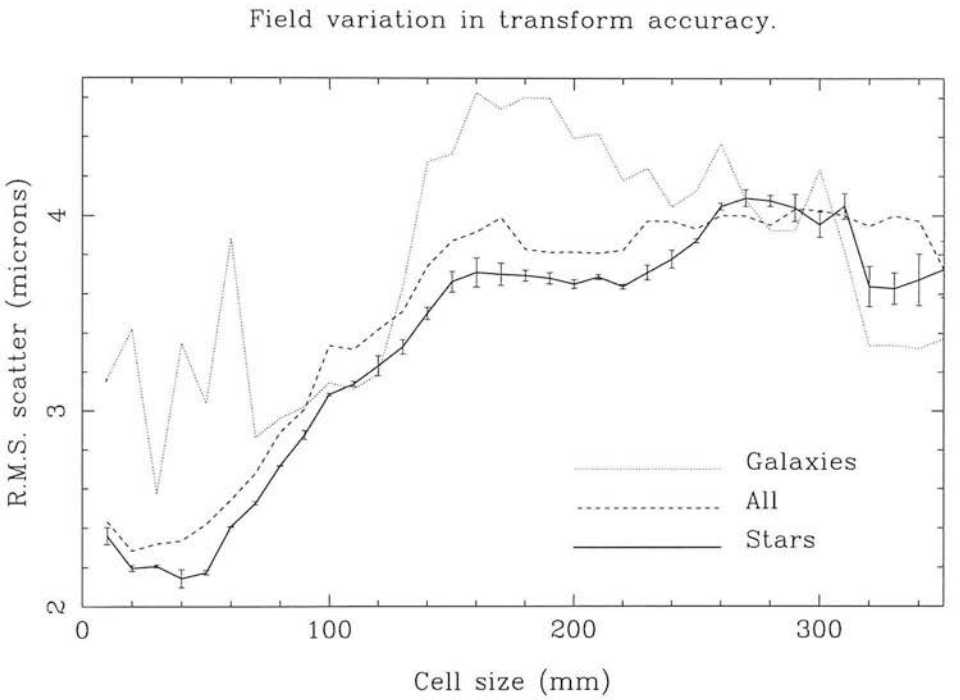

Figure 4.15: Field variations in the rms X,Y scatter for co-ord. transforms in various sub-plate cells. Measurements for three sets are shown: all images in the cell, galaxies and stars.

4.6.4 Choice of baseline

Since the reference frame is defined by stars, increasing the plate-plate baseline will increase the uncertainty in the transformation due to the larger random displacements of the images. In practice, the variation in scatter with baseline is less than $0.4\mu m$ about a mean of $2.6\mu m$ which shows a barely significant increase of around four per cent per year over the available (13 year) range. The choice of baseline then is determined by the pairing requirements explained in §4.3.5 and

the predicted space motions presented in §3.3.4. The image pairing condition sets an upper limit for the given tangential velocity cut and corresponds to the typical image separation on the plate. The proper motion predictions set a lower limit of approximately six years in order to measure small variations in the distribution with 3σ accuracy.

Chapter 5

Results and Follow-up work

This chapter presents two distinct results of the project to survey the lowest mass stars and detect brown dwarfs. A stellar luminosity function for M-dwarfs within 100 pc is presented based upon a 112 square degree survey. This distribution is compared to previous field measurements in the photographic R and bolometric magnitude systems. Secondly spectroscopic observations from a programme to detect brown dwarfs amongst a sample of red objects are presented. The objects were selected from a pre-SUPERCOSMOS analysis of the survey data and so updated photometry is given where relevant. The detection of lithium is focussed upon as the principal means of star/brown dwarf discrimination.

5.1 Luminosity function

With the five primary survey fields listed in Chapter 3 a study of the space distribution of low mass stars, or more accurately cool stars can be made by constructing a luminosity function. This is done in the following steps:

1. Selection of images by photometric colour.

2. Assessment of completeness and contamination.

3. Definition of a distance estimator.

4. Computation of space density.

5. Assessment of bias.

5.1.1 Image selection

With magnitude-calibrated data image selection is based upon R – I colour. All objects that are classified as stars according to the method of §4.4 are chosen from regions of the fields that have been assessed to be photometrically uniform (see §4.5.2). Other contaminants are also possible: mis-paired images, sub-dwarfs and red giants. Mis-pairs often show large variance in individual magnitude measurements; certainly more than the 0.1 - 0.4 mag. expected from field variations. For the faintest luminosity bins where each star is important the actual plate images are checked by eye.

Sub-dwarfs are typically one magnitude fainter for their colour than population I disc stars and so are difficult to identify photometrically. They can be identified by their large space motions (velocities of order 100 km/s) and are likely to be rejected by the pairing radius limits (§4.3.5) or detected as high proper motion objects otherwise.

Red giants can be identified using photometric parallax estimates since they are extremely luminous for a given colour. Gilmore *et al.* (1985) have estimated that giant contamination is unimportant for $V \geq 13.5$ and is less than four per cent for $V \leq 16.5$ in a sample of stars with colour V–I > 1.5. The corresponding photographic R–I lower limit is approximately 0.6 for $R \geq 12.6$.

5.1.2 Completeness and proper motion checks

The apparent magnitude limit for the survey is determined by the least complete plate in the set, that is, the plate scan which shows a fall in the image number

density at the brightest apparent magnitude. Figures 5.1 shows, for R band (a) and I band (b) plates, the galaxy counts for images detected on four or more plates (*i.e.* 2 × R, 2 × I) in the field. The R band images counts fall off rapidly beyond R = 20 and the I band counts continue to around I = 18, suggesting that the overall quality of the I band plate material is better than the R band material. The I band counts show more variation (*i.e.* deviation from linearity) and the apparent I=18 limit may be lower than this. The R band uncertainty has led to the removal of the following plates from the photometric study: OR 15825 (F117)[1], OR 14521 (F341) and OR 14588 (F342). The counts are binned per magnitude and the peak bin is marked on each diagram by the dotted line. This represents the estimated survey completeness limit, which is set at R = 19.0 and imposes no restrictions on the selection of red stars below this, given an I band limit of I = 17 to 18.

After the removal of photometrically suspect regions (see §4.5.2) and accounting for the 3° vignetting cut (§3.2) the remaining usable area for each field, in square degrees is 22.6 (117), 23.5 (341), 21.3 (342), 20.6 (343) and 23.6 (349). The total surveyed area is thus 111.6 square degrees, or 0.034 steradians.

The proper motion measurements for the reddest objects (R-I > 2.0, corresponding to spectral types later than approximately M4) are presented in figure 5.2. The three fields around $21^h, -45°$: 341, 342 and 343 should be compared with figures 3.12 and 3.13 which predict the stellar and brown dwarf distribution for that field. The distributions are in reasonable agreement. The majority of objects in all fields reflect the solar motion with a small number of exceptions. In the case of the field 349 the three objects in the fourth quadrant, may not be part of the local M dwarf group represented by the rest of the sample. The motions are small however and the difference may not be significant. The distributions give confidence that the selection method is correctly choosing red dwarf stars.

[1]see figure 4.1 and accompanying text for further discussion on plate quality.

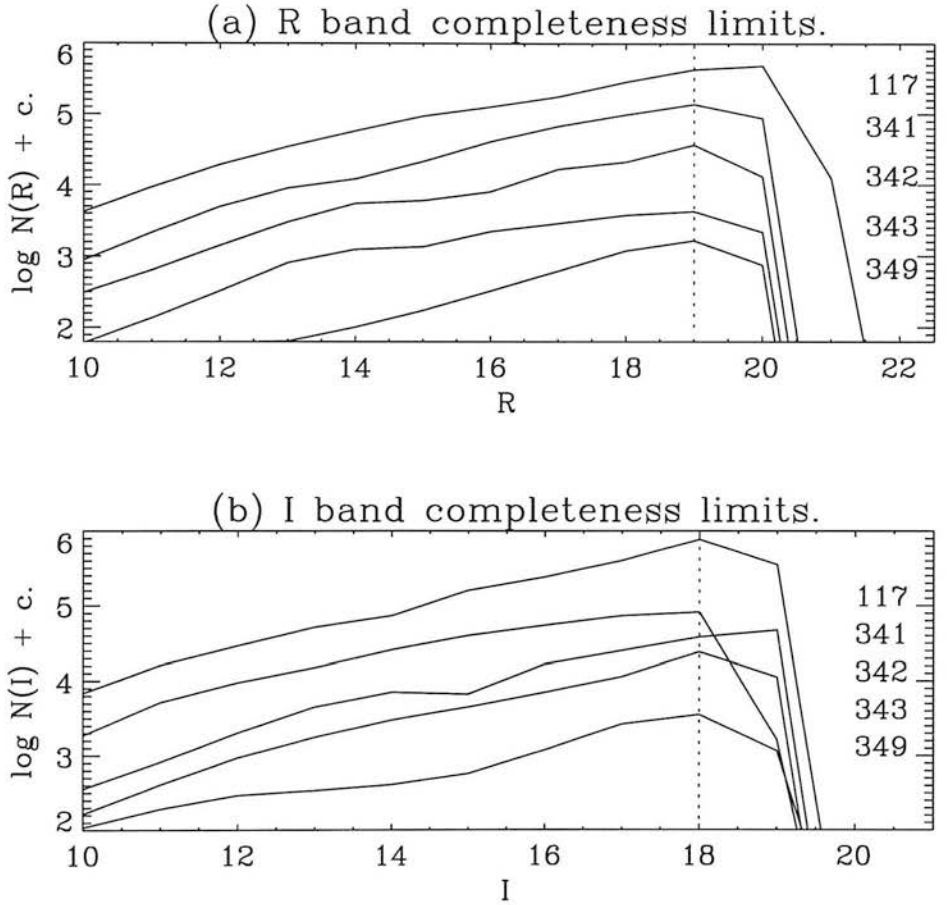

Figure 5.1: Differential number counts in R and I for galaxian images detected on at least 4 plates per field in each of the five survey fields. The estimated completeness limit of the combined data set is marked by dotted lines.

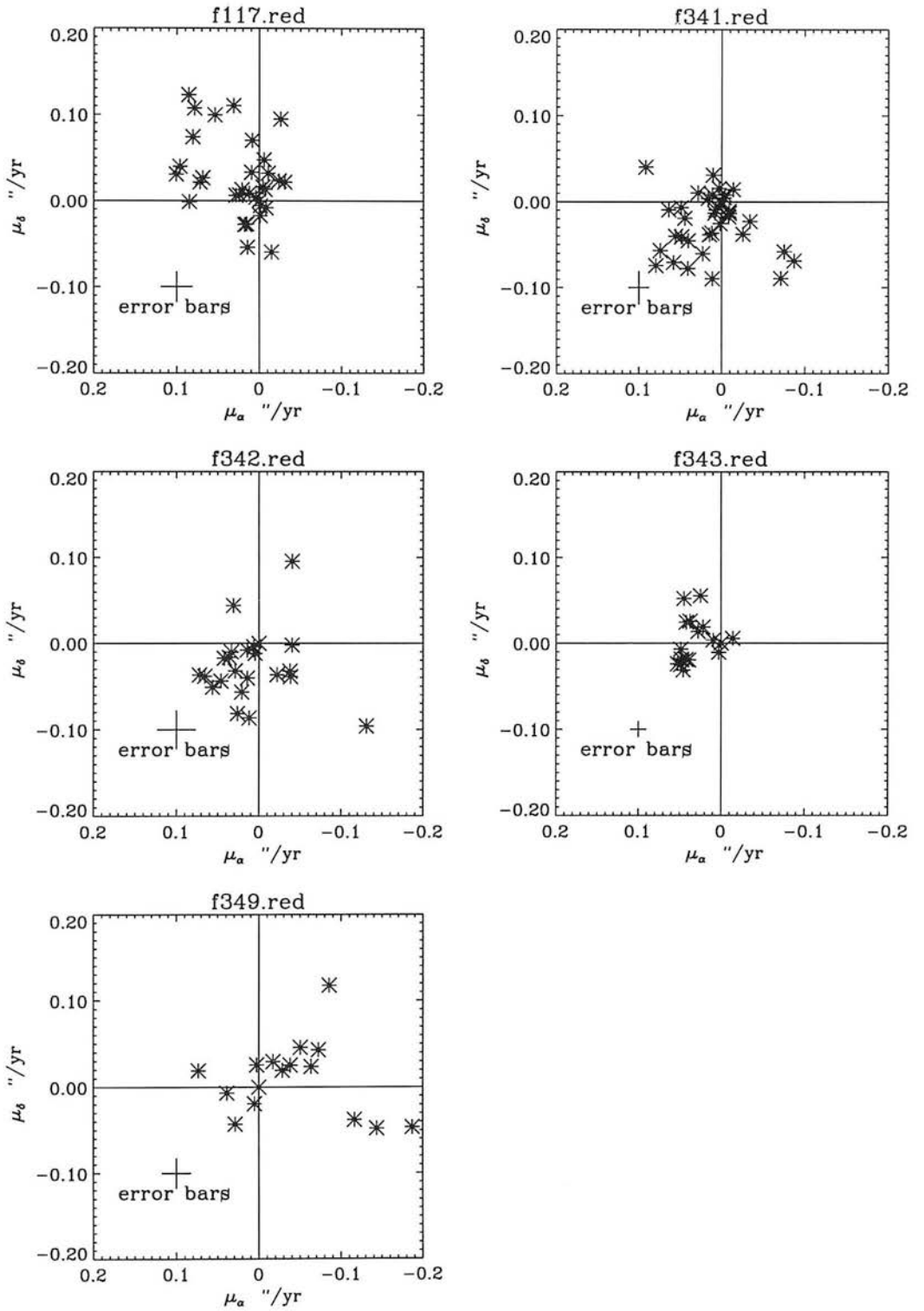

Figure 5.2: Proper motions of stars with R–I>2.0 that define the luminosity function within 100 pc.

5.1.3 Photometric colour and parallax.

In the absence of a distance measurement based on trigonometric parallax, a statistical estimate can be made using photometric colour indices. Figure 5.4 shows the population I M-dwarf sub-set of the Gliese catalogue. The relationship of absolute magnitude M_R to the photographic (R–I) colour index is shown. The baseline of the photographic colour is longer than that of the standard photoelectric system which gives the photographic system a small advantage. However, the bolometric corrections to the R–I index shown in figure 2.3 show an increasing divergence from R–I $\simeq$ 2 to 3 due to the 'saturation' of the index [2]. The uncertainty beyond this is so large as to render the relationship unusable for photometric parallax work. This does not rule-out the use of R–I$>$ 3 for the detection of cool stars however, but objects detected in this range will certainly need more accurate follow-up observations to determine their nature.

The scatter in the diagram is due to measurement errors, the natural cosmic variation in element abundance (metallicity) and variation in radius. Being related to age and stellar evolution, the second and third factors are not independent though the scatter due to variations in stellar radius is dominated by the other uncertainties. The size of cosmic scatter in this relationship is about 0.4 magnitudes. The size of the trigonometric parallax uncertainty is important, as a systematic bias is introduced in the absolute magnitude scale due to the geometric growth in distance with distance modulus.

The correction for this effect has been discussed by Lutz and Kelker, 1973 (LK73). Their approach is to assume that the stars defining the photometric parallax relationship are characterised by a Gaussian error distribution about the true parallax. For a uniform stellar distribution, the number of stars in the distance element r

[2]The (R-I) index is essentially measuring the variation of the TiO and VO bands with temperature. These bands are observed to saturate in dwarfs later than M6 with a corresponding loss in colour index sensitivity

to $r + dr$ is

$$N(r)dr = 4\pi r^2 dr. \tag{5.1}$$

In terms of the trigonometric parallax angle p the number is

$$N(p)dp = \frac{4\pi dp}{p^4}. \tag{5.2}$$

Thus for measurements distributed equally about p by $\pm dp$, the number count is biased towards the smaller values of p, yielding a mean magnitude for the range that is larger (more distant). LK73 define a dimensionless parallax $Z \equiv p/p_0$ and express the distribution of measurements p about the true value p_0 as

$$g(p|p_0) \propto G(Z) \equiv \frac{1}{Z^4} exp\left(-\frac{(p-p_0)^2}{2\sigma^2}\right) \tag{5.3}$$

where σ is the standard deviation of the measurements, such that $G(Z) = 1$ for $Z = 1$ regardless of the value σ/p_0. The magnitude correction ΔM is then given by

$$\Delta M = M_{\text{true}} - M_{\text{observed}} = 5 \log p/p_0 = 5 \log Z, \tag{5.4}$$

and the expectation value of the distribution is given by

$$\langle \Delta M \rangle = \frac{5 \int_0^\infty \log Z G(Z) dZ}{\int_0^\infty G(Z) dZ}. \tag{5.5}$$

To avoid the divergence of the terms as $Z \rightarrow 0$, LK73 evaluate the integrals numerically for a small lower limit ϵ, where $\epsilon \simeq 0.1$ and produce a table of values for σ/p_0 vs $\langle \Delta M \rangle$, which are plotted in figure 5.3. They find corrections are possible (*i.e.* the computation of equation 5.5 produces stable, physically sensible results) for $\sigma/p_0 < 0.15$. In order to use these results, a cubic polynomial has been fitted to the tabulated values and also plotted as a dashed line in figure 5.3. In applying these corrections to the chosen sub-set of the Gliese catalogue only objects with measurements satisfying $\sigma/p_0 < 0.1$ are used, ensuring that the

estimated corrections are no larger than $0^m.11$. The polynomial curve used has the form

$$\langle \Delta M \rangle = 7.57 \times 10^{-4} - 0.328(\sigma/p_0) - 1.073(\sigma/p_0)^2 - 63.03(\sigma/p_0)^3. \quad (5.6)$$

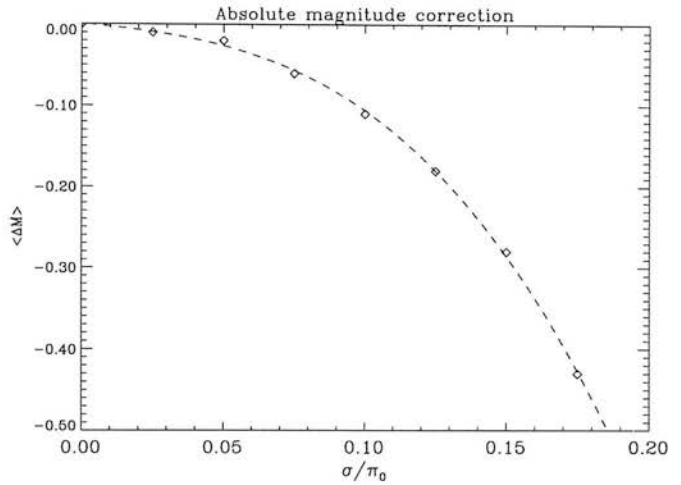

Figure 5.3: Correction of trigonometric bias to absolute magnitude, from computations by Lutz & Kelker 1973.

Despite the complexity of the relationships at higher temperatures (lower colour index) a linear fit is chosen to represent the measurements. The following relationships are derived, based on a sample of 103 stars, with the resulting absolute magnitudes being on the photographic system and the standard deviation being 0.6 mag. in each case.

$$M_{R_F} = 4.217 + 4.191(R_F - I_N), \quad (5.7)$$

$$M_I = 4.356 + 3.071(R_F - I_N) \quad (5.8)$$

The form of equation 5.7 is plotted in figure 5.4 as a solid line. The weighted fit produced by the set prior to correction by the method described above is plotted as a dashed line. The difference is insignificant, due to the restrictions imposed on selecting stars for the fit.

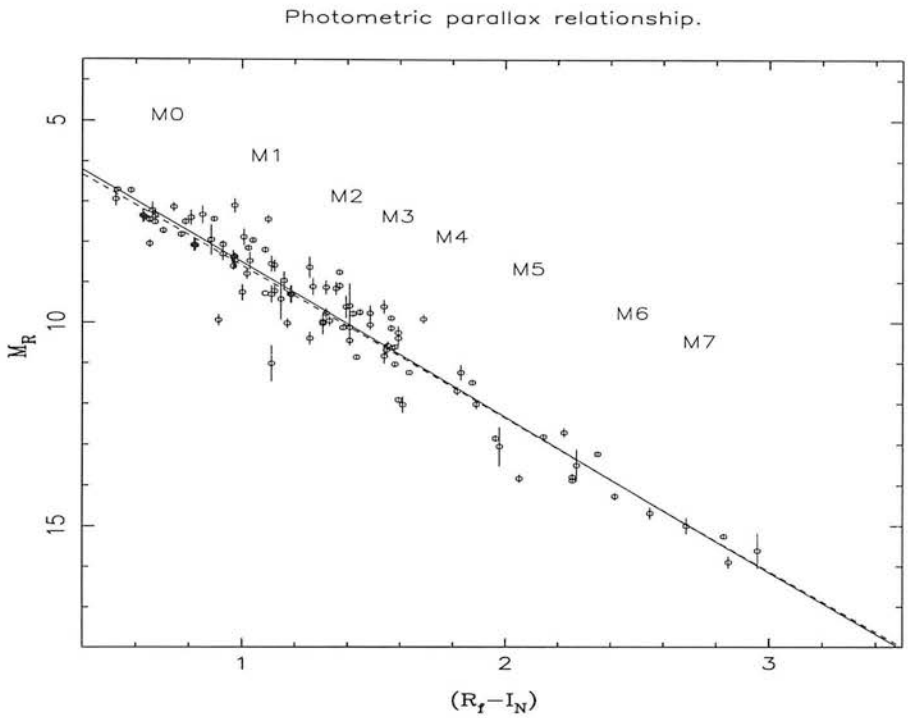

Figure 5.4: Colour-magnitude relationship for cool stars with approximate spectral class and linear least squares fits before (dashed line) and after (solid line) correction for trigonometric parallax bias.

5.1.4 Calculating the space density

Having estimated the luminosity of each star using the distance/magnitude relationship, the luminosity function is constructed by binning the stars by absolute magnitude and ensuring that the sample is complete (100% of the stars in the field are accounted for) within a specific volume. This volume is determined by the limiting observable distance of the least luminous star in the sample, which in turn is determined by the flux limit of the detector. In a survey whose intention is to discover stars with the lowest possible luminosity this is a great restriction, since it reduces the survey volume to a very small region in the solar neighbourhood and forces the rejection of otherwise useful measurements of more distant (more luminous) stars.

An estimate of the luminosity function of a *magnitude-limited* survey can be calcu-

lated using a method described by Schmidt (1975) that come to be known as the 'V_{max}' method. As mentioned briefly in Chapter 2, this method treats each object within the survey limit as an individual sampling of the luminosity function. For each sample member j a value $V_{m,j}$ is calculated which represents the maximum volume that the object could contribute to the survey and still be detected. This can be defined in terms of the maximum distance $r_{m,j}$ at which the object is still within the survey's flux limit i.e.

$$V_{m,j} = \frac{\Omega}{4\pi}\frac{4}{3}\pi {r_{m,j}}^3 \tag{5.9}$$

Where Ω is the survey solid angle and $r_{m,j}$ is assumed to be independent of direction on the sky and randomly distributed (see Felten 1976 for discussion of this and other cases). The case considered here also assumes a locally flat (Euclidean) space with distances on a intra-galactic scale and thus unaffected by cosmological evolution (unlike Schmidt's original application). With this definition, the luminosity function for the N members in a given magnitude bin is given by

$$\phi = \sum_{j=1}^{N} \frac{1}{V_{m,j}}. \tag{5.10}$$

with variance

$$var\phi = \sum_{j=1}^{N} \frac{1}{V_{m,j}^2}, \tag{5.11}$$

i.e. Poissonian ($\sqrt{N}$) error bars.

The above method is suitable for isotropically distributed objects, but for disc stars the fall-off in density with disc height must be considered, in the form of a generalised volume

$$V_{gen} = \Omega \int z^2 \rho/\rho_0 dz. \tag{5.12}$$

For the standard density function $\rho/\rho_0 = e^{-z/H_z}$, integration by parts gives

$$V_{gen} = \Omega {H_z}^3[2 - (y^2 + 2y + 2)e^{-y}], \tag{5.13}$$

where $y = z/H_z$. Stobie *et al.* use this method for their Galactic pole survey. To further generalise this to any Galactic latitude b, the exponent term becomes y=$(r \sin b)/H_z$ and the generalised volume term becomes

$$V_{gen} = \Omega \frac{{H_z}^3}{\sin^3 b}[2 - (y^2 + 2y + 2)e^{-y}], \tag{5.14}$$

as used by Tinney *et al.* (1992).

5.1.5 Accounting for photometric bias

As noted, the absolute magnitude-colour relations used to derive stellar distances have a natural scatter of around 0.3 to 0.5 mag. (depending on waveband). This leads to a bias in the volume sampling of a luminosity function that is usually known as *Malmquist bias* (Malmquist 1927). For stars of equal apparent magnitude in a given colour range, the mean absolute magnitude, M_m of stars in that bin is increased. This effect is due to the logarithmic nature of the distance-magnitude relation and was discussed in the previous section with respect to the photometric distance relationship. The effect here is due to the *cosmic* scatter as opposed to the *instrumental* scatter discussed above, but the effect is the same: a larger over-estimate of distance for an over-luminous object of magnitude $M + \delta M$ than the under-estimated distance for a star of $M - \delta M$. The over-estimate of the mean magnitude is the result of working with a magnitude-limited (or *flux-limited*) sample and can be corrected to the 'true' mean, M_0 as would be determined from a volume-limited sample by applying the following correction to each star in the sample:

$$\Delta M = M_m - M_0 = -\sigma^2 \frac{1}{N} \frac{dN}{dm}. \tag{5.15}$$

Here σ is the (Gaussian) cosmic scatter and $\frac{dN}{dm}$ the differential number counts (for M). Stobie *et al.* (1989) have pointed-out that the effect of the bias is two-fold: firstly, the mean is biased, as discussed above and secondly, the number of images outside of the survey volume that are scattered into a bin increases geometrically with apparent m, biasing the calculated number density. This effect is different to that of the sampling of stars of magnitude m already within the survey volume to larger volumes, which is dealt with in equation 5.15.

The result of this effect is contained in an extra correction term that must be applied to the data. The correction is applied to the luminosity function itself and not to the individual objects in the sample. The fractional change in the luminosity function according to Stobie *et al.* is

$$\Delta\phi/\phi = \frac{1}{2}\sigma^2[(0.6\ln 10)^2 - 1.2\ln 10\phi'/\phi + \phi''/\phi], \tag{5.16}$$

where σ is the standard deviation of the colour-magnitude relationship (the cosmic scatter) and ϕ' and ϕ'' are the first and second derivatives of the luminosity function with respect to absolute magnitude. Application of this correction thus requires differentiation of the luminosity function which is done here by use of a Lagrangian difference method (see Kopal p. 87-92 for example).

5.1.6 The photographic luminosity function of low mass stars

The luminosity function for dwarf stars with absolute magnitude $M_{R_F} > 10.0$ is presented here. The sample is taken from five survey fields: 117, 341, 342, 343 and 349, the middle three of which are contiguous on the sky. Stars have been selected according to the criteria discussed above with the further stipulation of a distance limit of 100 pc and a magnitude limit of R = 19.0. The distance limit serves two purposes: to minimise to effects of inter-stellar reddening of the objects, which will bias the function towards cooler stars and to reduce the effects of the fall in the stellar density function with distance from the disc. This second effect has been partially dealt with by the use of a generalised sampling volume, but this function is

scale-height dependent and thus introduces a bias into the sample which increases exponentially with distance from the plane. Considering two possible values of the old disc dwarf scale height; 300 pc and 350 pc, the difference in sampled density at 100 pc is no more than 5% and this value decreases with $|b_{gal}|$.

The tabulated luminosity function for each field is given in tables 5.1 to 5.5. The combined function is given in table 5.6 in which the number of objects per bin in each field is listed again in columns two to six.

Table 5.1: Stellar luminosity function for field 117.

$M_R \pm 0.5$	Objects	ϕ mag^{-1}pc^{-3}x10^3	$\log \phi$
10.5	14	7.41	-2.13
11.5	19	10.05	-1.99
12.5	41	21.69	-1.66
13.5	12	8.82	-1.05
14.5	1	3.90	-1.41
15.5	0	0.0	-
16.5	0	0.0	-

Table 5.2: Stellar luminosity function for field 341.

$M_R \pm 0.5$	Objects	ϕ mag^{-1}pc^{-3}x10^3	$\log \phi$
10.5	41	19.56	-1.71
11.5	46	21.95	-1.65
12.5	29	13.84	-1.86
13.5	13	8.45	-2.07
14.5	9	16.19	-1.79
15.5	1	3.54	-2.45
16.5	1	13.75	-2.86

Table 5.3: Stellar luminosity function for field 342.

$M_R \pm 0.5$	Objects	ϕ mag^{-1}pc^{-3}x10^3	$\log \phi$
10.5	27	14.43	-1.84
11.5	30	15.89	-1.80
12.5	20	10.59	-1.97
13.5	9	6.26	-2.20
14.5	1	1.03	-2.99
15.5	0	0.0	-
16.5	0	0.0	-

Table 5.4: Stellar luminosity function for field 343.

$M_R \pm 0.5$	Objects	ϕ mag^{-1}pc^{-3}x10^3	$\log \phi$
10.5	24	12.27	-1.95
11.5	32	16.35	-1.75
12.5	18	9.20	-1.89
13.5	6	4.96	-2.00
14.5	1	1.05	-2.97
15.5	1	3.75	-1.69
16.5	0	0.0	-

Table 5.5: Stellar luminosity function for field 349.

$M_R \pm 0.5$	Number	ϕ mag^{-1}pc^{-3}x10^3	$\log \phi$
10.5	11	5.83	-2.23
11.5	24	12.73	-1.90
12.5	31	16.44	-1.78
13.5	9	5.74	-2.24
14.5	6	14.44	-1.84
15.5	2	18.36	-1.74
16.5	0	0.0	-

Table 5.6: Combined Stellar luminosity function for fields 117, 341, 342, 343 and 349.

M_R ± 0.5	#117	#341	#342	#343	#349	#total	$\phi(M_R)$ $\mathrm{mag}^{-1}\mathrm{pc}^{-3}\mathrm{x}10^3$	$\log \phi$
10.5	14	41	27	24	11	117	11.90	-1.92
11.5	19	46	30	32	24	151	15.44	-1.81
12.5	41	29	20	18	31	139	14.39	-1.84
13.5	12	13	9	6	9	49	6.86	-2.16
14.5	1	9	1	1	6	18	8.02	-2.09
15.5	0	1	0	1	2	4	5.20	-2.28
16.5	0	1	0	0	0	1	2.87	-2.54

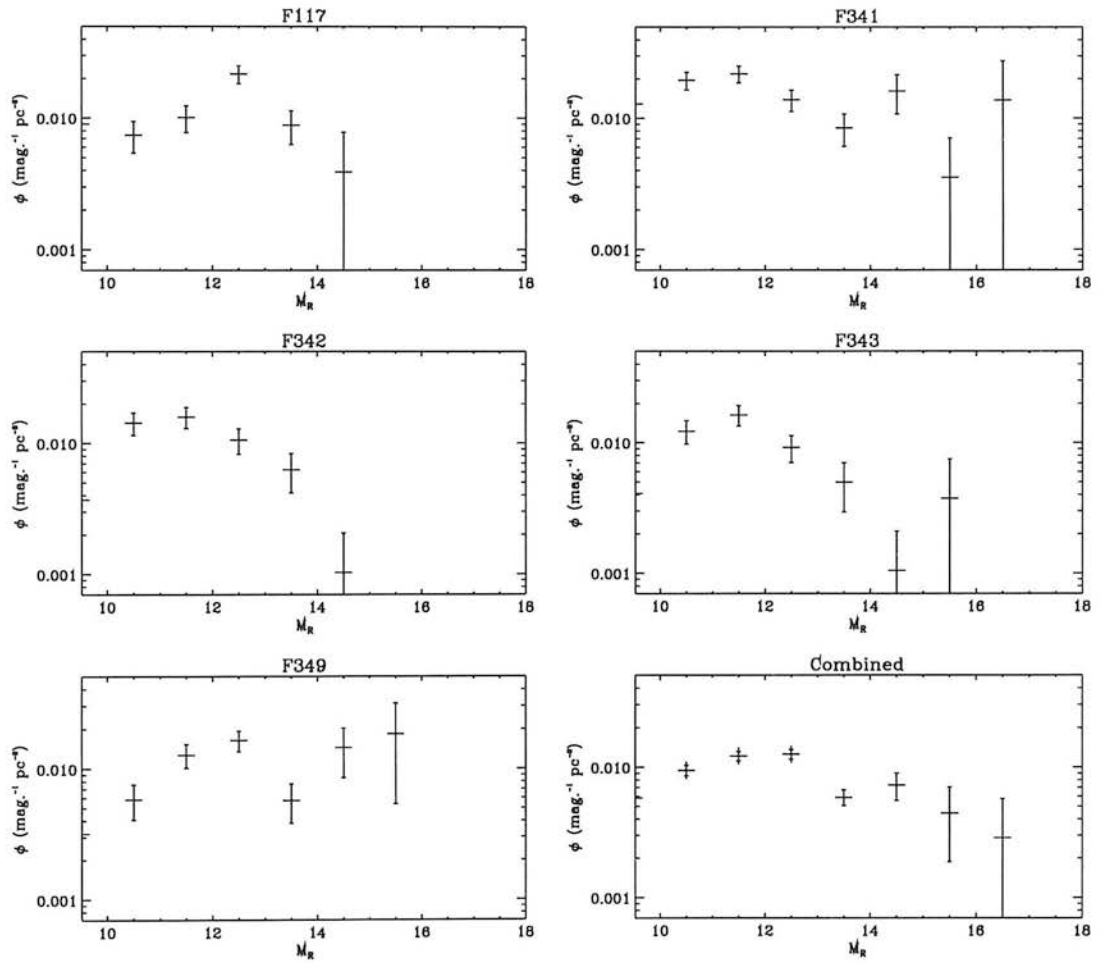

Figure 5.5: The RG630/IIIaF band (R_F) luminosity function of dM-type stars within 100 pc of the Sun with R < 19.0. Five individual fields are shown plus the combined function at lower right. The total sky coverage is 111.7 deg^2

Table 5.7: Raw and corrected luminosity functions in R_F and bolometric wavebands. Values are logarithmic, expressed in $mag^{-1}pc^{-3}$

Bin	$\log\phi(M_R)$		$\log\phi(M_{bol})$	
± 0.5	raw	cor.	raw	cor.
8.5	-	-	-1.6	-1.73
9.5	-2.20	-2.36	-1.32	-1.49
10.5	-1.92	-2.07	-1.95	-2.14
11.5	-1.81	-1.98	-2.12	-2.33
12.5	-1.84	-2.02	-2.51	-2.61
13.5	-2.16	-2.35	-2.53	-2.54
14.5	-2.09	-2.29	-	-
15.5	-2.28	-2.38	-	-
16.5	-2.54	-2.55	-	-

The derived function can be put into context by comparison with previous determinations. The Hawkins & Bessell (1988) LF is given in the same waveband as the one above and so a direct comparison can be made. The R–I bolometric correction given by equation 2.1 is used to transform the data of this work to the bolometric system which allows comparison with several other surveys. The Tinney *et al.* (1993) LF is given for a different R band and conversion between the two will introduce a considerable uncertainty. They also present a bolometric LF which the LF of this survey is compared to in figure 5.7. Reid (1987) has also transformed the HB88 LF onto the bolometric system which is also compared, as is the Kirkpatrick *et al.* (1994) CCD survey. The raw and bias-corrected luminosity functions in each waveband for this work are given in table 5.7. The effect of the bias correction is the shift the function to lower space densities and brighter magnitudes.

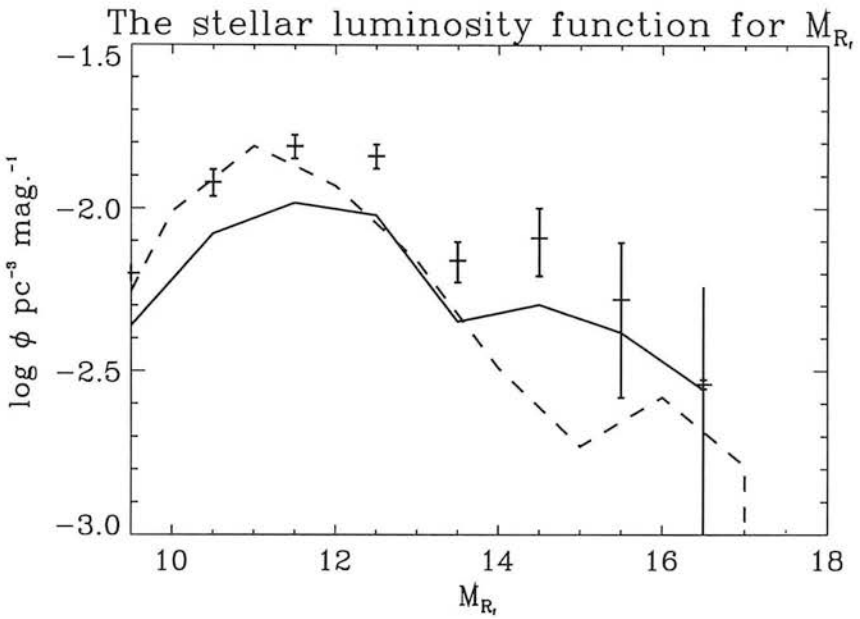

Figure 5.6: The R band stellar luminosity function. Error bars mark the raw data, the solid line shows the Malmquist bias-corrected function. Dashed line is the LF of Hawkins & Bessell 1988 on the same photometric system, with no bias correction applied.

The luminosity function presented here is in fair agreement with previous measurements. The most obvious features being the peak around $M_R = 11$ and the subsequent decline. For the M_R function there is some disagreement with the HB88 function for the faintest bins, where they measure smaller space densities. The LF presented here does not extend to the $M_R = 17$ bin as the HB88 does and the sampling of their survey is better due to the higher magnitude limit ($R = 20$). The excess in the $M_R = 14$ and 15 bins with respect to HB88 is notable. In numbers this is 22 objects, the majority coming from fields 341 and 349. Were this excess to be removed, the functions would be in better agreement. This excess does not however contribute to any evidence that the function is rising again towards the faintest bins. The excess counts may be genuine or due to contamination, a possible candidate for which is photometric scatter from adjacent bins. Field 349 was noted for having a small group of objects with unusual proper motions that suggested possible contamination of the sample. The high proper motion objects in this field *do* contribute to this bin and are a likely source of contamination. Fur-

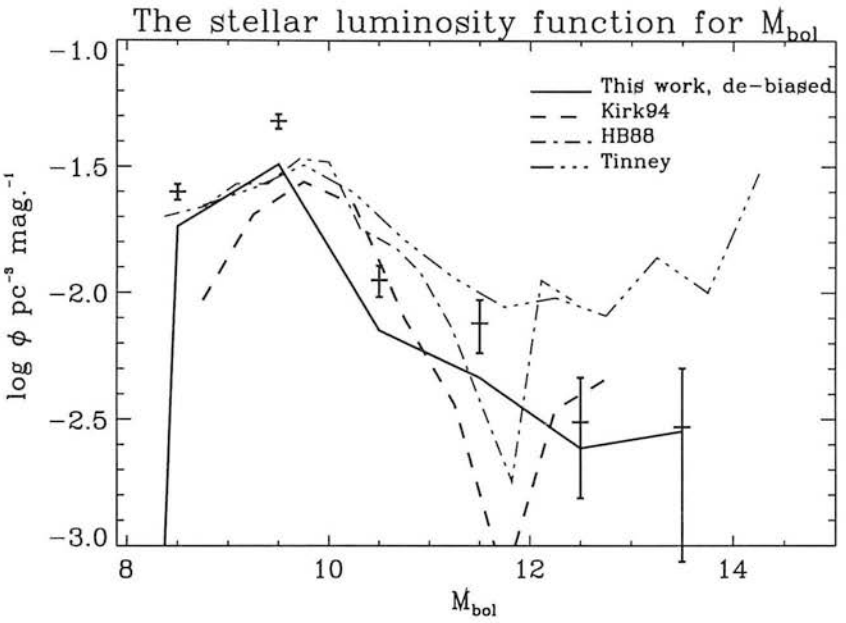

Figure 5.7: The stellar luminosity function for M_{bol}. Error bars mark the raw data, the solid line shows the Malmquist bias-corrected function. Dashed line is the LF of Kirkpatrick *et al.* 1994, dot-dashed is that of Hawkins & Bessell 1988 and dot-dot-dash is that of Tinney 1993.

ther observations are required to identify these objects since local excesses would suggest variation of the nearby stellar LF with field location, which goes against the prevailing evidence. All objects in the M_R = 14, 15 and 16 bins are listed, with coordinates in table 5.8.

The bolometric luminosity function is in general agreement and supports a lower space density for the faintest objects as opposed to the generally higher space densities and rising function as measured by Tinney (1993). Again it should be noted that the statistical significance of this sample is weaker than that of its peers due to the low number counts and imposed flux limit. The bolometric function does not show the excess counts noted in the R band LF to the same extent. The rebining and the uncertainty in the bolometric correction appear to have smoothed this feature.

Having presented a new measurement of the stellar luminosity function and having

shown that it is in broad agreement with several more extensive measurements it is worth addressing the question "*what new information does this new measurement give us?*". The answer is that this survey has been conducted with a data set that is very typical of what is available in the UKST plate archive. The Hawkins & Bessell survey studied fields with relatively large numbers of plates (fields 287 and the south Galactic polar fields), used more extensive photometry and achieved a depth one magnitude fainter than this survey. The Tinney survey used more typical plate material but again used an extensive set of photometric sequences in each field. Despite these advantages the number of very low mass stars detected in these surveys is small: two in the HB88 survey and around ten in the Tinney survey. The important region of the luminosity function for such work begins in the sixteenth bin where most objects are close to or beyond the photographic flux limit. It seems clear that statistically useful work (*i.e.* detecting lots of very low mass stars) can only be achieved in photographic surveys by casting the net over a very large area of the sky. The plate material that future large-area surveys will have to use is of the standard of that used in this survey. This work shows that reasonable results *can* be obtained from such material.

Table 5.8: Stars with $M_R > 14.0$ detected in the 112 deg^2 survey.

α_{1950} h m s	δ_{1950} ° ' "	R_f (σ_R)	R - I (σ_{R-I})	M_R	μ_α (σ_μ) mas/yr	μ_δ (σ_μ) mas/yr
03 40 11.11	−58 17 41.2	17.10 (0.06)	2.36 (0.08)	14.13	14.36 (18.92)	−54.09 (17.24)
00 01 17.52	−34 18 13.9	18.37 (0.04)	2.36 (0.15)	14.09	−28.39 (17.15)	+19.56 (17.6)
00 05 10.76	−36 56 43.9	18.68 (0.12)	2.54 (0.14)	14.90	-18.81 (16.73)	−58.62 (17.17)
00 05 11.78	−35 37 14.4	18.51 (0.12)	2.43 (0.22)	14.42	35.47 (17.48)	−48.29 (18.31)
00 05 18.82	−34 42 58.2	17.62 (0.06)	2.45 (0.07)	14.51	+85.43 (16.43)	+117.5 (18.15)
00 06 57.68	−34 39 30.3	17.01 (0.10)	2.42 (0.18)	14.35	38.80 (19.31)	−68.28 (19.40)
20 44 04.02	−39 25 36.1	17.12 (0.07)	2.50 (0.22)	14.71	−71.13 (10.49)	−89.23 (10.34)
20 46 03.55	−40 54 31.1	18.99 (0.11)	2.43 (0.24)	14.41	−13.96 (10.85)	+14.37 (10.44)
20 47 29.09	−40 16 49.1	18.54 (0.070	2.49 (0.17)	14.68	28.53 (10.44)	+10.39 (9.83)
20 49 56.44	−40 22 16.3	18.19 (0.09)	2.39 (0.19)	14.24	8.15 (10.14)	−13.35 (9.83)
20 53 33.29	−41 16 03.8	18.33 (0.07)	2.48 (0.30)	14.62	40.66 (9.73)	−45.45 (9.07)
20 54 22.70	−41 14 08.8	17.42 (0.05)	2.46 (0.18)	14.54	11.72 (11.51)	−36.48 (11.31)
20 57 42.40	−40 46 34.2	18.72 (0.13)	2.55 (0.33)	14.92	10.29 (10.54)	+31.18 (9.88)
20 58 08.78	−40 31 41.4	17.89 (0.05)	2.56 (0.20)	14.95	−9.27 (10.49)	−13.65 (9.73)
20 58 49.55	−39 43 07.3	16.75 (0.13)	2.39 (0.35)	14.26	73.99 (9.7)	−56.87 (9.2)
21 22 25.76	−39 22 04.5	18.99 (0.01)	2.44 (0.12)	14.44	28.88 (21.45)	−32.07 (21.45)
21 45 43.18	−40 01 09.3	17.32 (0.14)	2.37 (0.45)	14.15	45.85 (14.40)	−31.27 (10.62)
23 53 44.29	−35 30 52.5	17.78 (0.02)	2.34 (0.13)	14.02	53.29 (17.48)	−19.31 (16.82)
00 03 44.50	−35 06 00.4	18.55 (0.12)	2.67 (0.14)	15.41	−187.02 (19.31)	−46.63 (19.40)
00 00 11.07	−36 09 40.1	17.08 (0.14)	2.58 (0.18)	15.04	−197.34 (16.15)	+223.49 (16.15)
20 57 34.57	−41 18 32.7	18.95 (0.06)	2.79 (0.47)	15.92	16.20 (10.95)	+38.72 (10.91)
21 32 57.47	−40 21 32.0	18.31 (0.15)	2.59 (0.50)	15.05	39.23 (7.62)	−19.70 (7.06)
20 49 24.38	−40 19 54.2	18.92 (0.07)	2.97 (0.27)	16.68	55.54 (10.14)	−40.26 (10.14)

5.2 Red object survey candidates

The following objects listed in this section have been selected from the survey for further attention. They are listed in table Table 5.9, being those images selected from the original COSMOS measurements prior to the acquisition of SUPERCOSMOS data. Each candidate object is assigned a name composed of the SERC survey field number and a letter obtained by listing the candidates in each field in order of increasing right ascension. Celestial co-ordinates are based on the COSMOS measurement of the primary plate of each set, and are quoted in the B1950 system as given in the original IAM data. The photometric measurements are based upon the most recent magnitude calibration involving both COSMOS and SUPERCOSMOS data, which replaces the values used to select the original sample. Several of the original objects been rejected as a result of the recalibration and all lie beyond the magnitude limit of the luminosity function survey except for 341A, 341B, 342A and 349H.

5.3 Follow-up observations: *The Lithium Test*

COSMOS -measurable properties are insufficient for individual star/brown dwarf discrimination in all but the most extreme cases. The crucial factor is mass which can only be realistically measured in nearby binary systems. The next most important parameter is age: knowing the age of each star in a sample is the only way to extract the initial luminosity and mass functions from the observed distribution.

Age can be measured, or at least correlated with kinematic and spectroscopic properties. The kinematic relationship, that of increasing velocity dispersion with age has already been discussed in Chapter 3. This method requires a large sample of objects in each age group in order to measure significant differences in space motion. Furthermore measurement of space velocity requires a distance measurement for each object. The acquisition of trigonometric parallaxes adds greatly to the amount of time and resources involved in any follow-up programme. Photo-

Table 5.9: Red object candidate list from a survey of six SERC survey fields.

Name	R.A. (B1950)	Decl. (B1950)	I	R-I
117A	3 41 43.3	−57 49 40.0	17.34	2.41
117B	3 49 57.8	−59 05 42.3	16.85	2.85
117C	3 51 00.1	−59 52 59.0	16.84	2.63
117D	4 01 28.9	−60 10 53.0	16.87	3.05
296A	1 22 36.0	−37 00 16.1	14.57	2.54
296B	1 24 40.8	−39 36 44.2	17.93	2.34
297A	1 39 33.8	−42 20 27.5	16.40	2.66
297B	1 39 55.1	−39 25 38.6	15.14	3.03
297C	1 42 21.9	−39 52 21.9	16.02	2.32
297D	1 48 03.7	−38 54 40.3	16.50	2.40
341A	20 47 29.1	−40 16 49.1	16.05	2.49
341B	20 50 03.8	−40 02 43.5	15.84	2.14
341D	20 59 24.8	−39 16 51.0	16.61	2.57
342A	21 03 06.9	−40 56 54.0	15.15	2.21
342C	21 22 07.3	−38 33 06.4	16.07	2.44
342E	21 23 42.0	−39 27 51.0	16.43	2.42
343A	21 48 39.2	−40 46 30.3	16.29	2.64
343B	21 48 43.4	−42 24 47.9	17.13	2.61
349B	00 09 54.9	−33 48 45.3	16.69	2.57
349C	00 10 04.0	−34 13 04.3	17.08	2.70
349E	23 48 15.2	−34 29 24.5	16.24	2.73
349H	23 58 55.6	−33 16 06.7	16.69	2.22

metric parallaxes can be used though the uncertainty is usually much larger (see §5.1.2). Radial velocity and proper motion measurements must also be made. Proper motions can be made with the existing plate material, radial velocities require spectroscopic measurements.

Spectroscopic indicators of age have the advantage of being specific to each star: a group property is not required although in some cases the relationship may be a statistical correlation. Three types of age-related features can be measured: those related to light element abundance and nuclear depletion, those related to 'youthful activity' where abnormal atmospheric features are excited and those sensitive to atmospheric pressure, allowing measurement of surface gravity which is related to age via the stellar radius.

The following section presents observations of COSMOS selected candidates with the intention of detecting the presence of the Lithium I resonance doublet at 670.8 nm. Measuring the level of nuclear depletion of lithium via this absorption feature in fully convective stars is a standard technique in the study of T Tauri stars. The lower temperature limit for lithium burning is close to that of the predicted central temperatures of high mass brown dwarfs which makes measurement of the feature a potential star/brown dwarf discriminator. This measurement has been dubbed "*The Lithium Test*" by Rebolo *et al.* (1992) and in the absence of a mass measurement, 'passing the test' is regarded by some as the strongest confirmation of an object's sub-stellar nature. Without a luminosity measurement, implying a distance measurement, the value of the test is lessened and secondary measurements must be made to constrain the age of the candidate. Temperature evolution is chosen for this work and the far-red spectroscopy required is presented below.

5.3.1 Light element abundance and The Lithium Test

The light metals Deuterium, Lithium, Beryllium and Boron are believed to have been synthesised during the first few minutes of the Universe. The cosmic abun-

dance of these elements has decreased ever since through depletion by further nucleosynthesis of heavier elements in stellar interiors. These elements are involved in the three principal proton-proton chain reactions of stellar fusion: PPI (D), PPII (Li and Be) and PPIII (Be and B). The importance of these reactions is that their rates are most sensitive to temperatures in the range $1 - 4 \times 10^6$K, below that of the main energy-providing steps of proton fusion which require temperatures in excess of 5×10^6K. Because the elements are so rare compared to hydrogen (by a factor 10^{-9} there is potential for these elements to be fully depleted in some predictable timescale, which can be used a measure of age. Since brown dwarf stars are predicted to achieve maximum core temperatures within or below the critical fusion range quoted above, the presence of these light elements in a star can be used a star/brown dwarf discriminant.

Several authors (Pozio 1991, Pavlekno *et al.* 1994 and Nelson *et al.* 1993b) have modelled the physical conditions and found that light elements are depleted very rapidly (in less than 10^8 years) once fusion begins. The depletion rate, being strongly temperature-dependent is related to mass. Thus the presence of the element in a star of a given mass tells us that the star is younger than the depletion age. More usefully, if age limits can be placed on the star from effective temperature or luminosity evolution, then the presence of the element places limits on the star's mass.

The discussion above assumes that material in the stellar core is visible to the observer. This is only possible in main sequence or pre-MS stars if the internal convection zone extends into the core. In this case core material can be dredged into the atmosphere to produce absorption features which are potentially observable. This degree of convection occurs in stars of masses around $0.3M_\odot$ and below which includes brown dwarfs and the sub-set of low mass stars that they share a common appearance with during the era of light element burning.

Cool stellar atmospheres, as discussed in chapter 2 present the largest problem to the physical modeller and so give the least reliable of predictions from a stellar

model. Prediction of line strengths and profiles of light elements are dogged by both the influence of the stronger metal oxide features and by uncertainties in the convection and mixing processes within the star. The element lithium has been singled-out as the most potentially useful to the observer due to the predictions of relatively strong atomic lines in the visible spectrum (specifically 610.3nm, 670.8nm and 812.6nm). In fact, the 670.8nm line is well known to observers of T-Tauri type stars; pre-main sequence stars, usually of spectral type K or M with ages of order one to ten million years. Stars as young as this have not yet depleted their supply of lithium and the 670.8nm absorption feature is visible, typically with an equivalent width of around 0.05nm (usually quoted as 0.5Å).

In a large T-Tauri survey by García-López *et al.* (1994) and Martín e*et al.* (1994) the largest measured equivalent widths are less than 0.8Å, even for stars of estimated ages below one megayear. These measurements can be compared with the theorists predictions. Growth curves from Pavlenko *et al.* (1994) for example predict values of 0.3Å for 3000K dwarfs of solar metallicity. The lines widen with decreasing temperature such that a 2500K star of solar metallicity would show an equivalent width of around 0.6Å. For stars of higher metallicity, such as a T-Tauri would have, the 3000K and 2500K cases give widths of 0.9Å to 3.0Å, for log n(Li) = 2.0. So whilst the predictions for higher mass, higher temperature stars of solar luminosity are in fair agreement, the case for lower mass, younger objects such as dM class T Tauris and presumably brown dwarfs (with even cooler, more complex atmospheres) is less clear. The observational evidence suggests that the predictions may over-estimate line widths by a factor of five or so. With this in mind, the observational programme was designed to detect equivalent widths below 0.5Å.

The observational basis for the test has been developed recently by surveys of a number of cluster and field brown dwarf candidates. These include Magazzú *et al.* 1991, Rebolo *et al.* 1992, Martín *et al.* 1994, and Reid *et al.* 1994 none of which succeeded in detecting a lithium-bearing brown dwarf candidate but have helped to weed-out several long-standing candidates from the list of possible brown dwarfs. Very recently two successful results have been reported by Basri *et al.*

1996 and Rebolo *et al.* 1996, both of which have measured the line in Pleiades BD candidates. The Basri *et al.* paper reports the detection in the object PPL 15 (Stauffer *et al.* 1994) with a measured equivalent width of approximately 0.5Å and thus similar to the T Tauri measurements. The star appears to mark the main sequence/brown dwarf divide, and the Rebolo *et al.* report adds weight to this by presenting spectra of two objects of lower luminosity than PPL 15 (Teide 1 and Calar 3) with measured equivalent widths of 1.0 ± 0.2 and 1.8 ± 0.4 which are closer to the model atmosphere predictions discussed above. The case for the brown dwarf nature of these objects is very strong and is an encouraging sign for the future application of the lithium test.

The observations for this programme were carried-out between 1995 August 19 and 21 using the Anglo Australian Telescope at Siding Spring, New South Wales, Australia. The RGO spectrograph was used with the 1200R grating which provided a resolution of 0.54Å per channel, sufficient to detect the Li line in T Tauri stars, as discussed above. The Tek CCD gave a range of 6540 to 7080Å. Further observations of the candidate objects were made with the same instrument using the 270R grating to measure far red spectra with a resolution of 3.4Å per channel in the 5670 to 9150Å range. The purpose of these measurements was to provide an estimate of the spectral class and effective temperature of the candidate objects. This spectral range contains several features which allow sub-dwarf/dwarf/giant discrimination.

Thirty minute integrations were used with the 1200R grating to obtain spectra of the Li region, and 10 minute integrations for the 270R measurements. The T Tauri star Sz 81 was measured to provide a comparative Li spectrum and the M7 dwarf VB 8 (LHS 644C) and M8 dwarf VB 10 (GL 752B) were also observed. Eight candidates were observed this way and the resulting spectra are shown in figures 5.8 and 5.9. Candidates 297A, 341C, 342B, 342D, 342E, 343C, 349A and 349D were also observed but poor weather rendered the spectra unusable. Sz 81 is plotted in each figure and the solid vertical line marks the position of the expected absorption line at 6707.8Å.

Figure 5.8: Li I

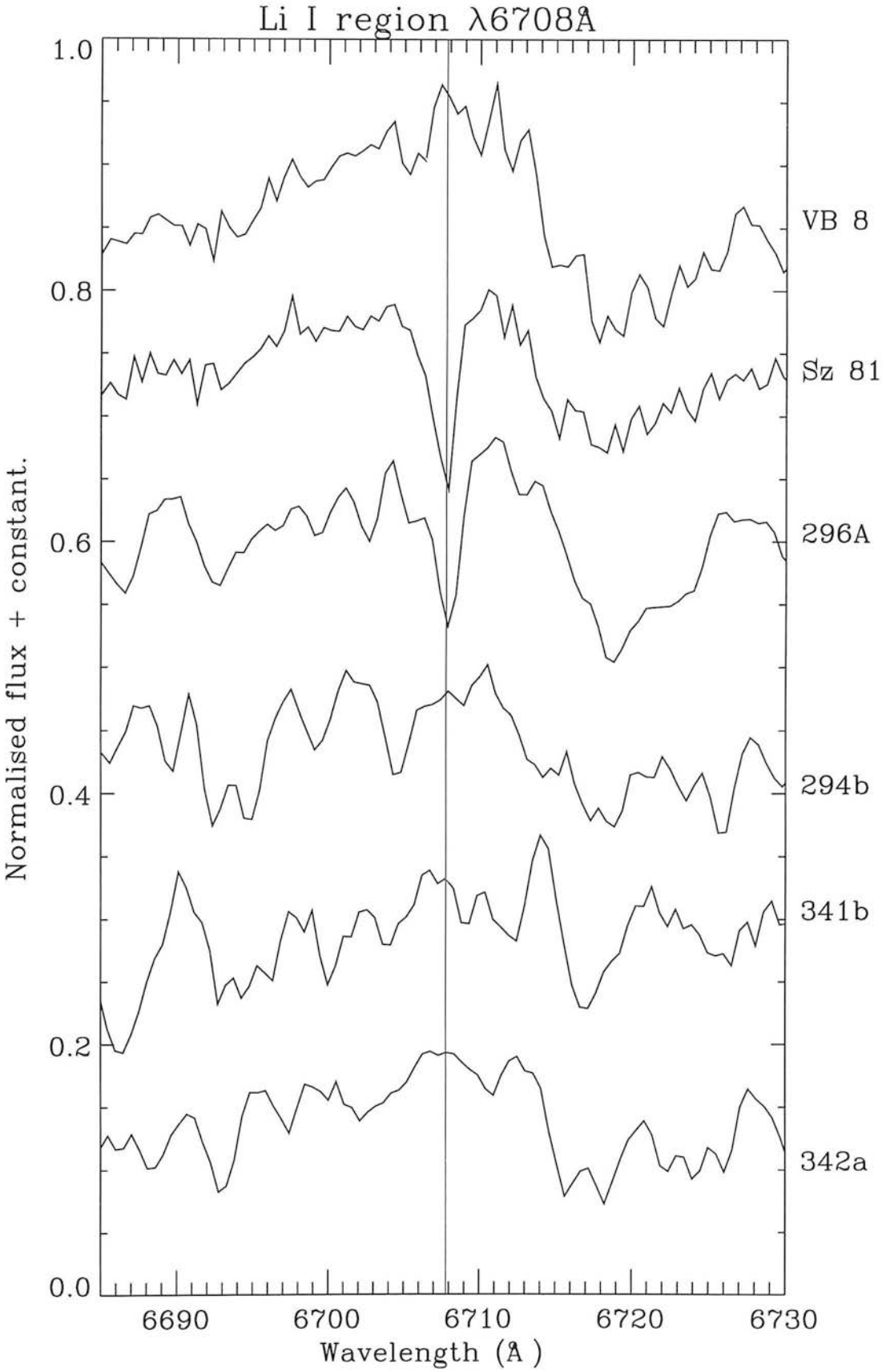

Figure 5.9: Li I

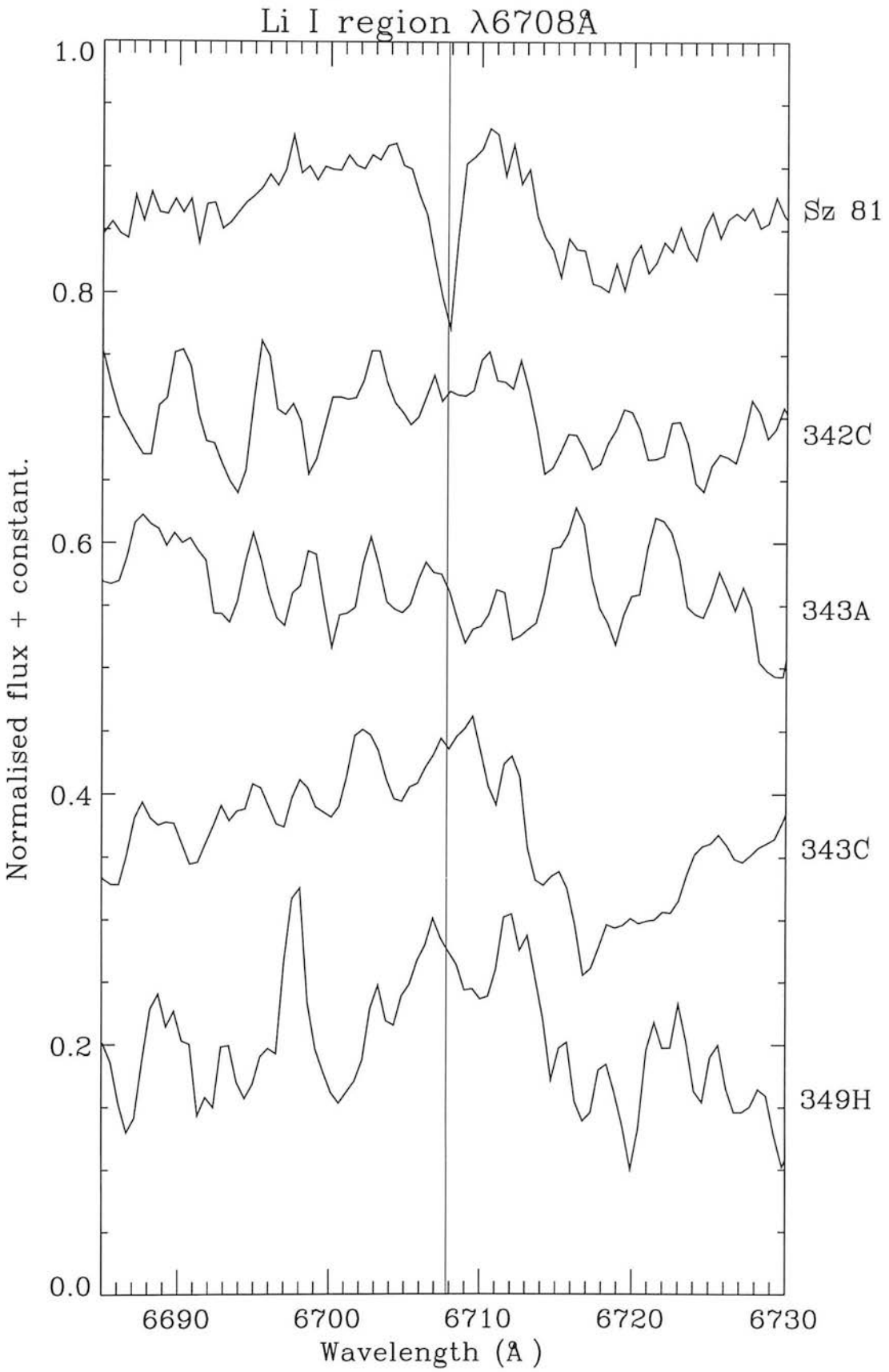

As is clear from the above spectra, only one of the observed candidates shows any evidence of bearing the Li line: 296A. The spectra of 342C and 343A are inconclusive due to lack of signal. The remaining five objects show similar M dwarf absorption features as defined by the VB 8 spectrum. The TiO line around 6705Å is clearly blended with the Li feature in 296A and is visible in VB 8. To assess the implications of this detection, a stellar structure model that treats lithium depletion is required.

5.3.2 Interpretation of the 296A Lithium measurement

The lithium test is employed as a means of discriminating between low mass stars and brown dwarfs. The fundamental difference between these types of object is their mass, which is either above or below the minimum required for stable hydrogen burning. The presence of lithium is not directly related to mass, but to age since it is the extent of depletion of the element in the star that determines whether it can be observed or not. Thus, the presence of lithium sets an upper limit to the age of an object, this limit being the latest epoch at which lithium is present in the stellar atmosphere. The rate of lithium depletion is a function of mass and so the 100% depletion epoch is also a function of mass. The interpretation of the detection requires a detailed model of lithium depletion for a range of masses and the stellar models of Nelson *et al.* 1993 provide this as do the more recent models of D'Antona & Mazzitelli (1994) and Chabrier *et al.* (1996). With no further limits, the models give a range of possible masses from that of a typical T Tauri star ($\approx 0.5 M_{\odot}$) down to a limiting value around $0.06 M_{\odot}$ below which full lithium depletion cannot occur. To narrow this mass range to a sufficiently small span to be of use requires further information about the object's age. For a given mass a star will evolve through a range of luminosity, temperature and radius values that can be quantified by a stellar model. The range of values possible prior to the cessation of lithium burning can further constrain the mass of the star should these values be measurable. The studies of the Pleiades dwarfs discussed above have used luminosity as the principal constraint, but this requires knowledge of the

distance to the object and a reliable (*i.e.* infrared) bolometric correction, neither of which are available in this study. The JHK colours of the star have been measured on the CIT system (see Thackrah *et al.* (1997)) to be (H–K) = 0.31, (J–H) = 0.54 and (I–K) = 2.83 with uncertainties of 0.05 mag. in each. The temperature evolution is considered here since an estimate can be made by spectroscopy alone.

Figure 5.10: Far red spectra of 296A compared to a giant (BS 6020) and a dwarf system (Gl 65AB). Three features used to assess the surface gravity of the star with respect to giant and dwarf classes are marked.

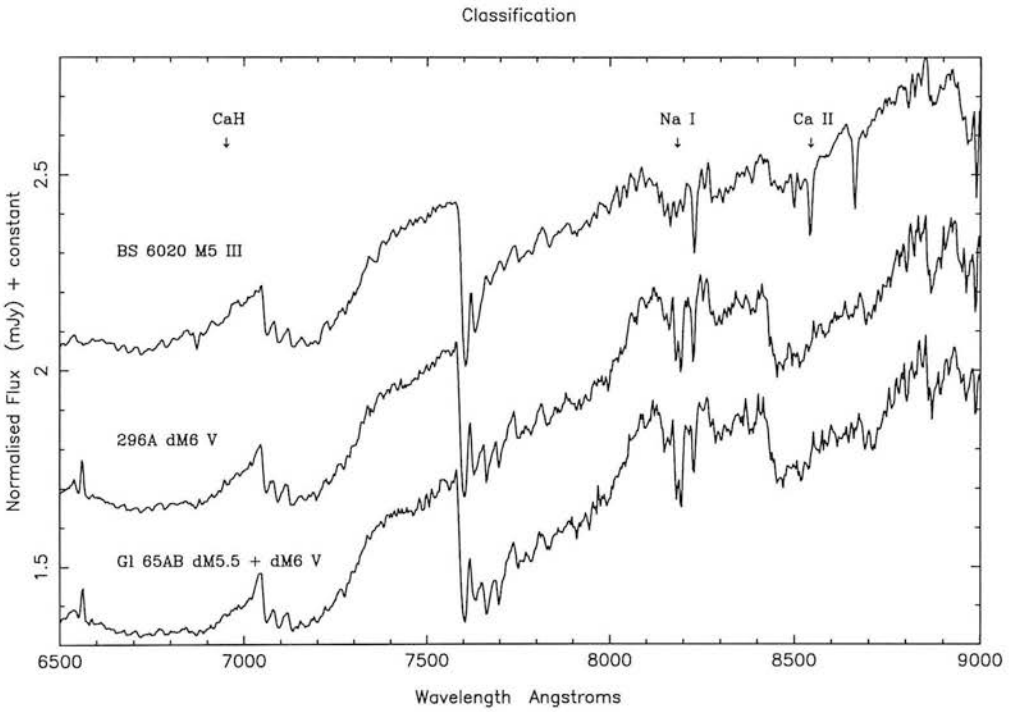

Figure 5.10 shows the far red spectra of three stars including 296A, measured with the 270R grating as described above. Compared to 296A are BS 6020, an M5 giant and GL 65AB an M5.5/M6 binary. Three absorption features are indicated, CaH (6975Å), Na I (8183Å) and Ca II (8542 Å). These features have been shown to be sufficiently sensitive to atmospheric pressure to allow discrimination between dwarf and giant stars and to give some measure of the surface gravity of the object (which is related to age). Table 5.10, from Thackrah *et al.* (1997) details the measurement of three flux ratios, named A, C and D here (after Kirkpatrick 1995). Ratio A measures the 'continuum' flux at 7035 Å over the flux at the CaH feature. Ratio

Table 5.10: A comparison of absorption feature strengths used to assess the gravity and hence evolutionary status of 296A. Ratio A measures continuum 703.5/CaH 697.5 , ratio C is continuum 811.5/Na 818.3 to 819.5 and ratio D measures cont. 857.2/Ca II 854.2 (wavelengths in nm).

Object	Ratio A	Ratio C	Ratio D	Spec. type
VB10	1.50	1.12	1.10	M8 V
Gl 65AB	1.50	1.45	1.11	M5.5 V +M6 V
296A	1.40	1.16	1.09	M6 V
Sz81	1.26	0.97	1.08	M5.5 IV
BS6020	1.23	1.01	1.383	M5 III

C measures the 8115 Å continuum over Na I and Ratio D measures the 8572Å flux over the Ca II feature. Included in table 5.10 are the T Tauri Sz 81 and the M8 dwarf VB 10 (GL 752B). The trend in values from low gravity giant, through T Tauri to (old) disc dwarf confirms that 296A is a dwarf, albeit a young one. The spectral class of 296A is estimated to be M6, based upon the VO feature at 7445Å (compare with the Kirkpatrick *et al.* 1991 classification of GL 65AB) and a corresponding temperature $2800 \pm 200K$ is inferred (measurements provided by Hugh Jones).

Armed with a temperature estimate, the status of 296A can be assessed by a suitable stellar model as discussed above. Figure 5.11 plots the effective temperature isotherms of three models for 2600, 2800 and 3000K in the (mass, age) plane. The models of Nelson *et al.* (1993), D'Antona and Mazzitelli (DM94, 1994) and Burrows *et al.* 1993 are compared, the solid lines for NRJ93, dot-dashed lines for BHSL93 and dotted lines for DM94. The isochrones marking the onset and end of lithium burning are marked as dashed lines and are taken from the NRJ93 calculations. The region bounded by the NRJ93 isotherms and isochrones is shaded

and represents the possible range of mass and age values available to a star with undepleted lithium in the $2800 \pm 200K$ temperature range. The NRJ93 model sets upper and lower limits for the mass of 296A at $0.09M_{\odot}$ and $0.045M_{\odot}$ respectively. Using the isothermal limits of either of the other compared models gives a lower upper limit, $0.07M_{\odot}$ for the DM94 model. The lower mass limit carries with it the assumption that the star is currently burning lithium. The equivalent width of the 296A 6708Å Li I is measured to be 0.5 ± 0.1Å which, by theoretical predictions is below initial abundance for such a star and thus supports the assumption. It should be noted that stars with masses below about $0.065M_{\odot}$ are predicted to retain their *measurable* lithium content indefinitely. The definition of the start of lithium burning taken here is the simple one of any reduction in the initial abundance of the (dominant) ^{7}Li component of the line.

The lithium test has been proposed as a brown dwarf discriminant for free-floating field stars of age greater than one gigayear (Nelson *et al.* 1993b). For younger stars the test is not so clean-cut due to the duration of lithium burning in higher mass objects. The test has however been applied and as described above has been able to considerably improve the mass estimate of the object. A star such as 296A with an R–I of 2.5 and a spectral class M6 would yield a mass of around $0.12M_{\odot}$ from conventional bolometric corrections[3] as they have been applied in previous photographic surveys to define the stellar mass function. The star is the first Galactic field object to have a sub-stellar mass determined in this way and is important in the affirmation it gives to the presence of free-floating brown dwarfs in the Galactic disc. The study presented in chapter three suggested that almost all brown dwarfs detected in a conventional photographic survey will be younger than one gigayear and so the nature of 296A is not surprising. Future photographic surveys must contend with the fact that many of the very low mass stars that they may detect will be similar to 296A and thus require the kind of spectroscopic measurements discussed here if limits on the local mass density are to be set.

[3]see Kirkpatrick 1995

Figure 5.11: A comparison of predicted isotherms for three brown dwarf models. The dashed lines represent the start and end of lithium burning for a given mass, based on the NRJ93 model, solid lines are isotherms for the NRJ93 model representing the inferred temperature limits of the brown dwarf candidate 296A. Dot-dashed mark the equivalent isotherms of the BHSL93 model X and dotted lines denotes those for DM94 model 7.

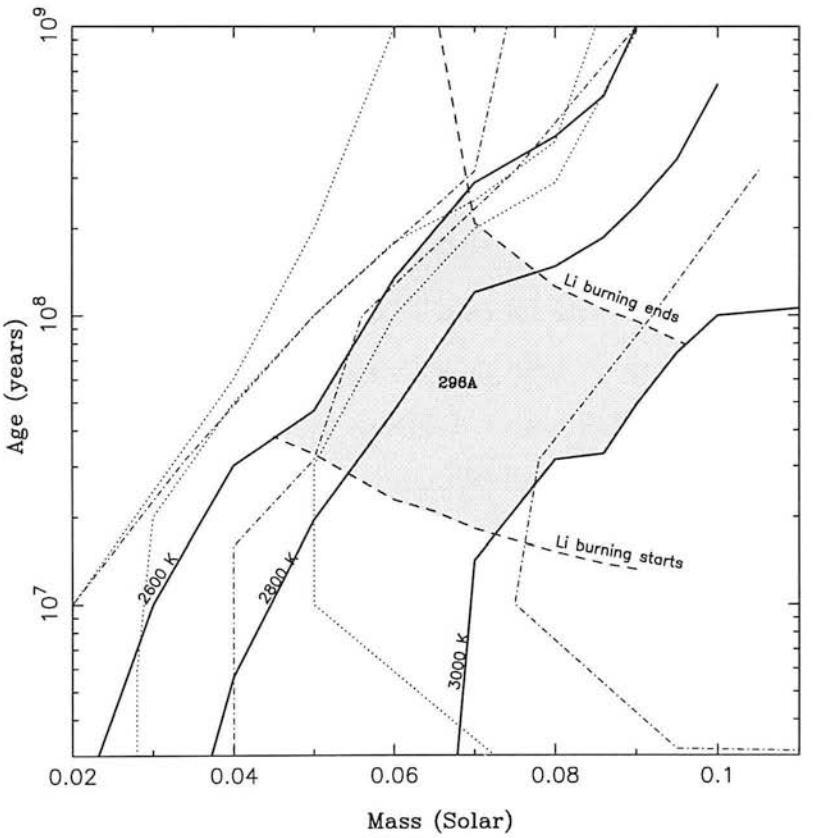

Chapter 6

Conclusion

This thesis has taken the detection of very low mass stars and brown dwarfs by photographic methods as its theme. The case for the existence of brown dwarfs has been reviewed and it is concluded that current theories of the formation of low mass bodies in the inter-stellar medium are not sufficiently developed yet to able to place a lower limit to the minimum stellar fragmentation mass. Existing models consider the formation of binary and planetary systems as being more likely than the formation of free-floating objects. Models of stellar structure are more fully developed and suggest a continuation of the properties of low mass stars through a transitionary region near the minimum hydrogen burning mass down to objects with masses at least as small as $0.01 M_{\odot}$. The weakest facet of the numerical models are the atmospheres which are essential for the relation of physical values to observable values. A seemingly systematic offset of 100-200K exists between model atmospheres and observations of the coolest stars although progress is being made in modelling the atmospheres of bluer, low metallicity stars where the effects of TiO and VO are less dominant.

The question of the existence of dark baryonic matter in the Galactic disc remains open, although agreement is converging on a value around $0.1 \mathrm{M}_{\odot}$ pc^{-3}. Recent measurements of the low mass stellar mass function in a variety of environments have suggested that a mass power law of index $\alpha \approx -1.5$ is a reasonable approxi-

mation. The value differs for the very nearby solar neighbourhood (< 10 pc) and the issue of binarity remains a very thorny problem.

Predictions of the low mass star surface distribution suggest that surveys employing far-red photographic plates/emulsions will be limited to detecting brown dwarfs with ages less than one gigayear, due to the rapid cooling of these objects and the high flux limit of photographic plates. These objects may only constitute around one tenth of the whole population (for a constant star formation rate in a 10 gigayear old Galactic disc). Extrapolating the stellar mass function into the brown dwarf regime to account for the suggested local missing mass yields surface number counts over one square degree which are close to unity within the completeness limit of a photographic plate. The number counts have been compared to the case of a time-dependent density function and for a case in which the Sun lies 50 pc above the Galactic plane. The resulting number counts vary by approximately 50% in the photographically detectable range but differences are only significant beyond the photographic flux limit.

The stellar luminosity function has been measured from a survey of 111.6 square degrees of the southern sky in SERC fields 117, 341, 342, 343 and 349. Agreement with previous measurements is fair, but an excess density is implied for $M_R = 14 \pm 0.5$ which may be due to contamination by several objects revealed by proper motion measurements. The overall trend of the function is a decline from a peak around $M_R = 11$ to the faintest sampled bin at $M_R = 16$. The objects for the $M_R = 14$, 15 and 16 bins are tabulated with the suggestion of follow-up work on the brighter members to verify or disprove the possibility of local variation in the luminosity function and on all members to ascertain their age and evolutionary status, from which it may be possible to apply mass limits, should the objects be sufficiently young.

Such follow-up observations have been presented for a second sample of stars culled from a preliminary red object survey of the original fields selected for the luminosity function. The observational programme is based around the detection of the Li I

absorption feature at 6708.8 Å. The depletion of lithium has been shown to be very sensitive to the conditions prevalent in low mass brown dwarfs and measurement of the line provides a 'Lithium test' which is predicted to clearly discriminate between objects above or below a mass of approximately $0.065M_{\odot}$ provided the age of the object is at least 10^9 years. For younger objects, interpretation is more complex and requires additional measurement of a physical value such as luminosity or temperature to estimate the evolutionary status of the object. This adds further model-dependence to the analysis but is capable of significantly narrowing the uncertainty in the estimate of the object's mass.

Concerning the status of brown dwarfs as astronomical objects, several changes have taken place in the years during the start of this project. In March, 1994 there was an I.A.U. Colloquium (148) entitled *The Future Utilisation of Schmidt Telescopes*, held in Bandung, Indonesia. As the title clearly states the intention of the meeting was to assess the opinions of astronomers regarding the continued scientific value of Schmidt telescopes, and of photographic astronomy in general. At this meeting I gave a brief presentation of the nascent project that eventually became the work described in this thesis. Technical set-backs with the development of SuperCosmos during this time means that a large photographic red object survey of the southern sky has yet to be carried out. The overall mood of the meeting was somewhat pessimistic in the face of the rapid growth of CCD arrays and telescopes. The completion of the UKST I band survey was even in question (this has since been resolved).

Four months later, An ESO workshop was held in Garching, Germany, dedicated to the study of the objects at *The Bottom of the Main Sequence - and Beyond.* Again the mood was pessimistic, not this time about the future of photographic surveys, but due to the gradual whittling-down of the brown-dwarf candidate list and the lack of convincing new entries (see Trimble's summary, 1995). During this meeting Reid concluded that the method of using photographic plates to conduct very low mass star surveys has run its course, due to the flux limitations, unreliable colour indices and large photometric uncertainties. It was suggested that the future of

this field lies in the use of wide-field IR surveys such as 2MASS and DENIS.

Within two years of these meetings, detections of brown dwarfs in the Pleiades with confirmed lithium measurements have been reported. There has also been a minor glut of detections of binary and planetary bodies. These discoveries have done much to elevate the status of brown dwarfs above the level of hypothetical objects, leading the journal Nature to comment *" Brown dwarfs exist - Official"*. Notably, all these objects have been detected using infrared technology and the question is posed: Have photographic surveys really run their course, or can they yet contribute to a field of study that appears to be entering its hey-day?

The body of evidence assembled from this and other photographic surveys over the past fifteen years or so suggests that the majority of brown dwarfs must lie *just* beyond the flux limit of conventional photographic plates. In order to make further progress in this field future surveyors have two options: to conduct huge, essentially all-sky surveys using photographic plates to detect the local brown dwarf population or to increase the magnitude limit of the plate material. Concerning the first option, the realisation of an all-sky survey is now possible using the SUPERCOSMOS measuring machine. To this end the EROSS project has been proposed (Hambly, private communication). The Edinburgh Red Object Survey *with* SUPERCOSMOS is an ambitious project to select red objects (by R–I) using the entire UKST R and I survey plate sets (outside the Galactic plane). The project will benefit from the ability to match the DENIS infrared survey dataset to it findings and presents an excellent opportunity to determine the very low mass stellar distributions (luminosity and mass) in the Solar neighbourhood.

Regarding the increase in magnitude limit, Hawkins (1995) has shown that it is possible to digitally stack Schmidt plate scans to improve the signal-to-noise sufficiently to push back the flux limit by two or more magnitudes. The early results of this project included several stars with extremely red spectra. Parallax measurements for these objects are now complete and further results are due. This dataset provides a good opportunity to assess how severe the conventional

photographic flux limit really is for this type of survey. The method of stacking requires large numbers of plates in each waveband in each survey field and is thus unlikely to be applicable to more than a handful of choice regions of the sky. More encouraging in this respect is the progress of the UKST's experiments with photographic *film*. Parker *et al.* (1995) have demonstrated the ability of the red-sensitive Tech-Pan film emulsions to probe to fainter limits than glass plates and in a recent report, Hewett *et al.* (1996) present the preliminary results of a red object survey with Tech-Pan film scanned by the APM machine in Cambridge. Spectra of several very late M dwarfs are presented and there is potential here to conduct wide-field surveys to at least a magnitude fainter than current plates.

To conclude, recent technical advances in measuring machine speed and accuracy and in plate and film material provide new opportunities to the stately art of photographic survey science. With recently reported detections of very convincing brown dwarf candidates in the Pleiades, the goals of this field of study have moved away from the singular issue of detecting sub-stellar objects and towards a quantification of their place as a population in the Milky Way and this is a task to which modern wide-field photographic techniques are well suited.

References

Abt, H. A. 1979, A.J., **84**, 1591

Adams, F.C. and Benz, W. 1992, in *Complementary Approaches to Binary and Multiple Star Research*, IAU Colloq. No, 135, ed. McAlister, H. (P.A.S.P.)

Adams, F. C. 1995 in *The bottom of the main sequence - and beyond*, ed. Tinney, C. G. (Springer-Verlag)

Allard, F. 1990, *Ph.D. Thesis, Ruprecht Karls Universität Heidelberg*

Bachall, J. N. 1984, Ap.J., **276**, 156

Bahcall, J. N., Flynn, C. & Gould, A. 1992, Ap.J., **389**, 234

Baraffe, I., Chabrier, G., Allard, F. & Hauschildt, P. H. 1995, Ap.J., **446**, L35

Baraffe, I. and Chabrier, G. 1996, Ap.J., **461**, L51

Basri, G, Marcy, G. W. & Graham, J. R. 1996, Ap.J. **458**, 600

Beard, S. M., MacGillivray, H. T. & Thanisch, P. F. 1990, MNRAS, **247**, 311

Becklin, E. E. and Zuckerman, B. 1988, Nature, **336**, 656

Berriman, G., Reid, N. 1987, MNRAS, **227**, 315

Berriman, G., Reid, N. & Leggett, S. K. 1992, Ap.J., **392**, L31

Bessell, M. S. 1986, P.A.S.P., **98**, 1303

Bessell, M. S. 1991, A.J., **101**, 662

Bessell, M. S. and Stringfellow, G. S. *Annual Rev. Astron. Astrophys.* 1993. **31**, 433-71

Bienaymé, O., Robin, A. & Crézé, M. 1987, A&A, **180**, 94 (BRC)

Boss, A. P. 1986, in *Astrophysics of Brown Dwarfs*, eds. Kafatos, M. C., Harrington, R. S. & Maran, S. P. C.U.P.

Boss, A. P. and Myhill, E. A. 1992, Ap.J.Sup., **82**, 311

Brand, J. and Blitz, L. 1993, A&A, **275**, 67

Burrows, A., Hubbard, W. B. & Lunine, J. I. 1989, Ap.J., **345**, 939

Burrows, A. and Liebert, J. 1993, Rev. Mod. Physics, **65**, 301

Burrows, A., Hubbard, W. B., Saumon, D. & Lunine, J. I. 1993, Ap.J., **406**, 158

Chabrier, G., Baraffe, I. & Plez, B. 1996, Ap.J.,**459**, L91

Chester, T. 1995, in *The bottom of the main sequence - and beyond*, ed. Tinney, C. G. (Springer-Verlag)

Combes, F. 1991, ARA&A, **29**, 195

Comeron, F., Rieke, G. H., Burrows, A. & Rieke, M. J. 1993, Ap.J., **416**, 185

Copet, E., de Batz, B., Epchtein, N., Fouque, P., Lacombe, F., Rouan, D., Tiphéne, D., Borsenberger, J., Le Berte, T. and Kimeswenger, S. 1995, in *The bottom of the main sequence - and beyond*, ed. Tinney, C. G., Springer-Verlag.

Cunow, B. 1993, A&AS, **97**, 541

Cunow, B. and Ungruhe, R. 1995, A&AS, **112**, 213

Dahn, C. C., Liebert, J. & Harrington, R. S. 1985, A.J., 91, 621

D'Antona, F. D., Mazzitelli, I. 1994, Ap.J.S **90**, 467

Dawe, J. A. & Metcalfe, N. 1982, Proc. A.S.A. **4(4)**, 486.

Dawson, P. C. 1986, Ap.J., **311**, 984

de Vegt, Chr., Winter, L. & Zacharias, N. 1992, in *Digitised optical sky surveys* p.3-8, Eds. MacGillivray, H. T. and Thomson, E. B., Kluwer Academic publishers.

Deul, E. 1992 in *Digitised optical sky surveys* p.3-8, Eds. MacGillivray, H. T. and Thomson, E. B., Kluwer Academic publishers.

Felten, J. E. 1976, Ap.J., **207**, 700

Fischer, D. A. & Marcy, G. W. 1992, Ap.J. **396**, 178

García López, R. J., Rebolo, R. & Martín, E. L. 1994, A&A, **282**, 518

Gilmore, G., Reid, N. & Hewett, P. 1985, MNRAS, **213**, 257

Gilmore, G, 1990 in *Baryonic dark matter*, eds. Lynden-Bell, D. and Gilmore, G. Kluwer Academic Publishers

Gliese, W., 1969 *Veröffentl. Astron. Rechen-Inst. Heidelberg*, No. 22

Gliese, W. and Jahreiß, H. 1991, in *The Astronomical Data Centre CD-ROM: Selected Astronomical Catalogues*, Vol. 1, eds. Brotzmann, L. E. and Gesser, S. E., NASA/ADC, Greenbelt, MD

Gómez, A. E, Delhaye, J., Grenier, S., Jaschek, C., Arenou, F. & Jaschek, M. 1990, AA, **236**, 95

Gould, A. 1990, MNRAS, **244**, 25

Grossman, A. S., Hays, D. & Graboske, H. C. 1974, A&A, **30**, 95

Guibert, J. 1992, in *Digitised optical sky surveys* p.3-8, Eds. MacGillivray, H. T. and Thomson, E. B., Kluwer Academic publishers.

Hambly, N. C., Hawkins, M. R. S. & Jameson, R. F. 1991, MNRAS, **253**,1

Hambly, N. C., Steele, I. A., Hawkins, M. R. S. & Jameson, R. F. 1995, MNRAS, **273**, 505

Harrington, R. S. 1986, in *Astrophysics of Brown Dwarfs*, eds. Kafatos, M. C., Harrington, R. S. & Maran, S. P. C.U.P.

Hawkins, M. R. S. and Bessell, M. S. 1988, MNRAS, **234**, 177

Hawkins, M. R. S. 1995, in *The future utilisation of Schmidt telescopes* p. 137-147, Eds. Chapman, J., Cannon, R., Harrison, S. & Hidayat, B. A.S.P. conference series Volume 85.

Hawley, S. 1995, in *The bottom of the main sequence - and beyond*, ed. Tinney, C. G. (Springer-Verlag)

Hayashi, C. 1962, P.A.S. of Japan, *13*, 450

Henry, T. J. and McCarthy, Jr, D. W. 1992, in *Complementary Approaches to Binary and Multiple Star Research*, IAU Colloq. No, 135, ed. McAlister, H. (P.A.S.P.)

Henry, T. J. and McCarthy, Jr, D. W. 1993, A.J. **106**, 773

Hewett, P, Harding, M., Warren, S., Drinkwater, M. and Foltz, C. 1996, Spectrum: Newsletter of the Royal Observatories, September edn.

Heydon-Dumbleton, N. H., Collins, C. A. & MacGillivray, H. T. 1989, MNRAS, **238**, 379

Hill, E. R., Hilditch, R. W. & Barnes, J. V. 1979, MNRAS, **186**, 813

Hu, E. M., Huang, J.-S., Gilmore, G. and Cowie, L. L. 1994, Nature **371**, 493

Hubbard, W. B., Burrows, A., Saumon, D. & Lunine, J. I. 1992, B.A.A.S, **181**, 2802

Jones, H. R. A., Longmore, A. J., Jameson, R. F. & Mountain, C. M. 1994, MNRAS **267**, 413

Jones, H. R. A., Longmore, A. J., Allard, F. & Hauschildt, P. H. 1996, MNRAS, **280**, 77

Jones, L. R., Fong, R., Shanks, T., Ellis, R. S. & Peterson, B. A. 1991, MNRAS, **249**, 481

Kirkpatrick, J. D., Henry, T. & McCarthy, D. W. 1991, Ap.J.Sup., **77**, 417

Kirkpatrick, J. D., Henry, T. & Liebert, J. 1993, **406**, 701

Kirkpatrick, J. D., McGraw, J. T., Hess, T. R., Liebert, J. & McCarthy, D. W. 1994, Ap.J.S, **94**, 749

Kirkpatrick, J. D. 1995, in *The bottom of the main sequence - and beyond*, ed. Tinney, C. G. (Springer-Verlag)

Kirkpatrick, J. D., Henry, T. J. & Simons, D. A. 1995, A.J. 109, 797

Kopal, Z. *Numerical Analysis*, Chapman & Hall, 1961

Kroupa, P., Tout, C. A. & Gilmore, G. 1991, MNRAS, **251**, 293

Kumar, S. S. 1963, Ap.J. **137**, 1121

Kuijken, K. and Gilmore, G. 1989a, MNRAS, **239**, 571

Kuijken, K. and Gilmore, G. 1989b, MNRAS, **239**, 571

Kuijken, K. and Gilmore, G. 1989c, MNRAS, **239**, 651

Kuijken, K. and Gilmore, G. 1991, Ap.J., **267**, L9

Lasker, B. M. *et al.* 1988, Ap.J.S, **68**, 1

Lasker, B. M. 1995, in *The future utilisation of Schmidt telescopes* p. 137-147, Eds. Chapman, J., Cannon, R., Harrison, S. & Hidayat, B. A.S.P. conference series Volume 85.

Laughlin, G. and Bodenheimer, P. 1993, Ap.J., **403**, 303

Lee, J. -F. and van Altena, W. 1983, A.J., **88**, 1683

Leggett, S. K. 1992, Ap.J.S, **82**, 351

Leggett, S. K. and Hawkins, M. R. S. 1988, MNRAS, **234**, 1065

Leggett, S. K., Harris, H.C. & Dahn, C. C. 1994, A.J., **108**, 944

Leggett, S. K., Allard, F., Berriman, G., Dahn, C. C. & Hauschildt, P. H. 1996, Ap.J.Sup., **104**, 117

Lutz, T. E. and Kelker, D. H. 1973, PASP, **85**, 573

Luyten, W. J. 1979, The NLTT Catalogue, vol. 2. University of Minnesota, Minneapolis.

Luyten, W. J. 1979, The LHS Catalogue. University of Minnesota, Minneapolis.

MacGillivray, H. T. and Stobie, R. S. 1985, *Vistas in Astronomy*, **27**, 433

Maddox, S. J., Efstathiou, G. & Sutherland, W. J. 1990, MNRAS, **246**, 433

Magazzú, A., Martín, E. L. & Rebolo, R. 1991, A&A, **249**, 149

Malmquist, K. G. 1924, *Medd. Lund. Series I, band VI, No. 106*

Marcy, G. W. and Butler, R. P. 1995, in *The bottom of the main sequence - and beyond*, ed. Tinney, C. G. (Springer-Verlag)

Marcy, G. W. and Butler, R. P. 1996a, Ap.J. **464**, L147

Marcy, G. W. and Butler, R. P. 1996b, Ap.J. **464**, L153

Martín, E. L., Rebolo, R., Magazzú, A. & Pavlenko, Ya.V. 1994, A&A, **282**, 503

Mera, D., Chabrier, G. & Baraffe, I 1996, Ap.J., **459**, L87

Metcalfe, N., Fong, R. & Shanks, T. 1995, MNRAS, **274**, 769

Mighell, K. J. 1990, A&AS, **83**, 109

Mihalas, D.& Binney, J., 1981 *Galactic Astronomy Structure and Kinematics* W. H. Freeman.

Miller, G. E, Scalo, J. M. 1979, Ap.J.S, **41**, 513

Mitchell, P. S. 1989, Ph. D. Thesis, University of Edinburgh.

Monet. D. G., Dahn, C. C., Vrba, F. J., Harris, H. C., Pier, J. R., Luginbuhl, C. B. & Ables, H. D. 1992, A.J., **103**, 638

Morgan, D. H. 1995 in *The future utilisation of Schmidt telescopes* p. 137-147, Eds. Chapman, J., Cannon, R., Harrison, S. & Hidayat, B. A.S.P. conference series Volume 85.

Nakajima, T., Oppenheimer, B. R., Kulkarni, S. R., Golimowski, D. A., Matthews, K. & Durrance, S. T. 1995, Nature **378**,463

Oort, J. H. 1932, Bull. Astron. Inst. Netherlands **6**, 249

Oort, J. H. 1960, Bull. Astron. Inst. Netherlands **15**, 45

Parker, Q. A., Phillips, S. & Morgan, D. 1995, in *The future utilisation of Schmidt telescopes* p. 137-147, Eds. Chapman, J., Cannon, R., Harrison, S. & Hidayat, B. A.S.P. conference series Volume 85.

Pavlenko, Ya.V, Rebolo, R., Martín, E. L. & García López, R. J., 1994, A&A, **303**,807

Pozio, F. 1991, Mem. Soc. Astr. Ital., **62**, 171

Nelson, L. A., Rappaport, S. & Joss, P. C. 1986, Ap.J., **311**, 226

Nelson, L. A., Rappaport, S. & Joss, P. C. 1993, Ap.J., **404**, 723

Nelson, L. A., Rappaport, S. & Chiang, E. 1993b, Ap.J., **413**, 364

Rebolo, R., Martín, E. L. & Magazzú, A. 1992, Ap.J., **389**, L83

Rebolo, R., Zapatero Osorio, M. R. & Martín E. L. 1995, Nature **377**, 129

Rebolo, R., Martín, E. L., Basri, G., Marcy, G. W. & Zapatero-Osorio, M. R. 1996, Ap.J., **469**, L53

Reddish, V. C. 1992 in *Digitised optical sky surveys* p.3-8, Eds. MacGillivray, H. T. and Thomson, E. B., Kluwer Academic publishers.

Reid, N. 1982, in *Proceeding of the Workshop on Astronomical Measuring Machines*, eds. Stobie, R. S. & McInnes, B. (Occasional Reports of the Royal Observatory, Edinburgh)

Reid, N. 1987, MNRAS, 225, 873

Reid, I. N. and Gilmore, G. F. 1982, MNRAS, **201**, 73

Reid, N., Tinney, C. & Mould, J. 1994, A.J., **108**, 1456

Salpeter, E. E. 1955, Ap.J., **121**, 243

Scalo, J. M. 1986, *Fund. Cosmic Phys.*, **11**, 1

Schmidt, M. 1975, Ap.J., **202**, 22

Shanks, T., Stevenson, P. R. F., Fong, R. & MacGillivray, H. T. 1984, MNRAS, **206**, 767

Spitzer, L. and Schwarzchild, M. 1951, Ap.J., **114**, 385

Spitzer, L. and Schwarzchild, M. 1953, Ap.J., **117**, 106

Stauffer, J. R., Hamilton, D. & Probst, R. 1994, A.J., **108**, 155

Staller R. F. A and DeJong, T. 1981, A&A, **98**, 140

Stobie, R. S. and Ishida, K. 1987, A.J., **93**, 624

Stobie, R. S., Sagar, R. & Gilmore. G. 1985a, A&AS, **60**, 495

Stobie, R. S., Sagar, R. & Gilmore. G. 1985b, A&AS, **60**, 503

Stobie, R. S., Ishida, K. & Peacock, J. A. 1989, MNRAS, **238**, 709

Tarter, J. C. 1986, in *Astrophysics of Brown Dwarfs*, eds. Kafatos, M. C., Harrington, R. S. & Maran, S. P. C.U.P.

Thackrah, A. D., Jones, H. R. A. & Hawkins, M. R. S. 1997, MNRAS, **284**, 507

Thanisch, P., McNally, B. V. & Robin, A. 1984, *Image and Vision Computing*, **2**, 91

Tinney, C. G. 1993, Ap.J. **414**, 279

Tinney, C. G., Reid, I. N. & Mould, J. R. 1993a, Ap.J., **414**, 254

Tritton, S. B. 1983, *U.K.S.T.U. Handbook*, Royal Observatory, Edinburgh.

Tritton, S. B., Morgan, D. H. & Cranston M. R., 1994 in *Astronomy from Wide Field Imaging*, Proc. IAU Symp. 161.

Trimble, V. 1987, *An. Rev. Astron. Astrophys.*

Trimble, V. 1995, in *The bottom of the main sequence - and beyond*, ed. Tinney, C. G. (Springer-Verlag)

Trumpler, R. J. and Weaver, H. F. *Statitical Astronomy*, Univ. Calif. Press 1953

Tyson, J. A. 1988, Ap.J., **96**, 1

UKSTU Handbook, Tritton, S. 1983 Available from U.K. Schmidt Telescope Unit, Royal Observatory, Edinburgh.

Van der Kruit, P. C. 1989, in SAAS-Fee Adv. Course 19: *The Milky Way as a Galaxy*, ed. Gilmore, G., King, I., van der Kruit, P. C. (Mill Valley, CA: Univ. Science Books), 331

Veeder, G. J. 1974, A.J., **79**, 1056

Wielen, R. 1977, A&A, **60**, 263

Wielen, R., Jahreiß, H. & Kruger, R. 1983, in *The Nearby Stars and the Stellar Luminosity Function*, I.A.U. Colloq. 76, eds. Davis, A. G. & Upgren, A. R.